

UNIVERSITÀ DEGLI STUDI DI NAPOLI
“FEDERICO II”



Facoltà di Ingegneria

Corso di Laurea Specialistica in
INGEGNERIA AEROSPAZIALE E ASTRONAUTICA
Classe delle lauree specialistiche N. 25/S

Dipartimento di Ingegneria Aerospaziale (DIAS)
in collaborazione con
MOX, Dipartimento di Matematica "F. Brioschi", Politecnico di Milano
e Dipartimento di Ingegneria dell'Informazione e Metodi Matematici,
Università degli Studi di Bergamo

**“Numerical Computations of Deflated
Vascular Geometries for Fluid-Structure
Interaction in Haemodynamics”**

Relatori: Prof. Sergio DE ROSA
Dr. Christian VERGARA (Università degli Studi di Bergamo)

Co-relatore: Dr. Matteo POZZOLI (Università degli Studi di Bergamo)

Autore:
Rocco Michele LANCELLOTTI 335/288

Anno accademico 2011/2012

Abstract

This thesis deals with a computational haemodynamic problem. The purpose is to simulate the prestressed state in human arteries and verify its effectiveness in haemodynamic fluid-structure interaction simulations.

In the first part of this work, we describe the vessel wall mechanics in regime of finite deformations with non linear hyperelastic structural models commonly used to describe biological tissue. Subsequently, we implement a parallel algorithm that consists in a simple iterative procedure based on a fixed point method. This algorithm aims at the calculation of deflated vascular geometries starting from three-dimensional vascular geometries reconstructed from radiological images. The idea is to use these deflated geometries as initial reference configurations for fluid-structure interaction simulations, in order to simulate the prestressed state of arteries. Moreover, we have tested the algorithm from a quantitative point of view, using consistency test cases on simple geometries.

In the second part of this thesis, we describe the incompressible Navier-Stokes equations in moving domains using the Arbitrary Lagrangian-Eulerian (ALE) formulation, and the fluid-structure coupled problem. Then, we use our algorithm in a parallel partitionated fluid-structure interaction solver and we perform physiological simulations on a patient-specific carotid artery with and without the use of deflated geometries, evaluating the fluid velocity, the fluid pressure, the structure displacement and the wall-shear stress fields in both cases, highlighting the differences.

All of the present work is developed within the open source object-oriented library called *LifeV*, that works on parallel architectures. In particular, *LifeV* is a finite element library that solves several physical problems, such as fluid dynamics, reaction-diffusion-transport and mechanical problems in a multiphysics contest.

Keywords: Prestress, fluid-structure interaction, computational haemodynamics, parallel computing, hyperelasticity, nonlinear structure, large deformations.

Sommario

Questa tesi tratta un problema di emodinamica computazionale. Lo scopo è quello di simulare lo stato di prestress presente nelle arterie e verificarne l'efficacia nelle simulazioni di interazione fluido-struttura in ambito emodinamico.

Nella prima parte di questo lavoro viene descritta la meccanica delle pareti arteriose in regime di deformazioni finite, usando modelli strutturali non lineari ed iperelastici comunemente impiegati per descrivere tessuti biologici. In seguito, abbiamo implementato un algoritmo parallelo che consiste in una semplice procedura iterativa basata su un metodo di punto fisso. Questo algoritmo calcola geometrie vascolari sgonfie partendo da geometrie tridimensionali ricostruite da immagini radiologiche. L'idea è quella di usare queste geometrie sgonfie come configurazione iniziale di riferimento nelle simulazioni di interazione fluido-struttura, al fine di simulare lo stato prestressato delle arterie. Abbiamo inoltre testato l'algoritmo da un punto di vista quantitativo usando casi test su geometrie semplici.

Nella seconda parte di questa tesi descriviamo le equazioni di Navier-Stokes nel caso incomprimibile per domini in movimento usando la formulazione Arbitrary Lagrangian-Eulerian (ALE), e descriviamo il problema accoppiato fluido-struttura. Successivamente utilizziamo il nostro algoritmo in un solutore fluido-struttura parallelo e partizionato ed effettuiamo delle simulazioni fisiologiche su una arteria carotidea di un paziente specifico, con e senza geometrie sgonfie, valutando i campi di velocità e pressione del fluido, il campo di spostamenti della struttura e quello dello stress di taglio alla parete ed evidenziandone le differenze.

Il presente lavoro è interamente sviluppato all'interno della libreria open-source *LifeV*, che lavora su architetture in parallelo. In particolare, *LifeV* è una libreria agli elementi finiti che risolve diversi problemi fisici, come problemi di dinamica dei fluidi, problemi di reazione-diffusione-trasporto e problemi meccanici in contesto multifisico.

Parole chiave: Prestress, interazione fluido-struttura, emodinamica computazionale, calcolo parallelo, iperelasticità, struttura non lineare, grandi deformazioni.

Contents

1	Introduction	1
1.1	Motivations	1
1.2	The role of numerical simulations	6
1.3	The present work	11
1.4	Outline	12
2	Artery wall mechanics	13
2.1	The artery wall	13
2.1.1	State of the art	15
2.1.2	Open problems	18
2.2	Three-dimensional finite elasticity	19
2.2.1	Kinematics	19
2.2.2	Equations of motion	21
2.2.3	Hyperelastic materials	23
2.2.4	Structural models within this work	26
2.3	Finite-element formulation	28
2.3.1	Weak formulation of the structural problem	28
2.3.2	Time discretization	30
2.3.3	Linearization	31
2.3.4	Quadrature rules and computation of integrals	32
3	The recovering of the correct initial geometry	35
3.1	The need to use a deflated geometry	35
3.2	State of the art	37
3.3	Description of the strategy used in this work	41
3.4	Numerical results	43
3.4.1	Cube	44
3.4.2	Cylinder	52
4	Incompressible Navier-Stokes equations in moving domain	61
4.1	The blood modeling	61
4.2	The fluid and the fluid domain problem	62
4.3	Finite element formulation	66

4.3.1	Weak formulation for the fluid and the fluid domain problems	66
4.3.2	Finite element discretization	67
4.3.3	Time discretization	70
5	Fluid-Structure Interaction	73
5.1	Introduction	73
5.2	The FSI problem	73
5.2.1	Time discretization	75
5.2.2	Boundary conditions	76
5.3	Partitioned algorithms for the numerical solution of the FSI problem	79
6	Haemodynamic results	85
6.1	Carotid artery stenosis	85
6.2	Numerical results	90
	Conclusions	103
	Appendix: Functional spaces	105
	Bibliography	107

List of Figures

1.1	Direct and indirect costs (in billions of dollars) of major cardiovascular diseases (CVD) (United States: 2008).	3
1.2	Examples of modern non-invasive data collection technologies.	8
1.3	Carotid bifurcation in healthy and diseased state.	9
1.4	Fluid velocity on a patient-specific carotid bifurcation before and after carotid thromboendarterectomy.	10
2.1	Artery wall layers.	14
2.2	Representative pressure–stretch response of an intact internal carotid artery. . .	16
3.1	Pressure-stretch curve for an artery with nonlinear material behaviour.	36
3.2	Typical stress-strain curve for an exponential material.	38
3.3	Deformation of an AAA when failure of convergence for ID appears.	40
3.4	Backward incremental modelling approach.	41
3.5	The cube.	45
3.6	Cube, residual χ vs. load \bar{p}	46
3.7	Cube, number of iterations vs. load \bar{p}	46
3.8	Cube, values of the relaxation parameter α vs. load \bar{p}	47
3.9	St.Venant-Kirchhoff material cube, comparison between the reference geometry $\widehat{\Omega}$ and the deflated geometry Ω_0 , for the load case $\bar{p} = 0.625 \cdot 10^6 \text{ dyne/cm}^2$	48
3.10	Exponential material cube, comparison between the reference geometry $\widehat{\Omega}$ and the deflated geometry Ω_0 , for the load case $\bar{p} = 0.625 \cdot 10^6 \text{ dyne/cm}^2$	49
3.11	St.Venant-Kirchhoff material cube, comparison between the reference geometry $\widehat{\Omega}$ and the deflated geometry Ω_0 reinflated with the load $\bar{p} = 0.625 \cdot 10^6 \text{ dyne/cm}^2$	50
3.12	Exponential material cube, comparison between the reference geometry $\widehat{\Omega}$ and the deflated geometry Ω_0 reinflated with the load $\bar{p} = 0.625 \cdot 10^6 \text{ dyne/cm}^2$	51
3.13	The cylinder.	53
3.14	Cylinder, residual χ vs. load \bar{p}	55
3.15	Cylinder, number of iterations vs. coefficient β	55
3.16	Cylinder, values of the relaxation parameter α vs. coefficient β	56

3.17	St.Venant-Kirchhoff material cylinder: comparison between the reference geometry $\widehat{\Omega}$ and the deflated geometry Ω_0 , for the Robin boundary condition coefficient $\beta = 0 \text{ dyne/cm}^3$	57
3.18	Exponential material cylinder: comparison between the reference geometry $\widehat{\Omega}$ and the deflated geometry Ω_0 , for the Robin boundary condition coefficient $\beta = 0 \text{ dyne/cm}^3$	58
3.19	St.Venant-Kirchhoff material cylinder: comparison between the reference geometry $\widehat{\Omega}$ and the deflated geometry Ω_0 reinflated with the load $P_d = 80 \text{ mmHg} = 106640 \text{ dyne/cm}^2$	59
3.20	Exponential material cylinder: comparison between the reference geometry $\widehat{\Omega}$ and the deflated geometry Ω_0 reinflated with the load $P_d = 80 \text{ mmHg} = 106640 \text{ dyne/cm}^2$	60
4.1	The three major types of cells in blood.	62
4.2	Moving mesh.	63
4.3	The ALE frame described by the map \mathcal{A}_t , which maps a reference (initial) domain into the current one.	64
5.1	Description of the FSI domain.	74
5.2	An image from an eco-color-doppler ultrasound machine.	77
5.3	From the eco-color-doppler image to the patient-specific flow rate.	78
5.4	Section of the FSI domain.	79
6.1	A carotid plaque.	86
6.2	Eco-color-doppler scan of plaque formation at internal carotid artery (ICA).	87
6.3	Plaque formation process.	88
6.4	Typical values of WSS for carotids.	89
6.5	A MRA image of left and right carotids.	90
6.6	The inflated solid mesh.	92
6.7	The deflated solid mesh.	93
6.8	Comparison between inflated and deflated carotid geometries.	94
6.9	Solid displacement for the inflated and the deflated geometries at systole.	95
6.10	Velocity for the inflated and the deflated geometries at systole.	96
6.11	Wall shear stress for the inflated and the deflated geometries at systole.	96
6.12	Solid displacement for the inflated and the deflated geometries at diastole.	97
6.13	Velocity for the inflated and the deflated geometries at diastole.	97
6.14	Wall shear stress for the inflated and the deflated geometries at diastole.	98
6.15	Particular of the wall shear stress distribution inside the internal carotid artery, for the inflated and the deflated geometries at systole.	98
6.16	The two sections considered to evaluate flow rate and pressure fields.	99
6.17	Flow rate comparison between inflated and deflated geometries at two different sections.	100

6.18 Pressure comparison between inflated and deflated geometries at two different sections. 101

List of Tables

1.1	International men death rates (per 100 000 population) for total CVD, CHD, stroke, and total deaths in selected countries (revised May 2011).	4
1.2	International women death rates (per 100 000 population) for total CVD, CHD, stroke, and total deaths in selected countries (revised May 2011).	5
2.1	Well-known Newmark methods.	31
3.1	Cube mesh properties.	44
3.2	Set of structural parameters for the cube and the cylinder.	44
3.3	Cylinder mesh properties.	54
6.1	WSS range for healthy and pathological arteries.	89
6.2	Set of structural and fluid parameters for the inflated and deflated geometries.	91
6.3	Inflated geometry mesh properties.	92
6.4	Deflated geometry mesh properties.	93

Chapter 1

Introduction

The first part of this chapter presents the motivations of this work with a general overview on the more common cardiovascular diseases. The second part explains the role of numerical simulation in the study of cardiovascular diseases. The third part presents the contribution of this work both in mechanical and haemodynamic fields. In the last section there is the outline of this thesis.

1.1 Motivations

The use of mathematical models, originally radicated mainly in sectors with a strong technical content (such as, e.g., automotive and aerospace engineering), is now widespread also in many fields of life sciences. Bioinformatics, mathematical analysis and scientific computing support investigations in different fields of biology (like genetics or physiology) and medicine.

The main impulse to this field of study comes from the increasing demand in the medical community for scientifically rigorous and quantitative investigations of *cardiovascular diseases* (CVD). In 2010, 18.1 million people died of CVD. Today, 1.3 billion people smoke worldwide, 600 million have hypertension, and 220 million live with diabetes which puts more than 2 billion individuals at risk of heart disease, stroke, or a related health problems. In particular, stroke is the second leading cause of death globally, and the leading cause of acquired disability, killing 5.7 million people every year [1] (see tables 1.1, 1.2).

Major CVD includes diseases listed in the bullet points below:

- *High blood pressure* (HBP) or *hypertension*, defined as systolic pressure ≥ 140 mmHg and/or diastolic pressure ≥ 90 mmHg, use of antihypertensive medication, or being told at least twice by a physician or other health professional that one has HBP. One in three US adults has HBP and projections show that by 2030, an additional 27 million people could have hypertension, a 9.9% increase in prevalence from 2010.
- *Coronary heart disease* (CHD), *acute coronary syndrome* and *angina pectoris*. Over the next 20 years, medical costs of CHD (real 2008\$) are projected to increase by 200%: of

CVD indirect costs, CHD is projected to account for 40% and has the largest indirect costs.

- *Stroke* (cerebrovascular disease). It causes one of every eighteen deaths in USA. Projections show that by 2030, an additional 4 million people will have had a stroke, a 24.9% increase in prevalence from 2010.
- *Cardiomyopathy* and *heart failure*.
- *Disorders of heart rhythm*.
- Other cardiovascular diseases: *valvular heart disease*, aortic, mitral, pulmonary and tricuspid *valve disorders*, etc.

An estimated 82.6 million American adults (more than one third) have one or more types of CVD. Of these, 40.4 million are estimated to be older than 60 years of age [2]. The total direct and indirect cost of CVD in the United States for 2008 is estimated to be \$297.7 billion (see fig. 1.1). This figure includes health expenditures (direct costs, which include the cost of physicians and other professionals, hospital services, prescribed medications, home health care, and other medical durables) and lost productivity resulting from mortality (indirect costs). By comparison, in 2008, the estimated cost of all cancer and benign neoplasms was \$228 billion. CVD costs more than any other diagnostic group. By 2030, 40.5% of the US population is projected to have some form of CVD and total medical costs of CVD are projected to triple, from \$273 billion to \$818 billion [3].

In Europe, each year, CVD causes over 4.3 million deaths, nearly half of all deaths in Europe. It is the main cause of death in women in all countries of Europe and is the main cause of death in men in all countries except France, the Netherlands and Spain. The financial burden for EU health care systems related to this group of diseases has been estimated to be just under €192 billion in 2006, almost €110 billion of which were direct costs and €82 billion were indirect costs. CVD are very strongly associated with social conditions and differences in CVD rates are the biggest single causes of health inequalities both between and within the Member States [4].

There is certainly a need to a change of behaviours and lifestyle to prevent these diseases induced by smoking, an incorrect diet, physical inactivity, alcohol consumption and psychosocial stress. At the same time, however, it is necessary to provide effective investigative tools to treat existing diseases and better understand the phenomena behind this type of problems and provide a more effective prevention. In the past decade, the application of mathematical models, seconded by the use of efficient and accurate numerical algorithms, has made impressive progress in the interpretation of the circulatory system functionality, in both physiological and pathological situations, as well as in the perspective of providing patient specific design indications to surgical planning. Continued advances in molecular and cell biology, biomechanics, medical imaging, computational methods, and computational power promise to revolutionize our understanding and thus treatment of these devastating diseases. There is a pressing need, therefore, to synthesize these many advances into a consistent clinically useful tool. Computational methods could enable cardiovascular device manufacturers

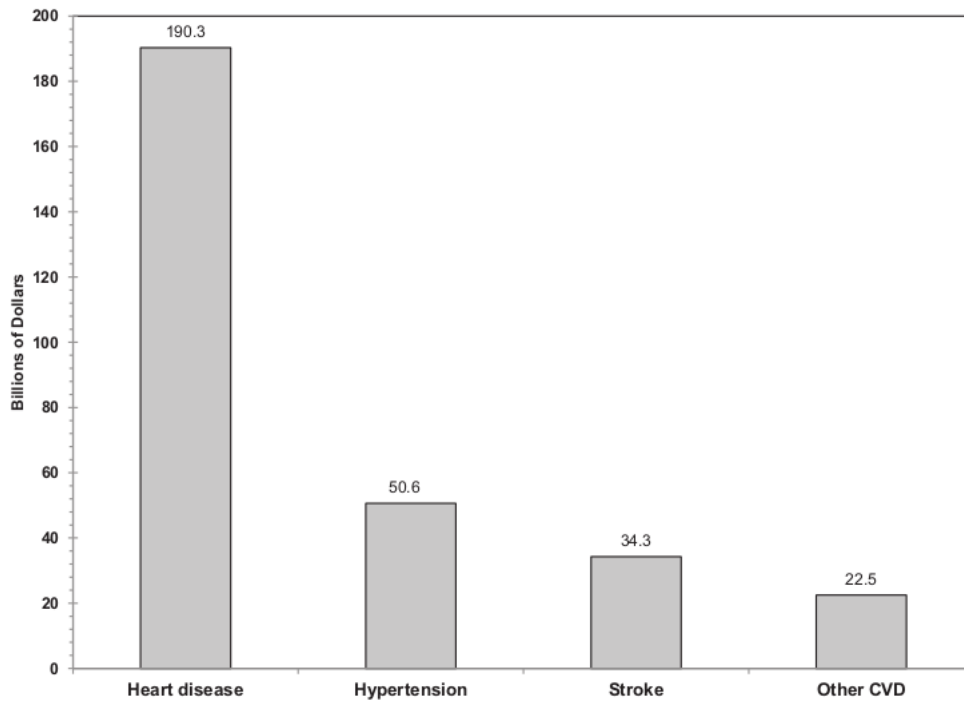


Figure 1.1: Direct and indirect costs (in billions of dollars) of major cardiovascular diseases (CVD) (United States: 2008). Source: National Heart, Lung, and Blood Institute.

to predict the performance of their devices in virtual patients prior to deployment in human trials. These virtual clinical trials prior to animal and human studies could result in safer designs, reduced development costs, and shorter time-to-market.

	CVD deaths	CHD deaths	Stroke deaths	Total deaths
Men ages 35-74 y				
Russian Federation (2006)	1299.2	706	351.4	2683.4
Bulgaria (2008)	803.7	219.4	218.2	1554.3
Lithuania (2009)	734.7	444.6	138.3	1842.3
Romania (2009)	677.9	276.4	200.2	1572.4
Slovakia (2005)	634.2	320.1	91.8	1528.3
Hungary (2009)	605.6	319.1	121.1	1652.3
Poland (2008)	495.2	180.0	100.8	1412.7
Croatia (2009)	419.3	202.2	113.6	1184.7
Czech Republic (2009)	386.6	198.6	64.4	1080.8
Kuwait (2009)	319.6	187.0	62.1	563.9
Finland (2009)	284.4	170.0	43.8	833.2
United States (2008)	256.0	149.2	30.0	862.7
Greece (2009)	251.6	136.7	50.8	721.6
Germany (2006)	242.1	125.3	34.5	788.5
Ireland (2009)	210.0	140.6	29.2	701.3
Belgium (2005)	209.6	99.5	35.9	821.7
Denmark (2006)	206.6	84.8	45.6	865.6
New Zealand (2007)	204.2	135.6	29.1	635.7
United Kingdom (2009)	202.0	125.8	29.9	687.6
Canada (2004)	198.3	130.8	24.2	705.3
Austria (2009)	189.3	110.2	26.3	736.3
Sweden (2008)	187.8	109.4	31.0	591.8
Portugal (2009)	168.7	61.3	62.1	825.3
Spain (2008)	168.2	77.6	33.7	714.0
Italy (2007)	160.6	75.6	29.9	625.8
Netherlands (2009)	157.9	64.6	24.6	649.4
Israel (2007)	156.3	86.3	32.5	655.9
Norway (2009)	154.4	84.6	29.0	607.0
Switzerland (2007)	150.4	78.2	16.6	587.5
Japan (2009)	145.2	46.5	52.2	605.0
France (2007)	145.0	57.1	26.5	774.6
Australia (2006)	141.3	88.9	22.0	553.4
Korea, South (2009)	138.4	41.0	65.9	783.6

Table 1.1: International men death rates (per 100 000 population) for total CVD, CHD, stroke, and total deaths in selected countries (revised May 2011). CVD indicates cardiovascular disease; CHD, coronary heart disease. Sources: The World Health Organization, National Center for Health Statistics, and National Heart, Lung, and Blood Institute.

	CVD deaths	CHD deaths	Stroke deaths	Total deaths
Women ages 35–74 y				
Russian Federation (2006)	521.4	237.1	189.2	1001.8
Bulgaria (2008)	368.6	70.9	120.6	699.3
Romania (2009)	325.5	109.5	116.2	706.0
Slovakia (2005)	269.5	129.5	41.9	643.7
Lithuania (2009)	253.9	127.5	73.8	648.6
Kuwait (2009)	246.1	94.8	56.1	568.1
Hungary (2009)	239.2	113.7	56.0	719.4
Croatia (2009)	190.8	71.9	68.7	520.1
Poland (2008)	181.5	51.6	50.1	570.0
Czech Republic (2009)	164.3	69.9	34.8	506.6
United States (2008)	129.2	59.5	23.5	544.7
Denmark (2006)	100.0	32.4	32.1	557.8
Germany (2006)	97.8	38.2	20.1	402.4
Greece (2009)	97.1	33.3	29.3	319.0
Belgium (2005)	94.4	30.8	24.8	436.3
New Zealand (2007)	89.8	43.9	21.7	418.2
United Kingdom (2009)	88.1	38.5	22.5	438.5
Ireland (2009)	86.8	40.9	21.9	419.8
Finland (2009)	83.4	36.1	23.0	377.8
Canada (2004)	83.1	42.8	17.3	432.7
Portugal (2009)	76.5	20.0	33.5	377.6
Austria (2009)	75.5	33.7	16.4	368.2
Sweden (2008)	74.6	35.5	18.5	374.1
Netherlands (2009)	74.0	20.6	20.1	416.8
Italy (2007)	67.3	22.2	18.2	326.0
Israel (2007)	65.4	22.2	17.3	388.7
Korea, South (2009)	63.5	41.0	33.2	312.3
Spain (2008)	62.4	18.7	17.8	304.4
Norway (2009)	60.5	26.3	15.2	377.0
Australia (2006)	60.4	26.8	16.3	327.5
Japan (2009)	54.4	12.8	22.7	266.9
Switzerland (2007)	54.1	19.4	12.4	327.6
France (2007)	51.3	12.1	13.9	346.0

Table 1.2: International women death rates (per 100 000 population) for total CVD, CHD, stroke, and total deaths in selected countries (revised May 2011). CVD indicates cardiovascular disease; CHD, coronary heart disease. Sources: The World Health Organization, National Center for Health Statistics, and National Heart, Lung, and Blood Institute.

1.2 The role of numerical simulations

The vascular system is highly complex and able to regulate itself: an excessive decrease in blood pressure will cause the smaller arteries (the arterioles) to contract and the heart rate to increase, whereas an excessive blood pressure is counter-reacted by a relaxation of the arterioles (which causes a reduction of the periphery resistance to the flow) and a decrease of the heart beat. Yet, it may happen that some *pathological conditions* develop. For example, the arterial wall may become more rigid, due to illness or excessive smoking habits, fat may accumulate in the arterial walls causing a reduction of the vessel section (a stenosis) and eventually an aneurysm or an atherosclerotic plaque.

The consequence of these pathologies on the blood field as well as the possible outcome of a surgical intervention to cure them may be studied by *numerical simulations*, that are less invasive than in-vivo investigation, and far more accurate and flexible than in-vitro experiments (in addition they deal with ethical and practical limitations). Numerical models require patient's data (the initial and boundary conditions for the PDE systems, as well as geometrical data to characterize the shape of the computational domain) that can be generated by radiological acquisition through modern non-invasive data collection technologies, e.g., computerized tomography, magnetic resonance, doppler anemometry, etc. (see fig.1.2).

The progress in computational fluid dynamics (CFD), as well as the increase in computer power, has added the numerical experiments to the tools at disposal to medical researchers, biologists and bioengineers. For example, quantities like *shear stresses* on the endothelium surface, which are quite hard, if not impossible, to measure in vitro, can now be calculated from simulations carried out on real geometries obtained with three-dimensional reconstruction algorithms.

Besides their employment in medical research, numerical models of vascular flows can provide a virtual experimental platform to be used as *training system*. For instance, a technique now currently used to cure a stenosis is angioplasty, which consists of inflating a balloon positioned in the stenotic region by the help of a catheter. The balloon should squash the stenosis and approximately restore the original lumen area. The success of the procedure depends, among other factors, on the sensitivity of the surgeon and his ability of placing the catheter in the right position. A training system which couples virtual reality techniques with the simulation of the flow field around the catheter, the balloon and the vessel walls, employing geometries extracted from real patients, could well serve as training bed for new vascular surgeons. A similar perspective could provide specific design indications for the realization of surgical operations. For instance, numerical simulations could represent a tool for the design of new *prototypes*, or for devising prosthetic devices by the help of shape optimization theory. These numerical investigations can help the surgeon in understanding how the different surgical solutions may affect blood circulation and guide the choice of the most appropriate procedure for a specific patient. In such “virtual surgery” environments, the outcome of alternative treatment plans for the individual patient can be foreseen by simulations, yielding a new paradigm of the clinical practice which is referred to as “predictive medicine” (see [5]).

The European Union is improving the research in numerical simulation with the *Virtual Physiological Human Network of Excellence* (VPH NoE) program [6]. The VPH NoE is a project which aims to help support and progress European research in biomedical modelling and simulation of the human body. This will improve our ability to predict, diagnose and treat disease, and have a dramatic impact on the future of healthcare, the pharmaceutical and medical device industries. This program is designed to foster, harmonise and integrate pan-European research in the field of

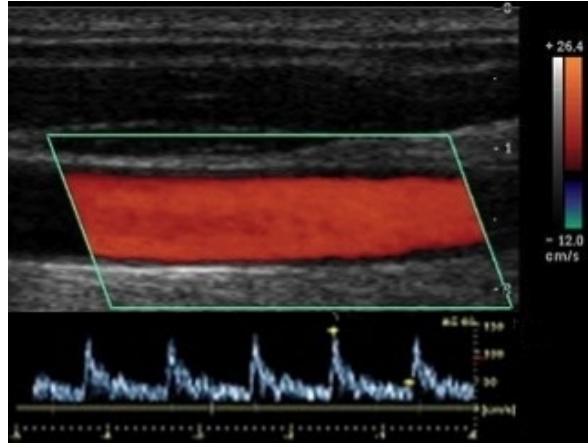
1. Patient-specific computer models for personalised and predictive healthcare,
2. ICT-based tools for modelling and simulation of human physiology and disease-related processes.

Another European research program is the *Mathematical Modelling and Simulation of the cardiovascular system* (MathCard) project, a five years long project started in 2009 and due to finish by the end of 2013 [7] whose principal investigator is professor Alfio Quarteroni. The goal of this program is to describe and simulate the anatomic structure and the physiological response of the human cardiovascular system in healthy or diseased states, developing different tasks:

- mathematical models for the integrated cardiovascular system;
- mathematical models of the interaction between circulation, tissue perfusion, biochemical and thermal regulation;
- modeling drug delivery in prosthetic implants;
- modeling electrical activity, fluid dynamics and wall mechanics of the heart;
- efficient methods for control and optimisation;
- risk evaluation;
- software development;
- further relevant clinical applications.



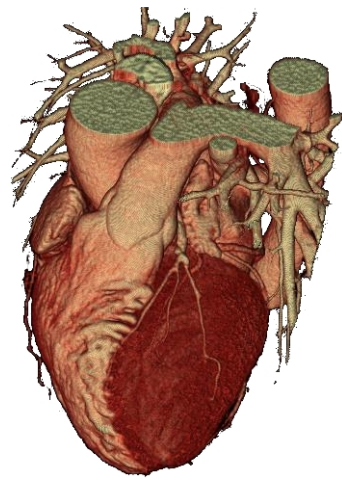
(a) MRI machine.



(b) EcolorDoppler of an abdominal aorta.



(c) Brain vessels in a MRI caption.



(d) CT angiography.

Figure 1.2: Examples of modern non-invasive data collection technologies.

Computational Haemodynamics. One of the most interesting and promising fields in numerical simulation is computational haemodynamics. It helps us to improve in the *understanding of the on-rise and the development of individual physiopathologies*. For example, geometrical reconstructions of an individual carotid morphology starting from angiographies, CT scans or MR images can be extensively used for evaluating the impact of the vessel shape on the wall shear stress and consequently on the possible development of pathologies. The separation of the blood flow in the vessel and the generation of a secondary motion are today recognized as potential factors for the development of atherosclerotic plaques. They may be induced by a particular vascular morphology, like a bifurcation (see fig.1.3). A detailed understanding of the local haemodynamic patterns and of their effects on the vessel wall is today a possibility thanks to accurate computer simulations (see fig.1.4).

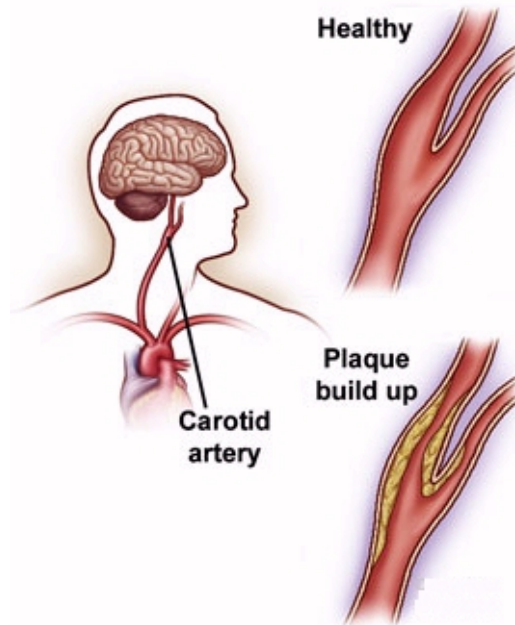


Figure 1.3: Carotid bifurcation in healthy and diseased state.

In vascular surgery, arterial bypass grafting is a common practice to treat coronary artery and peripheral vascular diseases. Nonetheless, over 50% of coronary artery bypass grafts fail within 10 years and more than 25% of infra-inguinal grafts within 5 years (see [9, 10, 11]). The principal cause is neo-intimal hyperplasia that may degenerate in atherosclerosis. A better understanding of local haemodynamics, like the detection of regions of low wall shear stress and of high residence time for blood particles, is of utmost importance to assess its correlation with atherogenesis [12].

A final example is the onrise and growth of cerebral aneurysms, a major pathology with many aspects still to be clarified. Here, complex interactions involving systemic factors, like hypertension or high cholesterol levels, and local blood flow features associated to particular vascular morphologies can induce the onrise of the pathology [13, 14, 15].

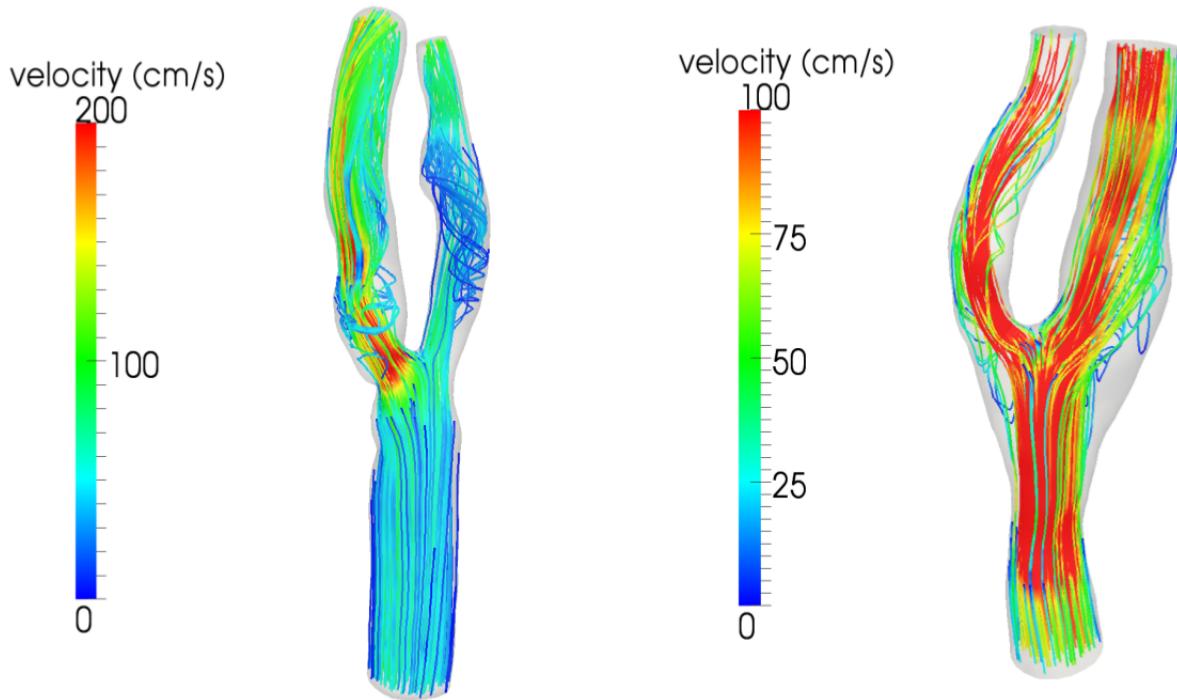


Figure 1.4: Fluid velocity [cm/s] on a patient-specific carotid bifurcation before (left) and after (right) carotid thromboendarterectomy. Taken from [8].

The computational haemodynamics can improve *prediction and design* too. In some engineering fields numerical simulations represent a consolidated tool for supporting design and the set up of a new prototype, with the aim of reducing the more expensive experimental assessment. Today, it is a common practice in cardiology the use of stents, to open a stenosis in a vessel. A stent is a little metallic tube permanently inserted in the artery that keeps it opened to let blood flowing normally. In particular, drug eluting stents contain medication substances able to reduce possible inflammation reactions and haemodynamic numerical simulations allow to design a film coating optimized for drug release [16, 17].

Another task of computational haemodynamics is *identification and optimization*. Scientific computing is nowadays used to solve not only direct, but also inverse problems, i.e. to help devising a solution which fulfills some prescribed optimality criteria. For example shape optimization techniques are applied to coronary artery bypass graft surgery, reducing surgical intervent failure probability [18]. The task could be therefore not only to simulate the fluid dynamics in a given vascular district or, more in general, in a compartment (i.e. a set of organs and tissues). Rather, the desired dynamics inside the compartment are specified (or given by measures in identification problems), and the computations have the role to identify the “parameters” of the problem ensuring that these features will be fulfilled at best. The major difficulty in solving optimization problems in general (and for life sciences in particular) is represented by the severe computational costs. Optimization solvers are usually based on iterative procedures and this could be prohibitively expensive if each iteration requires the

solution of a system of non-linear time-dependent partial differential equations. For this reason, specific techniques are under development, aiming at reducing the computational costs, as the reduced basis method [19].

For further informations and details about computational haemodynamics applications see [20, 21].

1.3 The present work

The work achieved in this thesis has been developed at MOX - Modeling and Scientific Computing laboratory (Dipartimento di Matematica "F. Brioschi", Politecnico di Milano).

In the first part of this thesis, we have implemented a parallel structural algorithm into the open-source finite-element library *LifeV* [22] (developed by Politecnico di Milano (MOX), Ecole Polytechnique Fédérale de Lausanne (CMCS, Switzerland), INRIA (REO/ESTIME, France) and Emory University (Sc. Comp, USA)). The goal is to improve the non-linear hyperelastic vessel wall model in fluid-structure interaction (FSI) simulations, including the *prestressed state* to vascular geometries reconstructed from radiological images [23, 24, 25, 26]. Our algorithm consists in a simple iterative procedure based on a fixed point method, and it aims at the calculation of deflated vascular geometries to simulate the prestressed state of arteries.

We have tested the algorithm from a quantitative point of view, using simple consistency test cases on a cube and a hollow cylinder. During our simulations we have considered two material models: St. Venant-Kirchhoff and Exponential. The former is a hyperelastic compressible material, while the latter is a nearly-incompressible hyperelastic material [27, 28, 29, 30]. These materials have properties similar to biological tissues as well known in literature [31, 32, 33, 34].

In the second part of this thesis, we described the Navier-Stokes equations in moving domains using the Arbitrary Lagrangian-Eulerian formulation, and the fluid-structure coupled problem with the partitioned procedure used to solve it. We used the algorithm in a parallel partitionated FSI solver, performing FSI simulations on a patient-specific carotid artery with and without the use of deflated geometries, evaluating the fluid velocity, the fluid pressure, the structure displacement and the wall-shear stress fields in both cases, highlighting the differences.

Summarizing, the present work has produced the following results:

- Development of a parallel algorithm to simulate prestressed state of arteries;
- Integration of the algorithm in a parallel FSI solver;
- Haemodynamics results on complex prestressed geometries.

1.4 Outline

In Chapter 2, we introduce the artery wall mechanics in the framework of three-dimensional finite elasticity. Moreover, we introduce the finite element formulation and the time discretization.

In Chapter 3, we explain the importance in recovering the correct initial geometry for fluid-structure interaction simulations. We introduce the algorithm implemented in this work and some numerical results on a cube and an hollow cylinder.

In Chapter 4, we introduce the incompressible Navier-Stokes equations in a moving domain using the Arbitrary Lagrangian-Eulerian formulation, their finite element formulation and time discretization.

Chapter 5 deals with the fluid-structure interaction problem and the partitioned algorithms used for the numerical solution.

In Chapter 6, we present an haemodynamic problem on a real carotid geometry showing the effectiveness of deflated geometries as initial configurations in FSI simulations. We compare FSI results on inflated and deflated patient-specific carotid, highlighting differences in the displacement, velocity, pressure field, and in the wall shear stress (WSS) haemodynamic factor.

Chapter 2

Artery wall mechanics

In the first part of this chapter a description of the artery wall is presented, with an insight on artery wall models and open problems. In the second part we provide some basic information on three-dimensional finite elasticity and finite element formulation needed in the following.

2.1 The artery wall

The arterial wall is a complex composite consisting of three primary types of constituents: structural proteins, resident cells, and a ground substance matrix. The primary structural proteins are elastin and fibrillar collagen. Elastin is the most biologically stable protein in the body (with a half life on the order of the lifespan of the organism) and it is the most elastic; it is capable of recoverable extensions of over 100%. Among the many members of the collagen family, particularly types I, III–V, and VIII in arteries, the fibrillar types I and III dominate overall wall stiffness. Finally, smooth muscle cells are capable of generating large, sustained contractile forces, which regulate the caliber of the artery and thus local blood flow.

The arterial wall is divided into three different layers: *tunica intima*, *tunica media* and *tunica adventitia* as shown in figure 2.1. The first layer is the innermost, it consists mainly of a single layer of endothelial cells, and does not contribute to the passive wall-mechanical response in healthy young arteries (because of its thinness) [33]. In a disease situation the mechanical properties of the wall may differ significantly from those of healthy arteries and, in some cases, the intima layer may become relevant [15]. We underline that pathological changes of the intimal components may be associated with *atherosclerosis*, the most common disease of the arterial wall. It consists in deposition of material, such as calcium, cellular waste products, and fibrin, that in an healthy situation are carried away by the blood flow. The resulting build-up is called *atherosclerotic plaque*, causing significant alterations in the mechanical behaviour of the arterial wall.

The second layer is the most important for arterial structural behaviour because it contains the elastin and the collagen, the main actors of the artery wall-mechanics. It consists of a complex three dimensional network of smooth muscle cells, elastin and collagen fibrils.

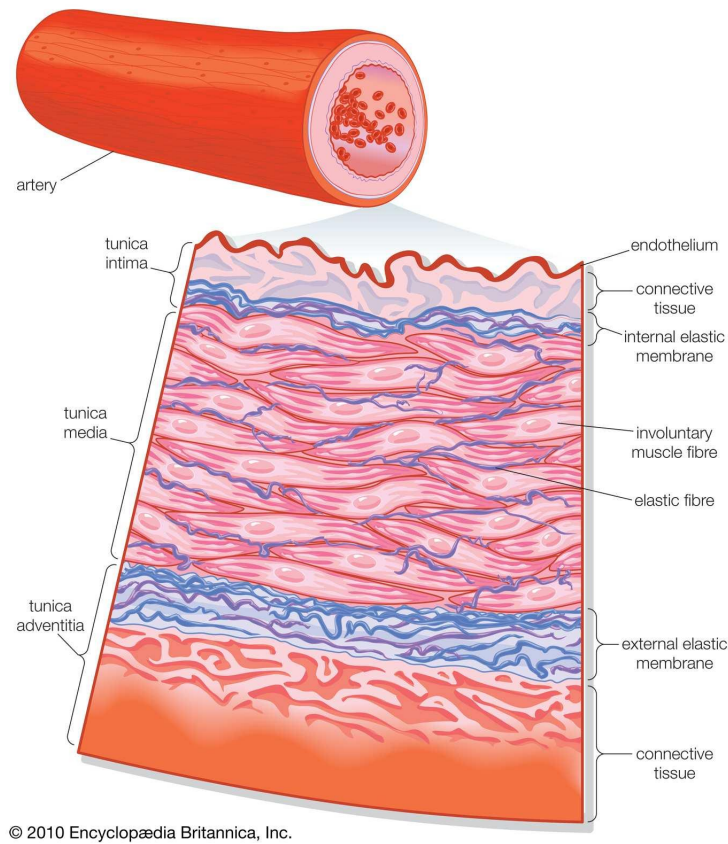


Figure 2.1: Artery wall layers.

Elastic layers, called fenestrated elastic laminae, separate the media into a varying number of well-defined concentric fiber reinforced layers [35].

Finally, the third arterial layer is the outermost and has a small contribution to structural response [13]. It consists mainly of collagen, fibroblasts, and fibrocytes, which are the cells that produce collagen and elastin. The adventitia is surrounded by connective tissue and its thickness strongly depends on the artery type.

Arteries are subdivided into two types, *elastic* and *muscular*. The first one presents an elastic behaviour while the second type is characterized by an important viscoelastic effect [31]. An important characteristic of the passive mechanical behaviour of an artery is that the stress-strain response during loading and unloading stages is highly non-linear. Indeed at low strain levels the structural response is mainly governed by elastina (soft tissue), while at high levels of strain the structural response is governed by fibers of collagen that stiffen the behaviour of the artery wall. Moreover, in large strain, the mechanical behaviour is anisotropic because of the collagen fibers structure. Therefore, when a vessel undergoes relatively large deformations it is expected that a reliable constitutive model for the vessel wall can be crucial for the accurate computation of some mechanical factors which are considered important in triggering the onset of a cardiovascular disease (e.g. aneurysms and atherosclerosis), or when

investigating the effect of changes of the arterial tissue behaviour due to factors like aging or hypertension.

2.1.1 State of the art

Constitutive laws In the last four decades, several models were proposed to describe the vessel wall dynamics using different theoretical frameworks like finite elasticity or mixture theory.

Modelling of soft tissues as fibre-reinforced elastic materials on the basis of the the invariant formulation of constitutive laws for materials with one or two families of fibres is now well established and widely used [34]. These formulations are based on the equations governing planar biaxial deformations since biaxial tests are commonly used in arterial mechanics to provide informations about material properties. However, biaxial tests alone are not sufficient to fully characterize the material properties of the anisotropic soft tissues [36] and this lack of data explains the need for some prior assumptions about the form of the constitutive laws.

Many research groups are oriented towards a description of the arterial wall that takes into account a *multi-mechanism*, coming from the elastin and collagen behaviour . The multi-mechanism models are based on the physiological assumption that the elastin works at low strain levels, then enters into a region of deformation in which collagen and elastin work together, and finally enters into a region of deformation in which only collagen works [37, 38, 39]. In figure 2.2a (taken from [40]) the internal pressure of an internal carotid artery is plotted, as a function of the circumferential stretch for several fixed values of the axial stretch. These curves show the characteristic stiffening response associated with the stretching of the collagen fibres following the relatively soft response associated with the deformation of the ground substance. We can see that the response is stiffer for higher axial pre-stretches. Figure 2.2b shows the pressure as a function of the axial stretch starting from an initial axial pre-stretch at zero pressure. The arterial tube elongates during inflation for low axial pre-stretches, but for larger ones the tube length decreases with pressure. The transition between these behaviours corresponds to an axial pre-stretch of about 1.15, when there is no change in length due to changes in pressure, a typical behaviour for human arteries [41].

Elastin can be considered an isotropic material with Young's modulus of about 1.1 MPa, while collagen is composed of fibers that make it anisotropic and has a stiffness greater than elastin with a Young's modulus of about 1.1GPa. From a computational point of view, this behavior can be effectively described using two different nonlinear constitutive laws, a *Neo-Hookean* hyperelastic material working under a certain threshold of strain and an *Exponential* hyperelastic material working above it.

Although arteries exhibit viscoelastic characteristics (creep, stress relaxation, and hysteresis), the assumption of *hyperelasticity* is sufficient in most physiologic and pathophysiologic cases. All constitutive relations must capture the nearly incompressible, nonlinear, anisotropic responses under finite deformations, however. Two general classes of relations have found most use: purely phenomenological relations in terms of the Green strain [42, 43]

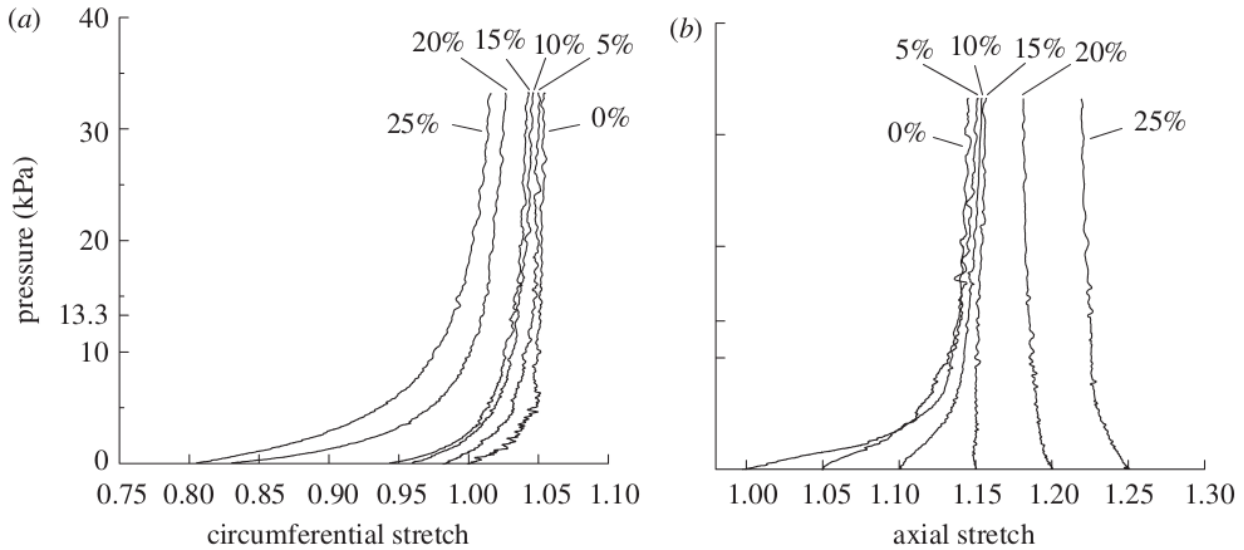


Figure 2.2: Representative pressure–stretch response of an intact internal carotid artery. (a) Pressure versus circumferential stretch for fixed values of the axial stretch. (b) Pressure versus axial stretch for different starting values of the axial stretch [40].

and structurally-motivated phenomenological relations [32, 44]. Although both types of relations are sufficient for computing wall stress in general, structurally-motivated relations using a rule-of-mixtures approach for the stress response are particularly useful in modeling stress mediated vascular growth and remodeling (G&R) in normal arteries as well as disease situations such as aneurysms and cerebral vasospasms.

Boundary conditions There are three primary surfaces of importance in arterial wall mechanics: the inner surface, in contact with the blood or implantable device, the outer surface, in contact with perivascular tissue, and the inlets/outlets generated by the truncation of the domain in view of the numerical simulations. The need to know traction boundary conditions on the inner surface of the artery (pressure and wall shear stress) reveals yet again the importance of knowing the haemodynamics. Fortunately, considerable information on this inner surface boundary condition can be gleaned from experiments, clinical measurements, or formal fluid–solid interaction (FSI) models. In contrast, tractions acting on the ends of the segment of interest (giving rise to the important axial pre-stretch) and the adventitial surface are not amenable to measurement in animal studies or in the clinical setting. Fortunately, it was discovered in the 1970s that arteries exhibit a remarkable property – the axial force needed to maintain the vessel at its *in vivo* axial stretch does not change during normal cyclic pressurizations. This constraint can be used in parameter estimations based on *in vivo* data [45] and it enables the semi-inverse method of finite elasticity to be used effectively. The outer boundary condition due to perivascular tissue is much more difficult to address, and only recently has received increased attention [46]. As in outlet boundary conditions for the

haemodynamics, lumped-parameter models will likely remain the best approach to address perivascular effects.

Fluid–structure interactions Given the importance of haemodynamics on intramural stresses and wall properties on the character of the blood flow, there has been recent progress in solving coupled blood flow–vessel wall interaction problems. The traditional approach to solve fluid–structure interaction problems in the arterial system is based on the *Arbitrary Lagrangian Eulerian* (ALE) method to solve the fluid problem in a moving domain. The coupled problem accounting for elastodynamics of the wall is solved using either a fully-coupled or a staggered approach [47].

For most researchers the preferred method of handling the moving interfaces involved in FSI modeling has been the arbitrary Lagrangian–Eulerian finite element formulation [47]. An alternative to the ALE approach is the *Coupled Momentum Method* (CMM) [48]. In this approach, wall motion is assumed to be small so that the fluid mesh is not updated, a membrane model for the vessel wall is employed, and node-on-node compatibility between the lateral surface of the fluid mesh and the vessel wall is enforced. These simplifications enable the elastodynamic equations for the wall to be embedded within the fluid dynamics equations, hence the only additional degrees of freedom are the (nonzero) velocities of the nodes on the lateral surface. The CMM is highly efficient for large scale fluid–structure interaction and wave propagation problems wherein underlying assumptions of small deformation and thin walls are valid. Indeed, the thin wall assumption is generally applicable (if the bending stiffness is accounted for appropriately) if the focus is on the haemodynamics because the fluid only needs to “know” the structural stiffness of the wall that constrains its motion, not detailed stress distributions throughout the wall.

For [49], the preferred method of handling the moving interfaces involved in FSI modeling has been the deforming-spatial-domain/stabilized space–time (DSD/SST) formulation [50, 51, 52, 53], which was introduced in 1991 as a general-purpose interface-tracking (i.e. moving mesh) technique for computation of flow problems with moving boundaries or interfaces. The formulation is based on the streamline-upwind/Petrov–Galerkin (SUPG) [54, 55] and pressure-stabilizing/Petrov–Galerkin (PSPG) [50, 56] methods.

Another alternative is the *immersed boundary method* introduced in [57]. In this method, the Navier–Stokes equations are generally solved on a Cartesian grid, which removes the effort needed to generate a body-fitted grid and enables the use of efficient numerical methods that can be parallelized in a relatively easy manner. The influence of objects on the flow is simulated by the addition of a force density (which represents the force of the surface of the object on the fluid) to the Navier–Stokes equations. This force density, if chosen properly, should result in a solution to the Navier–Stokes equation which satisfies the boundary conditions on the surface of the object. This is in contrast to other methods such as body-fitted curvilinear or unstructured grids, which require the grid to be built around or inside the objects being modeled.

Biological growth and remodeling Arteries retain a remarkable ability to adapt to changing haemodynamic conditions throughout life. The best known examples are that arteries increase (or decrease) in caliber in response to sustained increases (or decreases) in blood flow induced wall shear stresses [58] and they increase (or decrease) in thickness in response to sustained increases (or decreases) in blood pressure [59]. Indeed, perhaps the most important application of arterial wall mechanics is in understanding better how arteries adapt or maladapt under normal conditions, in disease, in injury, and in response to treatments that may include the use of implanted medical devices.

To date, two primary approaches have been proposed to address arterial growth and remodelling (G&R): the concept of kinematic growth (e.g. [60, 61] and the concept of a constrained mixture [62, 63]. The former can predict many cases of arterial adaptations by modeling the consequences of G&R but not the causes of such development. In contrast, the constrained mixture approach enables one to model the different rates of turnover of individual types of cells and matrix based on individual mass density production and removal (constitutive) functions. Such an approach promises to enable information on the mechanobiology to be incorporated directly.

A comprehensive model of vascular mechanobiology and biomechanics must synthesize analyses of the haemodynamics, wall mechanics, and growth and remodeling kinetics [64, 65]. Such models can be referred to as *fluid-structure-growth* (FSG) models. Because of the very different time scales between the cardiac cycle (i.e., seconds, for which FSI models hold) and periods of arterial adaptation (i.e., days to months, for which G&R models hold), such models can be formulated in a loosely coupled fashion [66].

2.1.2 Open problems

The main challenge to improve artery wall mechanics is prescribing the perivascular boundary conditions *in vivo* because fundamental to any analysis in continuum biomechanics is a basic knowledge of material behavior under conditions of interest. Such constitutive relations are formulated most easily *in vitro* wherein geometry, applied loads, and responses can be well controlled and measured. The primary motivation in biomechanics is to understand the *in vivo* condition, that is, to help patients who are in need.

There are five basic steps in the formulation of any constitutive relation: delineating the general characteristic behaviors, establishing an appropriate theoretical framework, identifying specific functional forms, calculating best-fit values of the material parameters, and evaluating the predictive capability of the final relations. Fortunately, it appears that we can formulate general constitutive relations for the arterial wall based on *in vitro* data and then focus primarily on identifying best-fit values of the associated material parameters from *in vivo* data, which requires accurate information on the geometry (from medical imaging) and haemodynamic loads (from imaging, pressure measurements, and CFD or FSI). Because of the potentially large number of material parameters in constitutive relations for the wall, particularly structurally-motivated ones, there is also a need to restrict the allowable parameter search space. Again, however, this can be accomplished based on *in vitro* findings, including bounds on typical mass fractions, orientations of individual constituents, extents

of residual and axial prestress, and so forth [46].

Most prior biomechanical analyses have employed simple boundary conditions, including parabolic velocity profiles at inlets, traction-free outlets, and no perivascular support. Most problems of clinical interest require more realistic conditions, however, with the computational domain for the fluid embedded within a closed-loop circulatory model and interactions included between the fluid and a solid that is constrained by perivascular tissue. This complexity presents new challenges related to prescribing boundary conditions.

First, there is the need to estimate parameters in reduced-order models of the distal resistance beds and to couple these models to the computational domain for the fluid. For the case of distributed network models, this involves specifying anatomic and physiologic parameters (e.g., branching patterns, vessel diameters and lengths) that cannot be resolved using standard noninvasive imaging (because of the micron diameter vessels). For lumped-parameter models of downstream or upstream portions of the circulation excluded from the computational domain, this necessitates assigning bulk resistances, impedances, compliance, or inertial terms. In either the distributed or the lumped-parameter reduced-order models, parameter values need to be “tuned” so the combined model matches available physiologic data, including measured blood pressures and flows. Without question, fluid–solid interactions in the arterial system depend strongly on the tissue or fluid outside the vessel of interest. For example, many portions of the vasculature are embedded in soft tissue (e.g., epicardial coronary arteries of the heart) or lie adjacent to hard tissues such as bones. Such support can have a dramatic stabilizing influence on wall dynamics and should be modeled when possible [67]. A second challenge, therefore, is the need to model the perivascular support and extract information on the degree of support via noninvasive imaging methods.

2.2 Three-dimensional finite elasticity

2.2.1 Kinematics

Three-dimensional finite elasticity describes the behaviour of a continuous body β in terms of kinematics, stress and deformation states. The body is assumed to occupy a compact domain in the three-dimensional Euclidean space, denoted by \mathbb{E} . β is made of material points whose position relative to a generic observer O at a time t defines the configuration of the body itself.

A configuration is a smooth-mapping of β onto a region of \mathbb{E} . It is possible to define one configuration that is constant in time, namely the reference configuration, which describes the position of each material point with respect to its position in the reference configuration. The reference configuration is also called *undeformed configuration*, while the current configuration is also called *deformed configuration*. A transformation from undeformed configuration denoted by $\widehat{\Omega}$ to current configuration, denoted by Ω , is defined by a one-to-one, orientation-preserving vector field \mathcal{L} :

$$\begin{aligned}\mathbf{x} &= \mathcal{L}(\widehat{\mathbf{x}}, t), \\ \widehat{\mathbf{x}} &= \mathcal{L}^{-1}(\mathbf{x}, t).\end{aligned}\tag{2.1}$$

where $\mathbf{x} \in \Omega$ and $\widehat{\mathbf{x}} \in \widehat{\Omega}$.

The position of a material point in the reference configuration is denoted by $\widehat{\cdot}$ (i.e. $\widehat{\mathbf{x}}$). Furthermore, the differential operators and the element of area or volume are indicated by $\widehat{\cdot}$ (i.e. $\widehat{\nabla}$, $\widehat{\partial\Omega}$, $\widehat{\Omega}$) when they are referred to the reference configuration. When it is clear from the context that a quantity belong to the reference configuration we omit $\widehat{\cdot}$.

Using the transformation from reference configuration to the current configuration, (2.1), the displacement field $\boldsymbol{\eta}$ in the reference configuration is defined as¹:

$$\boldsymbol{\eta}(\widehat{\mathbf{x}}) = \mathcal{L}(\widehat{\mathbf{x}}) - \widehat{\mathbf{x}}. \quad (2.2)$$

Moreover it is possible to define a primary measure of deformation \mathbf{F} called *deformation gradient*, as

$$\mathbf{F} = \widehat{\nabla} \mathcal{L} \quad \text{componentwise: } F_{ij} = \frac{\partial \mathcal{L}_i}{\partial \widehat{x}_j}. \quad (2.3)$$

In addition it is possible to introduce a symmetric positive-defined tensor called *right Cauchy-Green tensor* denoted by \mathbf{C} which measures the length of a vector $\delta\mathbf{x}$ after a generic deformation. Indeed, a vector defined in the reference configuration $\delta\widehat{\mathbf{x}}$ that follows the material points is transformed within the first order into the vector $\delta\mathbf{x} = \mathbf{F}\delta\widehat{\mathbf{x}}$ and the length of $\delta\mathbf{x}$ is given by: $|\delta\mathbf{x}|^2 = \delta\widehat{\mathbf{x}}^T (\mathbf{F}^T \mathbf{F}) \delta\widehat{\mathbf{x}}$. Hence it is convenient to introduce the right Cauchy-Green tensor:

$$\mathbf{C} = \mathbf{F}^T \mathbf{F}. \quad (2.4)$$

It is important for the following analysis to define the principal invariants, $I_1(\mathbf{C})$, $I_2(\mathbf{C})$, $I_3(\mathbf{C})$ of \mathbf{C} ; they are necessary to analyze homogeneous pure strain and to describe the hyperelastic constitutive laws. The three principal invariants are:

$$\begin{aligned} I_1(\mathbf{C}) &= \text{tr}(\mathbf{C}), \\ I_2(\mathbf{C}) &= \frac{1}{2}[(\text{tr}\mathbf{C})^2 - \text{tr}(\mathbf{C}^2)], \\ I_3(\mathbf{C}) &= \det(\mathbf{C}). \end{aligned} \quad (2.5)$$

We also introduce the *Green-Lagrange tensor* \mathbf{E} which is another useful measure of deformation:

$$\mathbf{E} = \frac{1}{2}(\mathbf{C} - \mathbf{I}). \quad (2.6)$$

The *Cauchy stress tensor* \mathbf{T}_s represents the state of stress of the elastic body β in the current configuration Ω . It is a symmetric second order tensor and it depends on the position \mathbf{x} and time t :

$$\mathbf{T}_s = \mathbf{T}_s(\mathbf{x}, t).$$

Here we assume that the reference configuration is at its natural state, that is the Cauchy stresses are everywhere zero.

¹For the displacement field in the reference configuration, we omit the superscript $\widehat{\cdot}$.

Through the Piola transformation it is possible to push back the state of stress of the elastic body β into the reference configuration $\hat{\Omega}$:

$$\mathbf{P} = J\mathbf{T}_s\mathbf{F}^{-T}, \quad (2.7)$$

where \mathbf{P} is called the *first Piola-Kirchhoff tensor*, which indeed describes the stress state in the reference configuration and $J = \det(\mathbf{F})$. We can also define the *second Piola-Kirchhoff tensor* \mathbf{S}

$$\mathbf{S} = \mathbf{F}^{-1}\mathbf{P} = J\mathbf{F}^{-1}\mathbf{T}_s\mathbf{F}^{-T}, \quad (2.8)$$

which is a symmetric tensor.

2.2.2 Equations of motion

It is possible to describe the equations of motion through the second law of dynamics. In fact it is well known that the rate of change of the linear momentum equals the sum of surface \mathbf{t} and volume forces \mathbf{f} . The equations of motion applied to an arbitrary volume $V(t)$, with boundary $\partial V(t)$ become:

$$\frac{D}{Dt} \int_{V(t)} \rho \dot{\boldsymbol{\eta}} dV = \int_{V(t)} \rho \mathbf{f} dV + \int_{\partial V(t)} \mathbf{t} dS, \quad (2.9)$$

where ρ is the density associated to the elastic body β and $\dot{\boldsymbol{\eta}}$ is the first time-derivative of the displacement. Defining the continuity of the mass:

$$\frac{D\rho}{Dt} + \rho \nabla \cdot \dot{\boldsymbol{\eta}} = 0, \quad (2.10)$$

where $\frac{D\rho}{Dt} = \frac{\partial \rho}{\partial t} + \dot{\boldsymbol{\eta}} \cdot \nabla \rho$, it is possible to rewrite the equations of motion using the transport theorem and (2.10):

$$\int_{V(t)} \rho \ddot{\boldsymbol{\eta}} dV = \int_{V(t)} \rho \mathbf{f} dV + \int_{\partial V(t)} \mathbf{t} dS, \quad (2.11)$$

where $\ddot{\boldsymbol{\eta}}$ is the second time-derivative of the displacement. The substitution of the stress vector with its representation by means of the Cauchy stress tensor \mathbf{T}_s and the use of the Gauss theorem allows to write:

$$\int_{V(t)} \rho \ddot{\boldsymbol{\eta}} dV = \int_{V(t)} \rho \mathbf{f} dV + \int_{\partial V(t)} \nabla \cdot \mathbf{T}_s dS. \quad (2.12)$$

This equation describes the motion by Eulerian variables in the current configuration.

It is more convenient to rewrite the equations of motion in terms of Lagrangian variables. From this point of view it is necessary to relate an infinitesimal volume and an infinitesimal oriented surface in $\Omega(t)$ to their counterpart in the reference configuration. Using the Jacobian J of the deformation gradient and the Piola transformation we have:

$$\begin{cases} d\Omega = Jd\widehat{\Omega} \\ \mathbf{n}dS = J\mathbf{F}^{-T}\widehat{\mathbf{n}}d\widehat{S}. \end{cases}$$

Using these relations it is possible to rewrite (2.9) in the reference configuration:

$$\int_{\widehat{V}} J\rho\ddot{\boldsymbol{\eta}} d\widehat{V} = \int_{\widehat{V}} J\rho\mathbf{f} d\widehat{V} + \int_{\partial\widehat{V}} J\mathbf{T}_s\mathbf{F}^{-T}\widehat{\mathbf{n}} d\widehat{S}. \quad (2.13)$$

The quantity $J\mathbf{T}_s\mathbf{F}^{-T}$ is the first Piola-Kirchhoff tensor and so the last equation becomes:

$$\int_{\widehat{V}} \widehat{\rho}\ddot{\boldsymbol{\eta}} d\widehat{V} = \int_{\widehat{V}} \widehat{\rho}\mathbf{f} d\widehat{V} + \int_{\partial\widehat{V}} \mathbf{P}\widehat{\mathbf{n}} d\widehat{S}. \quad (2.14)$$

Finally, through the Gauss theorem, it is possible to transform the surface integral into the volume integral:

$$\int_{\widehat{V}} \widehat{\rho}\ddot{\boldsymbol{\eta}} d\widehat{V} = \int_{\widehat{V}} \widehat{\rho}\mathbf{f} d\widehat{V} + \int_{\partial\widehat{V}} \widehat{\nabla} \cdot \mathbf{P} d\widehat{V}, \quad (2.15)$$

which is valid for any $\widehat{V} \subset \widehat{\Omega}$, therefore we may infer the differential equations of the linear momentum in the reference configuration:

$$\widehat{\rho}\ddot{\boldsymbol{\eta}} - \widehat{\nabla} \cdot \mathbf{P} = \widehat{\rho}\mathbf{f}. \quad (2.16)$$

The differential problem needs to be finalized by setting the initial and boundary conditions. The initial conditions read:

$$\begin{aligned} \boldsymbol{\eta}(\widehat{\mathbf{x}}, 0) &= \boldsymbol{\eta}_0(\widehat{\mathbf{x}}), \\ \ddot{\boldsymbol{\eta}}(\widehat{\mathbf{x}}, 0) &= \ddot{\boldsymbol{\eta}}_0(\widehat{\mathbf{x}}). \end{aligned} \quad (2.17)$$

while, the most common boundary conditions are the following:

- Dirichlet conditions:

$$\boldsymbol{\eta}(\widehat{\mathbf{x}}, t) = \mathbf{g}, \quad \widehat{\mathbf{x}} \in \widehat{\Gamma}_D; \quad (2.18)$$

- Neumann conditions:

$$\mathbf{P}\widehat{\mathbf{n}}(\widehat{\mathbf{x}}, t) = \mathbf{h}, \quad \widehat{\mathbf{x}} \in \widehat{\Gamma}_N, \quad (2.19)$$

where $\widehat{\Gamma}_N \cup \widehat{\Gamma}_D \equiv \partial\widehat{\Omega}$, $\widehat{\Gamma}_N \cap \widehat{\Gamma}_D = \emptyset$.

Moreover, it is necessary to define the relation between the stress tensor and the kinematic variables to characterize the mechanical properties of the continuous body β . In particular it is necessary to define the constitutive law that characterizes the material model adopted. In the next paragraph, the hyperelastic materials are introduced from a general point of view.

2.2.3 Hyperelastic materials

The *constitutive law* relates the stress tensor \mathbf{T}_s and the kinematic variables. This relation characterizes the mechanical properties of the continuous body β . A material is defined *elastic* if the stress tensor \mathbf{P} depends on the position of the material points \mathbf{x} and the deformation gradient \mathbf{F} :

$$\mathbf{P} = \tilde{\mathbf{P}}(\mathbf{x}, \mathbf{F}). \quad (2.20)$$

When the previous relation is independent of the position of the material points \mathbf{x} the material is called *homogeneous*. Finally a material is *hyperelastic* when it does not dissipate energy during cyclic homogeneous deformations:

$$W_{cycle} = \int_0^T \int_{\hat{\Omega}} \mathbf{P} : \dot{\mathbf{F}} \, d\hat{\Omega} \, dt = 0, \quad (2.21)$$

along any deformation characterized by $\mathbf{x}(t = T) = \mathbf{x}(t = 0)$ at any point of β .

To define an hyperelastic material it is common to introduce the strain-energy function \bar{W} that represents the amount of elastic energy locally stored in the body β during the deformation \mathcal{L} . The form of the strain-energy function characterizes a material from another one. In addition, for hyperelastic materials it is common to distinguish between compressible, nearly incompressible and incompressible materials.

Hyperelastic compressible materials. An admissible homogeneous deformation for compressible materials reads:

$$\mathcal{L}(\hat{\mathbf{x}}, t) = \mathbf{F}(t)\hat{\mathbf{x}} + \mathbf{c}(t), \quad (2.22)$$

with the constraint $J > 0$. With the change of variable $t \rightarrow \mathbf{F}(t)$ the equation (2.21) becomes:

$$W_{cycle} = vol(\hat{\Omega}) \int_{\mathbf{F}(0)}^{\mathbf{F}(\tau)=\mathbf{F}(0)} \tilde{\mathbf{P}}(\mathbf{F}) : d\mathbf{F} = 0. \quad (2.23)$$

This relation implies that it must exist a scalar function whose gradient is equal to the first Piola-Kirchhoff stress tensor \mathbf{P} . In particular this scalar function is exactly the strain-energy function \bar{W} previously defined, thus it is possible to write

$$\mathbf{P}(\mathbf{F}) = \frac{\partial \bar{W}(\mathbf{F})}{\partial \mathbf{F}}. \quad (2.24)$$

The strain-energy function \bar{W} has to satisfy the *axiom of frame indifference*. In particular \bar{W} must be independent of rigid motion, since it depends only on the deformation \mathcal{L} . We can explain this concept introducing a generic rotation tensor \mathbf{R} . The axiom of frame indifference, in this case, reads

$$\bar{W}(\mathbf{R}\mathbf{F}) = \bar{W}(\mathbf{F}). \quad (2.25)$$

Choosing $\mathbf{R} = \sqrt{\mathbf{C}\mathbf{F}^{-1}}$ it is possible to rewrite the equation (2.25) as

$$\bar{W}(\mathbf{F}) = \bar{W}(\sqrt{\mathbf{C}}) := \tilde{W}(\mathbf{C}). \quad (2.26)$$

Hence the axiom of frame indifference implies that the strain-energy function depends only on the right Cauchy-Green tensor \mathbf{C} . Using equation (2.24) and the definition of \mathbf{F} we have

$$d\bar{W} = \frac{\partial \widetilde{W}(\mathbf{C})}{\partial \mathbf{C}} : d\mathbf{C}. \quad (2.27)$$

Finally, using the definition (2.4), the symmetry of the right Cauchy-Green tensor and using the chain rule

$$d\bar{W} = \frac{\partial \widetilde{W}(\mathbf{C})}{\partial \mathbf{C}} : d\mathbf{C} = 2\mathbf{F} \frac{\partial \widetilde{W}(\mathbf{C})}{\partial \mathbf{C}} : d\mathbf{F}, \quad (2.28)$$

the first Piola-Kirchhoff stress tensor assumes the following form

$$\mathbf{P} = 2\mathbf{F} \frac{\partial \widetilde{W}}{\partial \mathbf{C}}. \quad (2.29)$$

By inversion of the relation (2.7) it is possible to define also the Cauchy stress tensor \mathbf{T}_s that reads

$$\mathbf{T}_s = 2J^{-1}\mathbf{F} \frac{\partial \widetilde{W}}{\partial \mathbf{C}} \mathbf{F}^T. \quad (2.30)$$

To rewrite the strain-energy function for isotropic materials it is possible to use the *Rivlin-Ericksen* representation theorem:

Theorem 2.2.1. *For any isotropic hyperelastic materials the strain-energy function can be written as:*

$$\widetilde{W}(\hat{\mathbf{x}}, \mathbf{F}) = W(\hat{\mathbf{x}}, I_1(\mathbf{C}), I_2(\mathbf{C}), I_3(\mathbf{C})). \quad (2.31)$$

For further information and proof of the theorem see [29].

Hence, for isotropic hyperelastic materials the expression that defines the stress tensors, (2.29) and (2.30), can be rewritten only as a function of first derivative of the principal invariants of the right Cauchy-Green tensor \mathbf{C} . Employing the notation $I_j = I_j(\mathbf{C})$ the first Piola-Kirchhoff and Cauchy stress tensors becomes

$$\begin{aligned} \mathbf{P} &= 2\mathbf{F} \left[\left(\frac{\partial W}{\partial I_1} + I_1 \frac{\partial W}{\partial I_2} \right) \mathbf{I} - \frac{\partial W}{\partial I_2} \mathbf{C} + I_3 \frac{\partial W}{\partial I_3} \mathbf{C}^{-1} \right], \\ \mathbf{T}_s &= 2I_3^{-1/2} \left[\left(\frac{\partial W}{\partial I_1} + I_1 \frac{\partial W}{\partial I_2} \right) \mathbf{B} - \frac{\partial W}{\partial I_2} \mathbf{B}^2 + I_3 \frac{\partial W}{\partial I_3} \mathbf{I} \right], \end{aligned} \quad (2.32)$$

where \mathbf{B} is the left Cauchy-Green tensor defined as $\mathbf{B} = \mathbf{F}\mathbf{F}^T$. Any compressible hyperelastic material depends on volume changes through the third principal invariant I_3 . Indeed, I_3 is related to J by the relation $I_3 = J^2$.

Hyperelastic incompressible materials. Incompressible materials have to satisfy the constraint $J = 1$, i.e. an incompressible material does not change volume during the deformation. An admissible deformation for this kind of materials is

$$\begin{cases} \mathcal{L}(\widehat{\mathbf{x}}, t) = \mathbf{F}(t)\widehat{\mathbf{x}} + \mathbf{c}(t), \\ \det(\mathbf{F}) = 1. \end{cases} \quad (2.33)$$

It is possible to prove [29] that the first Piola-Kirchhoff tensor has the following expression

$$\mathbf{P} = \frac{\partial \overline{W}}{\partial \mathbf{F}}(\mathbf{F}) - p \frac{\partial J}{\partial \mathbf{F}}, \quad (2.34)$$

where p is a scalar field called *pressure*. As for compressible materials, the axiom of frame indifference implies that \overline{W} is a function of right Cauchy-Green tensor \mathbf{C} only. So, it is possible to derive the following relations for the stress tensors

$$\mathbf{P} = 2\mathbf{F} \frac{\partial \widetilde{W}}{\partial \mathbf{C}} - p\mathbf{F}^{-T}, \quad T_s = 2\mathbf{F} \frac{\partial \widetilde{W}}{\partial \mathbf{C}} \mathbf{F}^T - p\mathbf{I}. \quad (2.35)$$

Using the same considerations made for compressible materials it is possible to define the stress tensors as a function of the invariants of \mathbf{C}

$$\mathbf{P} = 2 \left(\frac{\partial W}{\partial I_1} + I_1 \frac{\partial W}{\partial I_2} \right) \mathbf{F} - 2 \frac{\partial W}{\partial I_2} \mathbf{F} \mathbf{C} - p\mathbf{F}^{-T}. \quad (2.36)$$

For incompressible materials the hydrostatic pressure plays the role of Lagrange multiplier associated to the incompressibility constraint $J = 1$.

Hyperelastic nearly incompressible materials. A nearly incompressible material can be associated to any incompressible material. Indeed, it is possible to demonstrate that for any strain energy function of an incompressible material W_{inc} there exists a nearly incompressible material with the following constitutive law

$$P = \frac{\partial W_\epsilon}{\partial \mathbf{F}}(\widehat{\mathbf{x}}, \mathbf{I} + \nabla \boldsymbol{\eta}), \quad (2.37)$$

where

$$W_\epsilon = W_{inc}(\widehat{\mathbf{x}}, [\det(\mathbf{F})]^{-1/3} \mathbf{F}) + \frac{1}{2\epsilon} (\det \mathbf{F} - 1)^2,$$

with ϵ a small parameter.

For practical applications it is common to divide the strain-energy function into two parts. The first one is the isochoric part W_{iso} that preserving volume during deformation. The second one is the volumetric part W_{vol} that depends on the Jacobian of the deformation gradient J

$$W(I_1(\overline{\mathbf{C}}), I_2(\overline{\mathbf{C}}), J) = W_{iso}(I_1(\overline{\mathbf{C}}), I_2(\overline{\mathbf{C}})) + W_{vol}(J), \quad (2.38)$$

where $\bar{\mathbf{C}}$ is the so-called *unimodular right Cauchy-Green tensor*, defined as $\bar{\mathbf{C}} = J^{-2/3}\mathbf{C}$ and such that $\det(\bar{\mathbf{C}}) = 1$.

The nearly incompressible materials are preferred to the incompressible materials because it is more common to have small compressibility in the hyperelastic materials and typically also in the biological tissues [32]. For this reason the use of nearly incompressible materials is the correct choice to well describe the arterial wall. Moreover, the problem is simpler than in incompressible materials since we do not have to treat the incompressibility constraint. Nevertheless, the price to pay for the simplicity of the formulation is that the resulting problem is badly conditioned.

2.2.4 Structural models within this work

In this work, two structural models which are commonly used in literature to describe the arterial tissue have been used. Namely, St.Venant-Kirchhoff and Exponential models. They have been developed in the framework of nonlinear finite elasticity [27]. From the mathematical point of view, these models describe the biological tissue as a compressible (the former) and nearly-incompressible (the latter), isotropic and hyperelastic material. From experimental observations, the arterial tissue is known to be incompressible or nearly-incompressible.

St.Venant-Kirchhoff model. The St.Venant-Kirchhoff model is the simplest compressible material. Its strain-energy function is defined as a quadratic isotropic function of the Green-Lagrange tensor:

$$W = W(\mathbf{E}) = \frac{\lambda}{2}(\text{tr}\mathbf{E})^2 + \mu\text{tr}(\mathbf{E}^2). \quad (2.39)$$

where λ and μ are the first and the second Lamè constants of the material:

$$\lambda = \frac{\nu E}{(1 + \nu)(1 - 2\nu)}, \quad (2.40)$$

$$\mu = \frac{E}{2(1 + \nu)}, \quad (2.41)$$

where ν and E are respectively the Poisson's ratio and the Young modulus. Using first equation of (2.32) it is possible to define the corresponding first Piola-Kirchhoff stress tensor in terms of \mathbf{F} and \mathbf{E} :

$$\mathbf{P} = \frac{\lambda}{2}(I_1(\mathbf{C}) - 3)\mathbf{F} - \mu\mathbf{F} + \mu\mathbf{F}\mathbf{C}. \quad (2.42)$$

It is more convenient to rewrite (2.42) in terms of displacements $\boldsymbol{\eta}$:

$$\begin{aligned}
 \mathbf{P}(\boldsymbol{\eta}) &= \lambda(\nabla \cdot \boldsymbol{\eta})\mathbf{I} + \mu(\nabla\boldsymbol{\eta} + \nabla\boldsymbol{\eta}^T) \\
 &+ \frac{\lambda}{2}(\nabla\boldsymbol{\eta} : \nabla\boldsymbol{\eta})\mathbf{I} + \mu\nabla\boldsymbol{\eta}^T\nabla\boldsymbol{\eta} \\
 &+ \lambda(\nabla \cdot \boldsymbol{\eta})\nabla\boldsymbol{\eta} + \frac{\lambda}{2}(\widehat{\nabla}\boldsymbol{\eta} : \widehat{\nabla}\boldsymbol{\eta})\widehat{\nabla}\boldsymbol{\eta} \\
 &+ \mu\widehat{\nabla}\boldsymbol{\eta}(\widehat{\nabla}\boldsymbol{\eta} + \widehat{\nabla}\boldsymbol{\eta}^T) + \mu\widehat{\nabla}\boldsymbol{\eta}\widehat{\nabla}\boldsymbol{\eta}^T\widehat{\nabla}\boldsymbol{\eta}.
 \end{aligned} \tag{2.43}$$

This material does not satisfies the constraint of *policonvexity* [68, 30]. Because of this, it is not usually used for problems with large levels of deformation.

Exponential nearly incompressible model. The exponential model is a nearly incompressible material. In particular, this material is widely used for soft biological tissues like the walls of the arteries. The strain-energy function, also in this case, is divided into isochoric and volumetric part

$$W = \frac{\alpha}{2\gamma}(e^{\gamma(I_1(\overline{\mathbf{C}})-3)} - 1) + \frac{\kappa}{4}[(J - 1)^2 + (\ln J)^2], \tag{2.44}$$

where α , γ and κ are respectively the *shear modulus*, the *exponential coefficient* and *bulk modulus*. The first Piola-Kirchhoff stress tensor after some calculation reads

$$\mathbf{P} = \alpha J^{-2/3} \left(\mathbf{F} - \frac{1}{3}I_1(\mathbf{C})\mathbf{F}^{-T} \right) e^{\gamma(I_1(\overline{\mathbf{C}})-3)} + J \frac{\kappa}{2} \left(J - 1 + \frac{1}{J}\ln J \right) \mathbf{F}^{-T}. \tag{2.45}$$

In this case the mathematical problem is well-posed, because the strain-energy function W satisfies the policonvexity constraint. It is possible to relate κ and α with the Poisson's ratio and the Young modulus

$$\kappa = \frac{E}{3(1 - 2\nu)}, \tag{2.46}$$

$$\alpha = \frac{E}{2(1 + \nu)}, \tag{2.47}$$

for the consistency of the nonlinear constitutive laws with the linear constitutive law, in the region of small deformations. The parameter γ is peculiar of this kind of material and tunes the stiffness for large displacements. In [29] it is suggested to use a parameter κ in the following range

$$\mu 10^2 \leq \kappa \leq \mu 10^6.$$

This choice does not influence strongly the comparison between materials because the stress-strain response in the region of small deformations is very similar for nonlinear structural models and linear elasticity also with such parameters. However, for a systematic comparative analysis between the different constitutive laws, could be necessary to use the relations (2.46) and (2.47).

2.3 Finite-element formulation

The finite-element formulation is the numerical approximation considered within this work for the spatial variables. The solution of a time-varying problem needs also a temporal scheme to integrate the equations. This leads to the solution of a linear system at each time step. In this section we give a brief explanation of these issues.

2.3.1 Weak formulation of the structural problem

We derive the weak form in a formal way by multiplying equation (2.16) by a test function \mathbf{v} and integrating on $\widehat{\Omega}$

$$\int_{\widehat{\Omega}} \widehat{\rho} \ddot{\boldsymbol{\eta}} \cdot \mathbf{v} d\widehat{\Omega} = \int_{\widehat{\Omega}} \widehat{\rho} \mathbf{f} \cdot \mathbf{v} d\widehat{\Omega} + \int_{\widehat{\Omega}} (\widehat{\nabla} \cdot \mathbf{P}) \cdot \mathbf{v} d\widehat{\Omega}. \quad (2.48)$$

In particular the test function has to respect the constraint

$$\mathbf{v} = \mathbf{0} \quad \text{on} \quad \widehat{\Gamma}_D. \quad (2.49)$$

Using the Gauss theorem and the Dirichlet boundary conditions (2.18) we obtain

$$\int_{\widehat{\Omega}} \widehat{\rho} \ddot{\boldsymbol{\eta}} \cdot \mathbf{v} d\widehat{\Omega} = \int_{\widehat{\Omega}} \widehat{\rho} \mathbf{f} \cdot \mathbf{v} d\widehat{\Omega} - \int_{\widehat{\Omega}} \widehat{\nabla}(\mathbf{v}) : \mathbf{P} d\widehat{\Omega} + \int_{\widehat{\Gamma}_N} \widehat{\mathbf{h}} \cdot \mathbf{v} d\widehat{\gamma}. \quad (2.50)$$

If we assume that \mathbf{v} is a velocity, so, $\widehat{\nabla}(\mathbf{v})$ is equal to $\delta \dot{\mathbf{F}}$ and the last equation assumes the following expression

$$\int_{\widehat{\Omega}} \widehat{\rho} \ddot{\boldsymbol{\eta}} \cdot \mathbf{v} d\widehat{\Omega} = \int_{\widehat{\Omega}} \widehat{\rho} \mathbf{f} \cdot \mathbf{v} d\widehat{\Omega} - \int_{\widehat{\Omega}} \delta \dot{\mathbf{F}} : \mathbf{P} d\widehat{\Omega} + \int_{\widehat{\Gamma}_N} \widehat{\mathbf{h}} \cdot \mathbf{v} d\widehat{\gamma}. \quad (2.51)$$

In particular, we are interested on the stiffness term $\int_{\widehat{\Omega}} \delta \dot{\mathbf{F}} : \mathbf{P} d\widehat{\Omega}$ that depends on the constitutive law adopted.

We are now in the position of giving the correct functional setting of (2.16) by employing the *Sobolev spaces* introduced in the appendix.

Weak-formulation 2.1. (*Continuous setting*). For any $t > 0$ find $\boldsymbol{\eta} = \boldsymbol{\eta}(t) \in \mathbf{V}(\widehat{\Omega})$:

$$\left\{ \begin{array}{l} \int_{\widehat{\Omega}} \widehat{\rho} \ddot{\boldsymbol{\eta}} \cdot \mathbf{v} d\widehat{\Omega} + a(\boldsymbol{\eta}, \mathbf{v}) = F(\mathbf{v}) \quad \forall \mathbf{v} \in \mathbf{V}(\widehat{\Omega}), \\ \boldsymbol{\eta}(0) = \boldsymbol{\eta}_0, \\ \dot{\boldsymbol{\eta}}(0) = \dot{\boldsymbol{\eta}}_0. \end{array} \right. \quad (2.52)$$

where

$$\mathbf{V}(\widehat{\Omega}) = \{ \mathbf{v} \in \mathbf{H}^1(\widehat{\Omega}) : \mathbf{v}|_{\widehat{\Gamma}_N} = \mathbf{0} \},$$

2.3. Finite-element formulation

and bilinear form $a(\cdot, \cdot)$ and right-hand side $F(\cdot)$ assume the following definitions

$$\begin{aligned} a(\boldsymbol{\eta}, \mathbf{v}) &= \int_{\widehat{\Omega}} \mathbf{P} : \widehat{\nabla} \mathbf{v} d\widehat{\Omega}, \\ F(\mathbf{v}) &= \int_{\widehat{\Gamma}_N} \widehat{\mathbf{h}} \cdot \mathbf{v} d\widehat{\gamma} + \int_{\widehat{\Omega}} \widehat{\rho} \mathbf{f} \cdot \mathbf{v} d\widehat{\Omega}. \end{aligned} \quad (2.53)$$

We have assumed, for simplicity, only homogeneous Dirichlet boundary conditions (for non-homogeneous Dirichlet boundary conditions see for example [69]).

The discrete version of (2.52) is obtained by the Galerkin method [69] where $\mathbf{V}(\widehat{\Omega})$ is replaced by a subspace \mathbf{V}_h of finite dimension. As usual a finite element formulation employs a mesh of the reference domain $\widehat{\Omega}$ to build \mathbf{V}_h . The computational domain is thus defined as:

$$\widehat{\Omega}_h = \bigcup_{K \in \widehat{\mathcal{T}}_h} K, \quad (2.54)$$

where K indicates the generic element of the mesh $\widehat{\mathcal{T}}_h$. Using Lagrangian finite elements, we have the following functional space:

$$\mathbf{X}_h^r = \{\mathbf{v}_h \in C^0(\widehat{\Omega}) : \mathbf{v}_h|_K \in \mathbb{P}_r, \forall K \in \widehat{\mathcal{T}}_h\} \quad r = 1, 2, \dots, \quad (2.55)$$

where \mathbb{P}_r is the polynomial space of degree r . \mathbf{V}_h is then a subspace of \mathbf{X}_h^r obtained by imposing the essential boundary conditions (2.18). The discrete version of (2.52) becomes:

Weak-formulation 2.2. (*Discrete setting*). For any $t > 0$ find $\boldsymbol{\eta}_h = \boldsymbol{\eta}_h(t) \in \mathbf{V}_h(\widehat{\Omega}_h)$:

$$\left\{ \begin{array}{l} \int_{\widehat{\Omega}_h} \widehat{\rho} \ddot{\boldsymbol{\eta}}_h \cdot \mathbf{v}_h d\widehat{\Omega} + a(\boldsymbol{\eta}_h, \mathbf{v}_h) = F(\mathbf{v}_h) \quad \forall \mathbf{v}_h \in \mathbf{V}_h(\widehat{\Omega}_h), \\ \boldsymbol{\eta}_h(0) = \boldsymbol{\eta}_{h_0}, \\ \dot{\boldsymbol{\eta}}_h(0) = \dot{\boldsymbol{\eta}}_{h_0}. \end{array} \right. \quad (2.56)$$

We can introduce the following approximate solution, associated to the discretization

$$\boldsymbol{\eta}_h(\widehat{\mathbf{x}}) = \sum_{j=1}^{3N_h} \eta_j \varphi_j(\widehat{\mathbf{x}}), \quad (2.57)$$

where $\eta_j, j = 1, 2, \dots, 3N_h$ are *unknown coefficients* and $\{\varphi_j, j = 1, 2, \dots, 3N_h\}$ are a *basis* of \mathbf{V}_h . If we define $\boldsymbol{\eta}$ as the vector whose components are the unknown coefficients η_j , it is possible to rewrite the discrete weak formulation as a system of ordinary differential equations (ODEs):

$$\mathbf{M}\ddot{\boldsymbol{\eta}} + \mathbf{k}(\boldsymbol{\eta}) = \mathbf{f}, \quad (2.58)$$

where

$$\begin{aligned}
 M_{ij} &= \int_{\widehat{\Omega}_h} \widehat{\rho} \varphi_j \varphi_i d\widehat{\Omega}, \\
 k(\boldsymbol{\eta})_i &= \int_{\widehat{\Omega}_h} \mathbf{P} \left(\sum_{j=1}^{3N_h} \eta_j \varphi_j(\widehat{\mathbf{x}}) \right) : \widehat{\nabla} \varphi_i d\widehat{\Omega}, \\
 f_i &= \int_{\widehat{\Omega}_h} \sum_{j=1}^{3N_h} h_{0j} \varphi_j \varphi_i d\widehat{\Omega} + \int_{\widehat{\Omega}_h} \sum_{j=1}^{3N_h} b_j \varphi_j \varphi_i d\widehat{\Omega}.
 \end{aligned} \tag{2.59}$$

In particular M_{ij} is the mass matrix, $k(\boldsymbol{\eta})_i$ is the non-linear stiffness vector and f_i is the forcing term.

2.3.2 Time discretization

The *Newmark scheme* can be used for the time-discretization. In particular, from equation (2.58), the time discretization is obtained in the following manner:

- Definition of a time interval $\mathbb{I} = [0, T]$;
- Uniform discretization of interval $\mathbb{I} \rightarrow \mathbb{I}_n = [t^n, t^{n+1}]$, with $\delta t = t^{n+1} - t^n$;
- Application of the Newmark scheme to system of ODEs (2.58)

$$\begin{cases}
 \mathbf{M}\ddot{\boldsymbol{\eta}}^{n+1} + \mathbf{k}(\boldsymbol{\eta}^{n+1}) = \mathbf{f}^{n+1}, \\
 \dot{\boldsymbol{\eta}}^{n+1} = \dot{\boldsymbol{\eta}}^n + \delta t[(1 - \theta)\ddot{\boldsymbol{\eta}}^n + \theta\ddot{\boldsymbol{\eta}}^{n+1}], \\
 \ddot{\boldsymbol{\eta}}^{n+1} = \frac{2}{\zeta\delta t^2}\boldsymbol{\eta}^{n+1} - \frac{2}{\zeta\delta t^2}(\boldsymbol{\eta}^n + \delta t\dot{\boldsymbol{\eta}}^n) - \frac{1 - \zeta}{\zeta}\ddot{\boldsymbol{\eta}}^n.
 \end{cases} \tag{2.60}$$

Hence:

$$\frac{2}{\delta t^2}\mathbf{M}\boldsymbol{\eta}^{n+1} + \zeta\mathbf{k}(\boldsymbol{\eta}^{n+1}) = \frac{2}{\delta t^2}\mathbf{M}(\boldsymbol{\eta}^n + \delta t\dot{\boldsymbol{\eta}}^n) - (1 - \zeta)\mathbf{k}(\boldsymbol{\eta}^n) + (1 - \zeta)\mathbf{f}^n + \zeta\mathbf{f}^{n+1}, \tag{2.61}$$

where we have set: $g^s = g(t^s)$. Here, ζ and θ are the coefficients of the Newmark's method.

The stability of the Newmark's method depends on the choice of ζ and θ . The following relations describe the stability conditions for a general Newmark's method applied to a second order dynamical system (see [70]):

$$\text{Unconditional stability} \quad \zeta \geq \theta \geq \frac{1}{2}, \tag{2.62}$$

$$\text{Conditional stability} \quad \theta \geq \frac{1}{2}, \quad \zeta < \theta, \quad \text{provided that} \quad \omega^h \delta t \leq \Omega_{crit}, \tag{2.63}$$

2.3. Finite-element formulation

where ω^h is the maximum natural frequency and Ω_{crit} is defined by the following relation:

$$\Omega_{crit} = \left(\frac{\theta}{2} - \frac{\zeta}{2} \right)^{-\frac{1}{2}}. \quad (2.64)$$

In table 2.1 we summarize the well-known members of the Newmark family of methods [70]

Table 2.1: Well-known Newmark methods.

Method	Type	ζ	θ	Stability condition	OA
average acceleration	Implicit	0.5	0.5	Unconditional	2
linear acceleration	Implicit	0.33	0.5	Conditional	2
Fox-Goodwin	Implicit	0.1667	0.5	Conditional	2
central difference	Explicit	0	0.5	Conditional	2

The choice of *average acceleration* method gives the optimal time convergence rate. However it may cause spurious oscillations since there is no numerical damping. It is possible to introduce damping by using a parameter ζ bigger than 0.5. For example the choice of $\zeta = 1$ and $\theta = 0.5$ is a fully dissipative method that cuts the spurious oscillations of the solution. This choice has been used for quasi-static problems. For dynamical problems it is necessary to have a good order of accuracy (OA), hence a second order method like average acceleration is preferred.

2.3.3 Linearization

As previously remarked, the stiffness term $\mathbf{k}(\boldsymbol{\eta})$ is non-linear with respect to the displacement $\boldsymbol{\eta}$. Hence to solve system (2.58) it is necessary to find the solution as the limit of solutions of suitable linearized problems. The linearization is obtained by the *Newton method* [71]. Indeed, the solution of (2.58) is equivalent to find the root $\boldsymbol{\eta}$ of the following problem:

$$\mathcal{Z}(\boldsymbol{\eta}) = \frac{2}{\delta t^2} \mathbf{M}\boldsymbol{\eta} + \zeta \mathbf{k}(\boldsymbol{\eta}) - \frac{2}{\delta t^2} \mathbf{M}(\boldsymbol{\eta}^n - \delta t \dot{\boldsymbol{\eta}}^n) + (1 - \zeta) \mathbf{k}(\boldsymbol{\eta}^n) - (1 - \zeta) \mathbf{f}^n - \zeta \mathbf{f}^{n+1} = 0, \quad (2.65)$$

where we have dropped the temporal current index $n + 1$ for the sake of clarity.

The unknown of the problem at each Newton iteration k is the displacement $\boldsymbol{\eta}^{(k)}$ which is set initially to $\boldsymbol{\eta}^n$. It is necessary to introduce the Jacobian² $J_{\mathcal{Z}}(\boldsymbol{\eta}^{(k)}) = D\mathcal{Z}(\boldsymbol{\eta}^{(k)})$ and the increment of solution $\delta \boldsymbol{\eta}^{(k+1)} = \boldsymbol{\eta}^{(k+1)} - \boldsymbol{\eta}^{(k)}$. Hence the Newton iterations become:

² $D\mathcal{Z}(\boldsymbol{\eta}^{(k)})$ is the directional derivative of $\mathcal{Z}(\boldsymbol{\eta}^{(k)})$. For more details see [13, 68].

Let $\boldsymbol{\eta}^{(0)} \in \mathbb{R}^3$ be given (for instance from the previous time-step), iterate for $k = 1, 2, \dots$ until convergence:

$$\begin{aligned} \text{solve} \quad & J_{\mathcal{Z}}(\boldsymbol{\eta}^{(k+1)})\delta\boldsymbol{\eta}^{(k)} = -\mathcal{Z}(\boldsymbol{\eta}^{(k)}), \\ \text{define} \quad & \boldsymbol{\eta}^{(k+1)} = \boldsymbol{\eta}^{(k)} + \delta\boldsymbol{\eta}^{(k+1)}, \end{aligned} \quad (2.66)$$

The test for convergence is the infinity norm of the residual. In particular, defining a tolerance $\varepsilon_R = \overline{\varepsilon_{R_{abs}}} + |\mathcal{Z}(\boldsymbol{\eta}^{(0)})| \overline{\varepsilon_{R_{rel}}}$ the stopping criterion for the Newton method is the following:

$$\|\mathcal{Z}(\boldsymbol{\eta}^{(k)})\|_{\infty} < \varepsilon_R. \quad (2.67)$$

To solve the linear system (2.66) the *preconditioned GMRES (P-GMRES) method* [71] has been used. The criterion to stop the P-GMRES method is to compare the norm of displacement $\boldsymbol{\eta}^{(k+1)}$ between iteration $\ell + 1$ and iteration ℓ of the method³. If $\varepsilon_{P-GMRES}$ is the tolerance of P-GMRES, the convergence test is:

$$\|\boldsymbol{\eta}_{(\ell+1)}^{(k+1)} - \boldsymbol{\eta}_{(\ell)}^{(k+1)}\|_{\infty} < \varepsilon_{P-GMRES}. \quad (2.68)$$

When P-GMRES method reaches to convergence, the solution is used to recompute the system (2.66) and in particular the residual of the system to verify the convergence of Newton method. The P-GMRES method will be more efficient when the number of iterations for convergence is small.

Summarizing, the steps for the solution of the nonlinear system (2.58) at each time-step are the following:

1. Choose an initial guess $\boldsymbol{\eta}^{(0)} \in \mathbb{R}^3$ and choose the tolerances ε_R and $\varepsilon_{P-GMRES}$;
2. Enter into Newton's loop, compute the jacobian and the residual;
3. If the residual is larger than ε_R , solve the linearized system (2.66) with P-GMRES method until $\|\boldsymbol{\eta}_{(\ell+1)}^{(k+1)} - \boldsymbol{\eta}_{(\ell)}^{(k+1)}\|_{\infty} < \varepsilon_{P-GMRES}$;
4. Re-build the system (2.66), until convergence.

2.3.4 Quadrature rules and computation of integrals

The calculation of the integrals required to build the matrices in the finite element formulation of the structural problem are obtained by *quadrature formulas*. For each quadrature point a local tensor is defined and a loop on quadrature points perform the computation of the integrals. In particular for a generic stiffness term, we have:

$$\int_K \mathbf{P}(\boldsymbol{\eta}_h) : \widehat{\nabla} \varphi_i dV_K \approx \sum_{ig} \mathbf{P}(\boldsymbol{\eta})_{ig} \widehat{\nabla} \varphi_{ig} \omega_{ig}, \quad (2.69)$$

where g indicate the *quadrature point* and ω_{ig} are the corresponding *weights*.

³ ℓ is the internal iteration of the P-GMRES method.

Stiffness term computation: St.Venant-Kirchhoff For St.Venant-Kirchhoff material, the first Piola-Kirchhoff tensor is defined in (2.43), here reported:

$$\begin{aligned}
 \mathbf{P}(\boldsymbol{\eta}) &= \lambda(\nabla \cdot \boldsymbol{\eta})\mathbf{I} + \mu(\nabla \boldsymbol{\eta} + \nabla \boldsymbol{\eta}^T) \\
 &+ \frac{\lambda}{2}(\nabla \boldsymbol{\eta} : \nabla \boldsymbol{\eta})\mathbf{I} + \mu \nabla \boldsymbol{\eta}^T \nabla \boldsymbol{\eta} \\
 &+ \lambda(\nabla \cdot \boldsymbol{\eta})\nabla \boldsymbol{\eta} + \frac{\lambda}{2}(\widehat{\nabla} \boldsymbol{\eta} : \widehat{\nabla} \boldsymbol{\eta})\widehat{\nabla} \boldsymbol{\eta} \\
 &+ \mu \widehat{\nabla} \boldsymbol{\eta}(\widehat{\nabla} \boldsymbol{\eta} + \widehat{\nabla} \boldsymbol{\eta}^T) + \mu \widehat{\nabla} \boldsymbol{\eta} \widehat{\nabla} \boldsymbol{\eta}^T \widehat{\nabla} \boldsymbol{\eta}.
 \end{aligned}$$

The calculation of the bilinear form $a(\boldsymbol{\eta}, \phi)$ is performed as:

$$\begin{aligned}
 \int_K \mathbf{P}(\boldsymbol{\eta}_h) : \widehat{\nabla} \phi \, dV_K &\approx \sum_{ig} \left(\lambda(\widehat{\nabla} \cdot \boldsymbol{\eta}_{ig})\mathbf{I} + \mu(\widehat{\nabla} \boldsymbol{\eta}_{ig} + \widehat{\nabla} \boldsymbol{\eta}_{ig}^T) \right. \\
 &+ \frac{\lambda}{2}(\widehat{\nabla} \boldsymbol{\eta}_{ig} : \widehat{\nabla} \boldsymbol{\eta}_{ig})\mathbf{I} + \mu \widehat{\nabla} \boldsymbol{\eta}_{ig}^T \widehat{\nabla} \boldsymbol{\eta}_{ig} \\
 &+ \lambda(\widehat{\nabla} \cdot \boldsymbol{\eta}_{ig})\widehat{\nabla} \boldsymbol{\eta}_{ig} + \frac{\lambda}{2}(\widehat{\nabla} \boldsymbol{\eta}_{ig} : \widehat{\nabla} \boldsymbol{\eta}_{ig})\widehat{\nabla} \boldsymbol{\eta}_{ig} \\
 &\left. + \mu \widehat{\nabla} \boldsymbol{\eta}_{ig}(\widehat{\nabla} \boldsymbol{\eta}_{ig} + \widehat{\nabla} \boldsymbol{\eta}_{ig}^T) + \mu \widehat{\nabla} \boldsymbol{\eta}_{ig} \widehat{\nabla} \boldsymbol{\eta}_{ig}^T \widehat{\nabla} \boldsymbol{\eta}_{ig} \right) \widehat{\nabla} \phi_{ig} \omega_{ig},
 \end{aligned} \tag{2.70}$$

For this material the linearization of the stiffness term is obtained using the *directional derivatives* [68, 13]:

$$\begin{aligned}
 DP(\boldsymbol{\eta})[\delta \boldsymbol{\eta}] &= \lambda(\widehat{\nabla} \cdot \delta \boldsymbol{\eta}) + \mu(\widehat{\nabla} \delta \boldsymbol{\eta} + (\widehat{\nabla} \delta \boldsymbol{\eta})) + \lambda \widehat{\nabla} \boldsymbol{\eta} : \widehat{\nabla} \delta \boldsymbol{\eta} \\
 &+ \lambda(\widehat{\nabla} \cdot \boldsymbol{\eta})\widehat{\nabla} \delta \boldsymbol{\eta} + \lambda(\widehat{\nabla} \cdot \delta \boldsymbol{\eta}) + \frac{\lambda}{2}(\widehat{\nabla} \delta \boldsymbol{\eta} : \widehat{\nabla} \boldsymbol{\eta})\widehat{\nabla} \boldsymbol{\eta} \\
 &+ \frac{\lambda}{2}(\widehat{\nabla} \boldsymbol{\eta} : \widehat{\nabla} \delta \boldsymbol{\eta})\widehat{\nabla} \boldsymbol{\eta} + \frac{\lambda}{2}(\widehat{\nabla} \boldsymbol{\eta} : \widehat{\nabla} \boldsymbol{\eta})\widehat{\nabla} \delta \boldsymbol{\eta} \\
 &+ \mu(\widehat{\nabla} \boldsymbol{\eta})^T \widehat{\nabla} \delta \boldsymbol{\eta} + \mu(\widehat{\nabla} \delta \boldsymbol{\eta})^T \widehat{\nabla} \boldsymbol{\eta} + \mu \widehat{\nabla} \boldsymbol{\eta} \widehat{\nabla} \delta \boldsymbol{\eta} + \mu \widehat{\nabla} \delta \boldsymbol{\eta} \widehat{\nabla} \boldsymbol{\eta} \\
 &+ \mu \widehat{\nabla} \boldsymbol{\eta}(\widehat{\nabla} \delta \boldsymbol{\eta})^T + \mu \widehat{\nabla} \delta \boldsymbol{\eta}(\widehat{\nabla} \boldsymbol{\eta})^T + \mu \widehat{\nabla} \delta \boldsymbol{\eta}(\widehat{\nabla} \boldsymbol{\eta})^T \widehat{\nabla} \boldsymbol{\eta} \\
 &+ \mu \widehat{\nabla} \boldsymbol{\eta}(\widehat{\nabla} \delta \boldsymbol{\eta})^T \widehat{\nabla} \boldsymbol{\eta} + \mu \widehat{\nabla} \boldsymbol{\eta}(\widehat{\nabla} \boldsymbol{\eta})^T \widehat{\nabla} \delta \boldsymbol{\eta}.
 \end{aligned} \tag{2.71}$$

Stiffness term computation: Exponential For exponential material, the first Piola-Kirchhoff tensor is defined in (2.45), here reported:

$$\mathbf{P} = \alpha J^{-2/3} \left(\mathbf{F} - \frac{1}{3} I_1(\mathbf{C}) \mathbf{F}^{-T} \right) e^{\gamma(I_1(\overline{\mathbf{C}}-3))} + J \frac{\kappa}{2} \left(J - 1 + \frac{1}{J} \ln J \right) \mathbf{F}^{-T}.$$

The calculation of the bilinear form $a(\boldsymbol{\eta}, \phi)$ is performed as:

$$\begin{aligned}
 \int_K \mathbf{P}(\boldsymbol{\eta}_h) : \widehat{\nabla} \phi \, dV_K &\approx \sum_{ig} \left[\alpha J^{-2/3} \left(\mathbf{F}_{ig} - \frac{1}{3} I_1(\mathbf{C}) \mathbf{F}_{ig}^{-T} \right) e^{\gamma(I_1(\overline{\mathbf{C}}-3))} \right. \\
 &\left. + J \frac{\kappa}{2} \left(J - 1 + \frac{1}{J} \ln J \right) \mathbf{F}_{ig}^{-T} \right] \widehat{\nabla} \phi_{ig} \omega_{ig}.
 \end{aligned} \tag{2.72}$$

We obtain the linearization of the stiffness term with respect to \mathbf{F} . In particular, we introduce the fourth order tensor \mathbb{C} :

$$\mathbb{C} = \frac{\partial \mathbf{P}}{\partial \mathbf{F}}, \quad (2.73)$$

and we linearize the stiffness term using the directional derivatives with respect to \mathbf{F} separating the isochoric and the volumetric part:

$$\begin{aligned} \mathbb{C}_{iso} : \delta \mathbf{F} &= -\frac{2}{3} \alpha e^{\gamma(I_1(\bar{\mathbf{C}}-3))} J^{-2/3} (1 + \gamma I_1(\bar{\mathbf{C}})) (\mathbf{F}^{-T} : \delta \mathbf{F}) \mathbf{F} \\ &+ \frac{2}{9} \alpha e^{\gamma(I_1(\bar{\mathbf{C}}-3))} I_1(\bar{\mathbf{C}}) (1 + \gamma I_1(\bar{\mathbf{C}})) (\mathbf{F}^{-T} : \delta \mathbf{F}) \mathbf{F}^{-T} \\ &- \frac{2}{3} \alpha e^{\gamma(I_1(\bar{\mathbf{C}}-3))} J^{-2/3} (1 + \gamma I_1(\bar{\mathbf{C}})) (\mathbf{F} : \delta \mathbf{F}) \mathbf{F}^{-T} \\ &+ 2 \alpha e^{\gamma(I_1(\bar{\mathbf{C}}-3))} J^{-4/3} (\mathbf{F} : \delta \mathbf{F}) \mathbf{F} \\ &+ \alpha e^{\gamma(I_1(\bar{\mathbf{C}}-3))} J^{-2/3} \delta \mathbf{F} \\ &+ \frac{2}{3} \alpha e^{\gamma(I_1(\bar{\mathbf{C}}-3))} I_1(\bar{\mathbf{C}}) \mathbf{F}^{-T} : \delta \mathbf{F}^T \mathbf{F}^{-T}. \end{aligned} \quad (2.74)$$

$$\begin{aligned} \mathbb{C}_{vol} : \delta \mathbf{F} &= \frac{\kappa}{2} J \left(2J - 1 + \frac{1}{J} \right) (\mathbf{F}^{-T} : \delta \mathbf{F}) \mathbf{F}^{-T} \\ &- \frac{\kappa}{2} (J^2 - J + \ln J) \mathbf{F}^{-T} \delta \mathbf{F}^T \mathbf{F}^{-T}. \end{aligned} \quad (2.75)$$

For further information [72].

Chapter 3

The recovering of the correct initial geometry

In this chapter we describe the available methodologies aimed at finding the correct initial reference configuration for FSI simulations in the human arteries for computational purposes. In the following, we also explain our approach to the problem and we describe the algorithm implemented in the parallel library LifeV [22]. Finally, numerical results on simple geometries are presented.

3.1 The need to use a deflated geometry

The mechanical behavior of blood vessel tissue is well described by means of large-deformation, three-dimensional solid or shell modeling [28, 42]. A total Lagrangian formulation with a hyperelastic constitutive law is typically employed. In hyperelasticity, the formulation relies on the existence of a unique stress-free configuration, which acts as a reference or initial configuration from which the displacement is computed. In vascular FSI analysis, patient-specific geometries of blood vessels are obtained from medical in vivo imaging data, for example from MRI or CT [73, 74]. The resulting images and reconstructed three-dimensional geometries could be assumed in first approximation as related to the diastole [73], and therefore represent a configuration which is submitted to an in vivo load. Indeed, the blood vessels are in a state of mechanical stress that puts them in equilibrium with the load coming from the blood flow at rest (i.e. diastolic blood pressure). Reconstructed structures are preloaded by the diastolic blood pressure (≈ 80 mmHg) and this preloading is commonly known as *prestress* load.

A common approach in FSI simulations to take into account this phenomenon is to neglect the predeformation of the object of interest under in vivo loads and to assume the obtained configuration as stress-free, leading to non-physical large deformations. This approach would be exact for the linear infinitesimal elasticity but it is not accurate when the vessel is described within finite elasticity. We can refer to fig.3.1 to better understand what happens. The blue line (B–D) is the relation that is experienced in vivo by the artery. This is the true behaviour

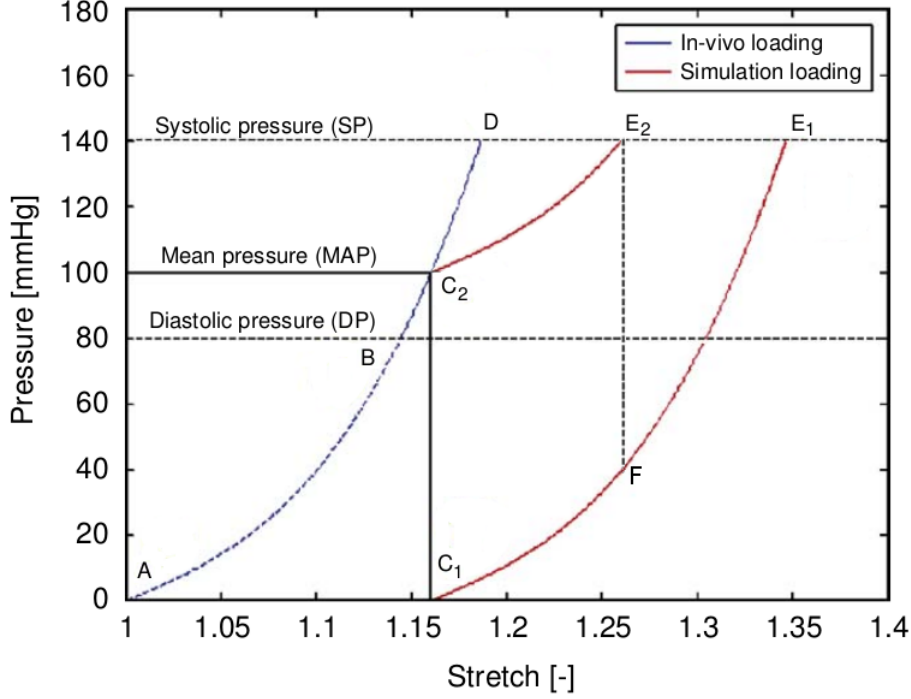


Figure 3.1: Pressure-stretch curve for an artery with nonlinear material behaviour. Modified from [75].

of the artery and it should be considered for real FSI simulations. However, from images, we start from the reconstructed geometry at C_1 . When this image-reconstructed geometry is used as reference geometry without prestress incorporation, the red curve (C_1 - E_1) is followed during loading. This leads to inaccurate FSI solutions, since we are not working in the right zone of the stress-deformation curve. Indeed, when comparing the real diastolic point (D) with E_1 , we see that a smaller systolic geometry should be obtained, with different stress distributions (D appears to be more stressed than E_1). A second common approach is to assume that reconstructed geometry is loaded with an average pressure of 70-85 mmHg (C_1 in place of C_2) and to reach systolic conditions applying a pressure increment of 35-50 mmHg (E_2). We are then translating C_1 - F curve upwards to create C_2 - E_2 curve. Also in this case we obtain erroneous results about deformation and stress state, as depicted in fig.3.1.

To achieve more realistic results, different strategies have been considered so far to model this prestress effect in arteries. We can discern two main approaches:

- a *prestress driven approach*, in which we aim at calculating the correct stress state of an image-reconstructed vessel. This means that C_2 is reached from C_1 , with just a prestress included in the Piola tensor. From C_2 , the pressure can be increased to a systolic pressure reaching the correct systolic condition (C_2 - D).
- a *zero-pressure geometry driven approach*, in which we aim at calculating the correct zero-pressure geometry starting from an image-reconstructed pressurized one. In this

case, starting from C1 geometry we calculate the geometry at A by deflation and then we apply the systolic pressure to this configuration (A-D).

3.2 State of the art

Prestress driven approaches A pure prestress driven approach is followed in [23], whereby the stress state of the reference image-based geometry is computed by an iterative procedure assuming a diastolic load of 85 mmHg and then used as starting point for the FSI analysis. In particular, they modified the variational formulation of the balance of linear momentum for the solid adding an a priori specified *prestress tensor* \mathbf{S}_0 , designed such that in the absence of displacement the blood vessel is in equilibrium with the blood flow forces

$$\mathbf{P} = \mathbf{F}(\mathbf{S} + \mathbf{S}_0). \quad (3.1)$$

This design condition leads to the following variational problem

Find the symmetric prestress tensor \mathbf{S}_0 , such that for all the test functions \mathbf{v}

$$\int_{\widehat{\Omega}} \widehat{\nabla}(\mathbf{v}) : \mathbf{S}_0 d\widehat{\Omega} - \int_{\widetilde{\Sigma}} \widetilde{\mathbf{h}} \cdot \mathbf{v} d\widetilde{\gamma} = 0, \quad (3.2)$$

where $\widehat{\Omega}$ is the blood vessel reference configuration coming from imaging data, $\widehat{\Sigma}$ is the fluid-structure interface in the same configuration, and $\widetilde{\mathbf{h}}$ is the diastolic load of 85 mmHg.

They obtain a particular solution for the state of prestress in (3.2) by means of the following procedure. Start with step $n = 1$ and set $\mathbf{S}_0^n = \mathbf{0}$, then follow these steps:

1. Set $\mathbf{S}_0 = \mathbf{S}_0^n$ and $\boldsymbol{\eta} = \mathbf{0}$, which gives $\mathbf{F} = \mathbf{I}$ and $\mathbf{S} = \mathbf{0}$;
2. From $t_n \rightarrow t_{n+1}$ solve the variational problem

Find $\boldsymbol{\eta}$ such that for all \mathbf{v}

$$\int_{\widehat{\Omega}} \widehat{\rho} \ddot{\boldsymbol{\eta}} \cdot \mathbf{v} d\widehat{\Omega} + \int_{\widehat{\Omega}} \widehat{\nabla}(\mathbf{v}) : \mathbf{F}(\mathbf{S} + \mathbf{S}_0) d\widehat{\Omega} + \int_{\widetilde{\Sigma}} \widetilde{\mathbf{h}} \cdot \mathbf{v} d\widetilde{\gamma} = 0,$$

where

$$\mathbf{S} = \mu J^{-2/3} (\mathbf{I} - \frac{1}{3} \text{tr} \mathbf{C} \mathbf{C}^{-1}) + \frac{1}{2} \kappa (J^2 - 1) \mathbf{C}^{-1}, \quad (3.3)$$

$$\mathbf{F} = \mathbf{I} + \frac{\partial \boldsymbol{\eta}}{\partial \mathbf{X}}, \quad (3.4)$$

with $\boldsymbol{\eta}$ the displacement with respect to the reference configuration $\widehat{\Omega}$ and \mathbf{X} the coordinates of the reference configuration;

3. Update $\mathbf{S}_0^{n+1} = \mathbf{S} + \mathbf{S}_0^n$ and increment n ;

4. If $\boldsymbol{\eta} \rightarrow \mathbf{0}$ we have as a result that $\mathbf{F} \rightarrow \mathbf{I}$, $\mathbf{S} \rightarrow \mathbf{0}$, and we arrive at the solution of (3.2), else continue with the next iteration.

In (3.3) μ and κ are interpreted as the blood vessel shear and bulk moduli, respectively (see [76]).

We observe that in (3.3) the value of $\mathbf{C} = \mathbf{F}^T \mathbf{F}$ used by the authors is approximated. Indeed, in (3.4) $\boldsymbol{\eta}$ is unknown and so, referring to fig.3.2 and to eq.(3.4), we have $\mathbf{F} = \mathbf{F}_A$ and not $\mathbf{F} = \mathbf{F}_{C_2}$. For this reason, in (3.3) the computed value of \mathbf{S} is not calculated in the reference geometry $\widehat{\Omega}$.

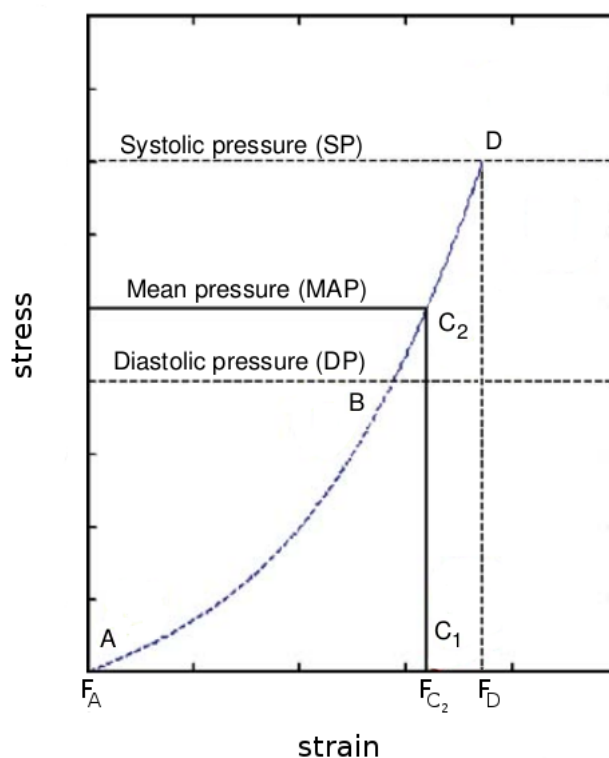


Figure 3.2: Typical stress-strain curve for an exponential material.

Another interesting method is the *modified updated Lagrangian formulation* (MULF), proposed in [24]. The MULF is algorithmically similar to the no-prestressing analysis, no buckling or bifurcation phenomena appear at least in the context of AAA simulation [24] and the resulting prestressed state is unique. However, it does not yield any deformations and so a zero-pressure geometry is not calculated.

Zero-pressure driven approaches Most of the works belonging to this strategy are based on the *Inverse design* (ID) analysis, that aims at solving the inverse elastostatic problem [77, 26, 78, 25]. Classically, the question to be answered is how a body has to be shaped in the reference configuration such that under a defined set of loads it takes on a prescribed

shape. Hence, as opposed to standard forward simulations, the spatial configuration and the set of loads are assumed to be known where the initial stress-free material configuration is to be determined. The inverse design problem basically consists on formulating the usual finite deformation balance equation and boundary conditions with respect to the known prescribed spatial configuration and the known external loads. Then, different methods could be developed that solves for the unknown coordinates of the material configuration. In the context of finite deformation this yields a system of nonlinear equations that is usually solved for incrementals applying some Newton-type scheme.

Methods for ID analysis have been originally proposed in [79] and have been analyzed in [80]. Later, other ID methods have been proposed in the context of finite deformation [81] and in the context of incompressible finite deformation [82]. An ID analysis following the approach in [81] has been employed to perform prestressing of abdominal aortic aneurysm (AAA) structures [77] and in the context of membrane modeling of cerebral aneurysms [14]. Both contributions are limited with respect to demonstrating general usability of inverse design analysis in the context of fully non-linear finite deformation analysis of predeformed structures.

As observed in [80], ID linear systems of equations are nonsymmetric and therefore ID analysis comes with an increased computational cost compared with standard forward techniques. It has been demonstrated that the obtained stress-free material configuration is not unique when inverse design analysis is applied to the full set of non-linear elasticity equations [81]. The ID method is appealing from the theory perspective but its *non-uniqueness* can be a major drawback when applied to e.g. thin walled structures that tend to exhibit bifurcation or buckling phenomena, as showed in fig.3.3.

ID analysis was later extended by other researchers to include anisotropic elastic solids via a *total* [83, 78] and an *updated* [26, 24] *Lagrange formulation*. Following an updated Lagrangian approach, in [26] the authors have introduced the *backward incremental method* (BI). This method aimed at the calculation of the initial wall stress in AAA and it is based on the backward application of computed forward deformations. If a load is applied on the initial geometry Υ_0 (zero-pressure configuration), at time t_i the wall stress depends on the current shape, the pressure P_i , the deformations to the current configuration U_i and the shear modulus G , we can write

$$\sigma_i = \sigma(t_i) = \sigma(\Upsilon_i, P_i, U_i, G),$$

where σ represents the Cauchy stress and σ_i fully describes this configuration. At every iteration i , instead of taking $\sigma(t_i) = \sigma(\Upsilon_i, P_i, U_i, G)$ as the next configuration, they take $\sigma(t_i) = \sigma(\Upsilon_r, P_i, U_i, G)$, with Υ_r as reference geometry (configuration coming from medical images, loaded with a non-zero pressure P_r). In this way they implicitly update Υ_0 by interpreting the computed forward deformations on the fixed reference domain. The principle of the backward modelling is schematically depicted in fig.3.4. During simulations they gradually increase the pressure in Υ_r in n steps to P_r , using

$$P_j = P_r \sin\left(\frac{j\pi}{2n}\right), \quad 0 \leq j \leq n,$$

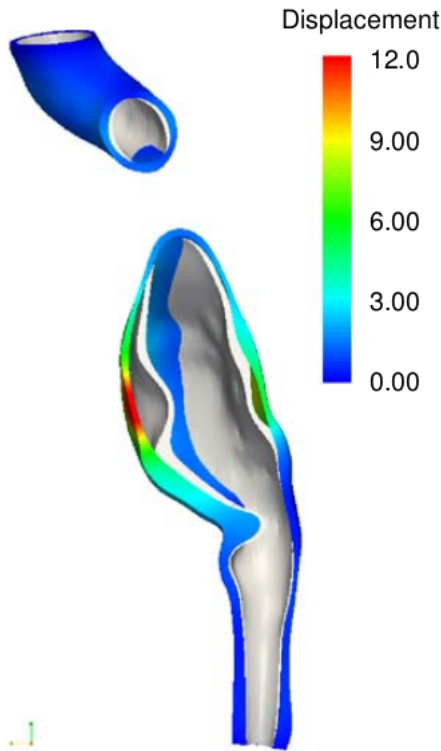


Figure 3.3: Deformation of an AAA when failure of convergence for ID appears. Gray cut indicates stress-free material configuration from ID analysis exhibiting physically meaningless buckling mode. Color indicates displacement norm in mm [24].

and the process converges to a total deformation as $n \rightarrow \infty$. At the end of the process they computed the approximation for the unloaded geometry by applying the opposite of the total deformation on Υ_r to obtain Υ_0 . Although small, some stresses were still present in the zero-pressure geometry Υ_0 . Indeed, it has been found that for all computed zero-pressure geometries the maximum stress is in the order of 10-15 kPa, representing 3-6% of the peak stresses at systolic pressure [84]. Compared to ID, the BI has two main advantages. First of all, it can be implemented starting from a model for forward elastic deformations without modifications to the underlying system being solved. This means that the convergence characteristics of the forward model are maintained. Secondly, the approach is more generic, since it can be applied using any constitutive model without modifications to the backward method itself.

In [26] the authors also proposed a possible alternative method to compute the equilibrium stress on the diastolic geometry. They first assumed a very high shear modulus and then compute the stress in the whole domain by performing a forward simulation with the reference diastolic pressure, $\hat{\sigma}$, as boundary condition. This is done by assuming that the geometry is similar to the reference one, and this is realistic due to the high stiffness. They performed simulations for the uniaxial deformation of a cube and the inflation of a cylinder and the

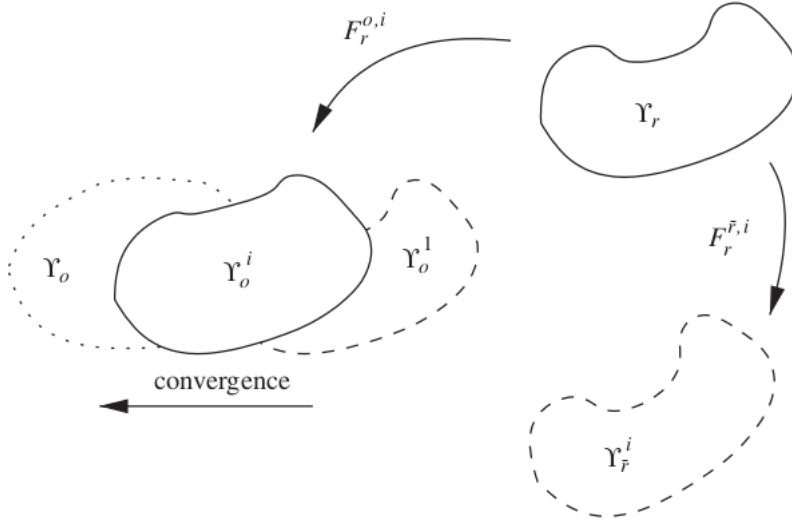


Figure 3.4: Backward incremental modelling approach: Υ_r reference geometry reconstructed from medical image and loaded with a pressure P_r , Υ_o initial geometry assumed to be unloaded, $\Upsilon_{\bar{r}}^i$ forward domain that can be computed by applying deformations on the reference domain at i th iteration and related deformation $F_r^{\bar{r},i}$, Υ_o^i i th approximation of Υ_o , $F_r^{o,i}$ deformation from Υ_r to Υ_o^i [26].

resulting stress fields were found to be similar to the stress computed with the backward incremental method, but convergence was generally very poor. Because of the additional disadvantage that this method does not directly provide a deformation field to Υ_o , and therefore also does not provide a simple approximation of the wall strain, they did not pursue this approach any further.

A further different strategy is suggested in [49].

3.3 Description of the strategy used in this work

The approach we followed is a zero-pressure geometry driven one. The goal is to recover a deflated geometry starting from an inflated one. At first, we obtain the patient-specific carotid geometry from MRI or CT scans by using the computer-assisted fast marching level set method implemented in the open-source Vascular Modeling ToolKit (VMTK) [85]. Indeed, from the geometrical reconstruction of radiological images, one obtains a diastolic intramural pressure geometry. The problem is that by performing numerical simulations in this computational domain we do not take into account for the prestressed state in vessel walls. Then, if we impose a pressure waveform in the reconstructed geometry which is given by the real one minus the diastolic one, we are not working at the right zone of the stress-deformation curve, leading to approximated FSI simulation results.

We simulated this prestress effect calculating a 0 mmHg intramural pressure geometry starting from the reconstructed one, using a fixed point method to solve the inverse problem.

By applying the whole pressure waveform to this deflated configuration it is then possible to recover more realistic results in FSI simulations (A-D in fig.3.1). Therefore, we have to solve the following inverse problem:

Given the MRI diastolic reconstructed geometry $\widehat{\Omega}$, find the zero-pressure geometry Ω_0 such that

$$S(\Omega_0, P_d) = \widehat{\Omega},$$

where S is the structural operator which, given a domain Ω_0 and an internal load P_d , gives the domain $\widehat{\Omega}$ obtained by moving the coordinates accordingly to the computed displacement. To solve such inverse problem, we propose here the following algorithm:

Algorithm.

Given an initial loaded geometry $\widehat{\Omega}$ and a suitable tolerance ε , do until convergence at iteration k

1. Solve the structural problem (2.15) on $\widehat{\Omega}$ with an internal load P_d , obtaining a set of displacements $\widetilde{\boldsymbol{\eta}}^{(k)}$;

2. Deflate $\widehat{\Omega}$ to find $\Omega_0^{(k)}$

$$\Omega_0^{(k)} = \widehat{\Omega}^{(k)} - \widetilde{\boldsymbol{\eta}}^{(k)}; \quad (3.5)$$

3. Solve the structural problem (2.15) on $\Omega_0^{(k)}$ with the same load used in step 1, obtaining a set of displacements $\widetilde{\boldsymbol{\lambda}}^{(k+1)}$;

4. Inflate $\Omega_0^{(k)}$ to find $\widehat{\Omega}^{(k+1)}$

$$\widehat{\Omega}^{(k+1)} = \Omega_0^{(k)} + \widetilde{\boldsymbol{\lambda}}^{(k+1)}; \quad (3.6)$$

5. Calculate the residual $\boldsymbol{\chi}^{(k+1)} = \widehat{\Omega}^{(k+1)} - \widehat{\Omega}$ and verify the stopping criterion

$$\frac{\|\boldsymbol{\chi}^{(k+1)}\|_\infty}{\|\widehat{\Omega}\|_\infty} \leq \varepsilon; \quad (3.7)$$

6. If the residual does not satisfy the stopping criterion then update the set of displacements $\widetilde{\boldsymbol{\eta}}^{(k)}$ using a relaxation parameter α

$$\widetilde{\boldsymbol{\eta}}^{(k+1)} = \widetilde{\boldsymbol{\eta}}^{(k)} + \alpha \boldsymbol{\chi}^{(k+1)}, \quad (3.8)$$

and return to step 2, else the solution $\Omega_0^{(k)} + \widetilde{\boldsymbol{\lambda}}^{(k+1)} \approx \widehat{\Omega}$ has been found.

The infinity norm in (3.7), for the case of a vector $\mathbf{x} = (x_1, \dots, x_n)$ in finite dimensional

coordinate space, takes the form

$$\|x\|_\infty = \max \{|x_1|, \dots, |x_n|\}.$$

When we consider image-reconstructed human geometries, the internal load P_d used in step 1 and 3 represent the average intramural pressure of 80 mmHg coming from radiological images. In case, this choice could be more patient-specific if this average pressure is directly measured on the patient. With regard to this pressure load, we can see step 1 and 3 as *inflation* steps in which a particular geometry is inflated with this level of pressure, and step 2 as a *deflation* step where we deflate a geometry with a set of displacements computed at the first inflation step.

Our approach is similar to the one followed in [67]. In that work the authors dealt with FSI simulation of an ascending aorta. The blood flow domain is initialized by calculating the steady solution of a rigid wall Navier-Stokes flow with a prescribed input flow corresponding to the average cardiac output, i.e. the stroke volume multiplied by the heart rate. In order to compute the mapping from the unknown reference configuration Ω_0 onto the loaded configuration $\hat{\Omega}$, they used the residual $\mathcal{P}_{\hat{\Sigma}}^f$, which represents the fluid stress tensor at the interface $\hat{\Sigma}$, obtained from the rigid wall fluid solution. Then they solved the inverse problem using a simple fixed point algorithm.

The use of the residual $\mathcal{P}_{\hat{\Sigma}}^f$ does not result in a better patient-specific initial condition because they take into account the tangential fluid stress tensor component not even present in a diastolic radiological image since the blood is at rest. This is the reason we preferred a simple average cardiac cycle pressure (or the average patient-specific one, if available) in our algorithm.

3.4 Numerical results

In this section we present the numerical results on simple geometries, i.e. a cube and an hollow cylinder. In all the numerical simulations, we consider the compressible *St. Venant-Kirchhoff* material and the nearly incompressible *Exponential* material. The first Piola-Kirchhoff tensor for the St. Venant-Kirchhoff material is defined in (2.42), here reported:

$$\mathbf{P} = \frac{\lambda}{2}(I_1(\mathbf{C}) - 3)\mathbf{F} - \mu\mathbf{F} + \mu\mathbf{F}\mathbf{C}$$

For the Exponential material it is defined in (2.45), here reported:

$$\mathbf{P} = \alpha J^{-2/3} \left(\mathbf{F} - \frac{1}{3} I_1(\mathbf{C}) \mathbf{F}^{-T} \right) e^{\gamma(I_1(\bar{\mathbf{C}}-3))} + J \frac{\kappa}{2} \left(J - 1 + \frac{1}{J} \ln J \right) \mathbf{F}^{-T}.$$

The finite element discretization is performed by P1 elements and the mesh properties are showed in table 3.1 and 3.3. The set of structural parameters are listed in table 3.2 and are typical values for biological tissues [13, 28, 38, 39].

3.4.1 Cube

We consider the case of homogeneous pure strain of a cube. The test consists in the normal traction of a cube in the direction of the Cartesian axis x , with homogeneous Dirichlet condition in the same direction but on the opposite face, see fig.3.5. The problem reads:

$$\begin{cases} \widehat{\nabla} \cdot \mathbf{P} + \widehat{\rho} \mathbf{b} = 0, & \text{in } [0, L]^3, \\ \boldsymbol{\eta}(x=0) \cdot \mathbf{e}_x = 0, \\ \boldsymbol{\eta}(x=L) \cdot \mathbf{e}_x = \bar{p}, \end{cases} \quad (3.9)$$

where \mathbf{e}_x is the unit vector in the x direction and \bar{p} is a prescribed pressure.

To correctly reproduce the steady state elastostatic response in (3.9), we have performed unsteady simulations and we have waited the end of the transitory of the elastodynamic system. For this purpose, we used as time discretization parameter $\Delta t = 0.001$ s, with a final time $T = 0.005$ s.

Table 3.1: Cube mesh properties.

Nodes	Tetrahedra	Length
125	384	1 cm

Table 3.2: Set of structural parameters for the cube and the cylinder.

$\rho[g/cm^3]$	$E[dyne/cm^2]$	ν	$\kappa[dyne/cm^2]$	$\alpha[dyne/cm^2]$	γ
1.2	6.0e6	0.45	1.0e8	2.0e6	0.8

Varying the load. We performed different simulations varying the value of the load \bar{p} . In fig.3.6 we observe the variation of the residual χ respect to the load and in fig.3.7 the number of iterations to reach convergence for each load. During simulations we assumed $\varepsilon = 10^{-4}$ and different values of the relaxation parameter α to verify the stopping criterion (3.7) (see fig.3.8). We remark that the values of the relaxation parameter α are not optimal. Therefore, the number of iterations to reach convergence can be decreased further.

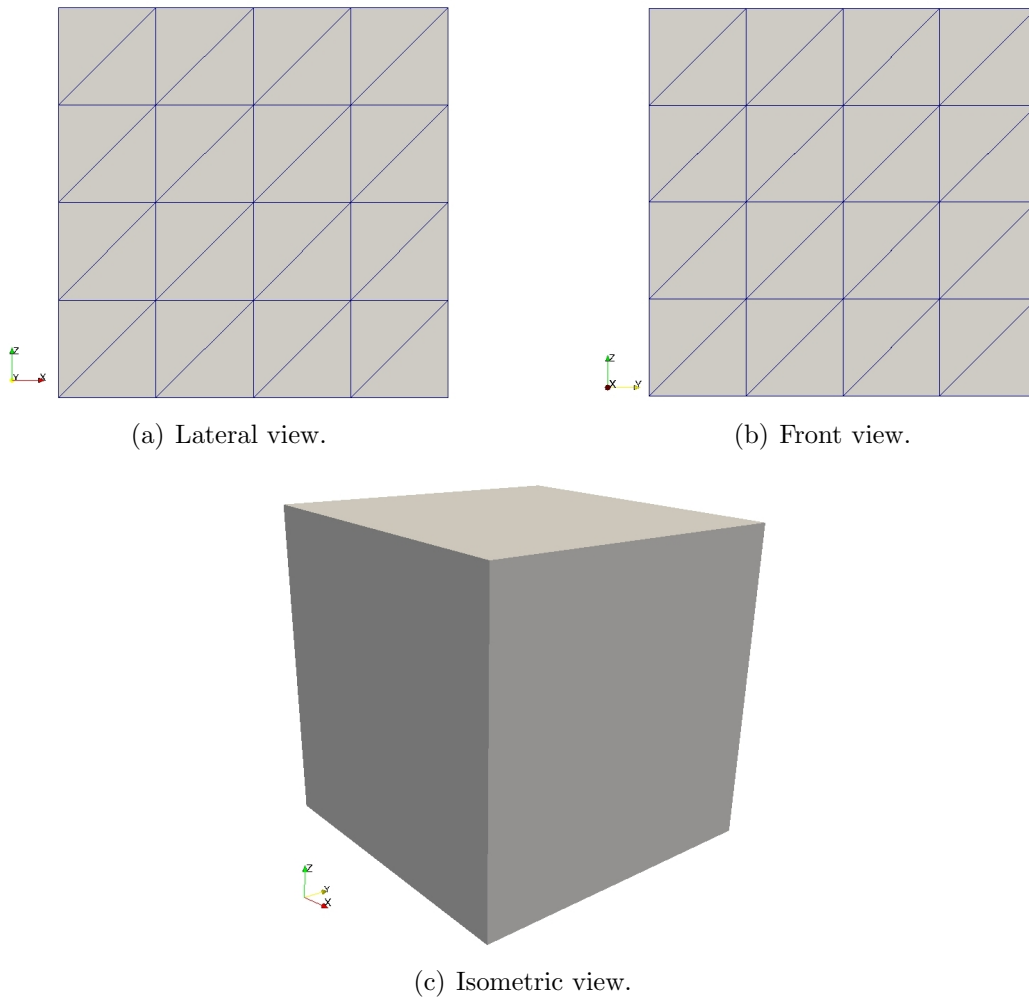


Figure 3.5: The cube.

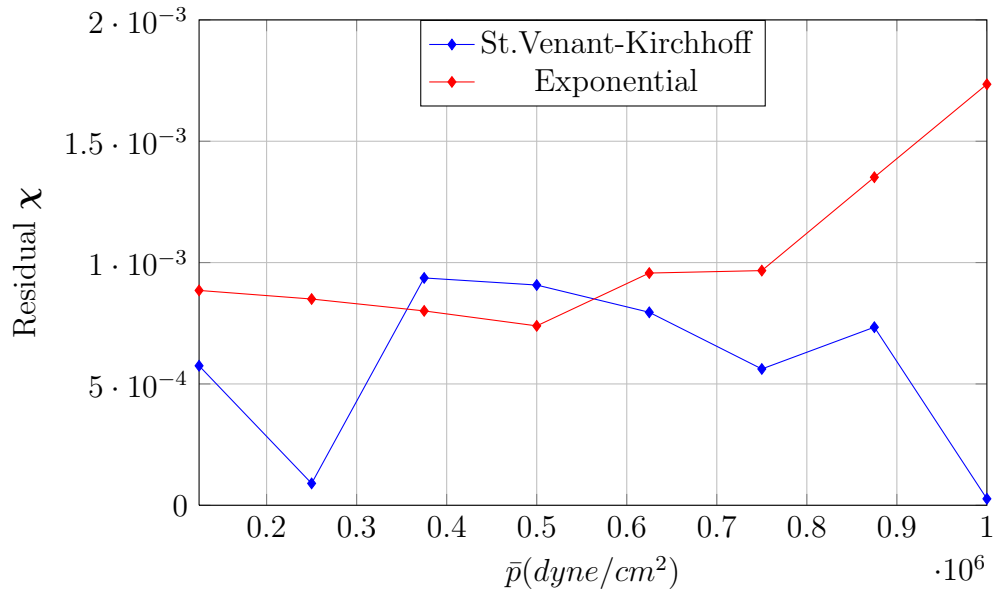


Figure 3.6: Cube, residual χ vs. load \bar{p} .

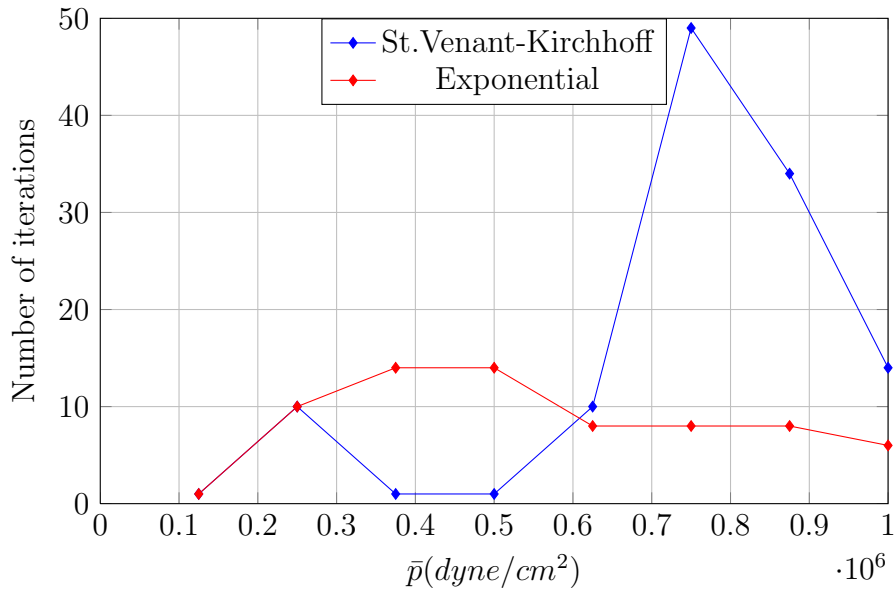


Figure 3.7: Cube, number of iterations vs. load \bar{p} .

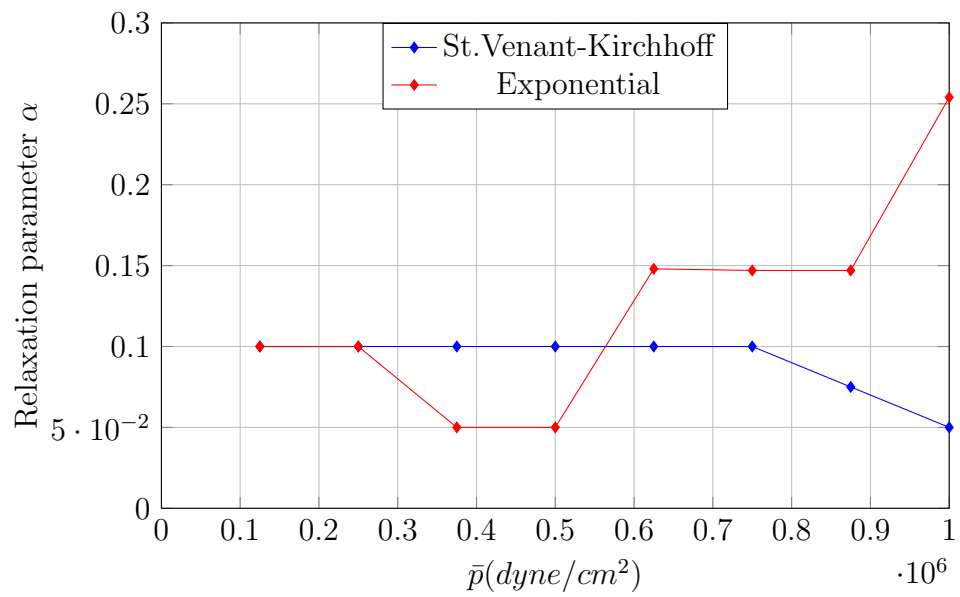


Figure 3.8: Cube, values of the relaxation parameter α vs. load \bar{p} .

In figures 3.9,3.10, for the load case $\bar{p} = 0.625 \cdot 10^6 \text{ dyne/cm}^2$, we observe the comparison between the reference geometry $\widehat{\Omega}$ (in grey) and the deflated geometry Ω_0 (in blue) calculated in (3.5) at the end of the algorithm.

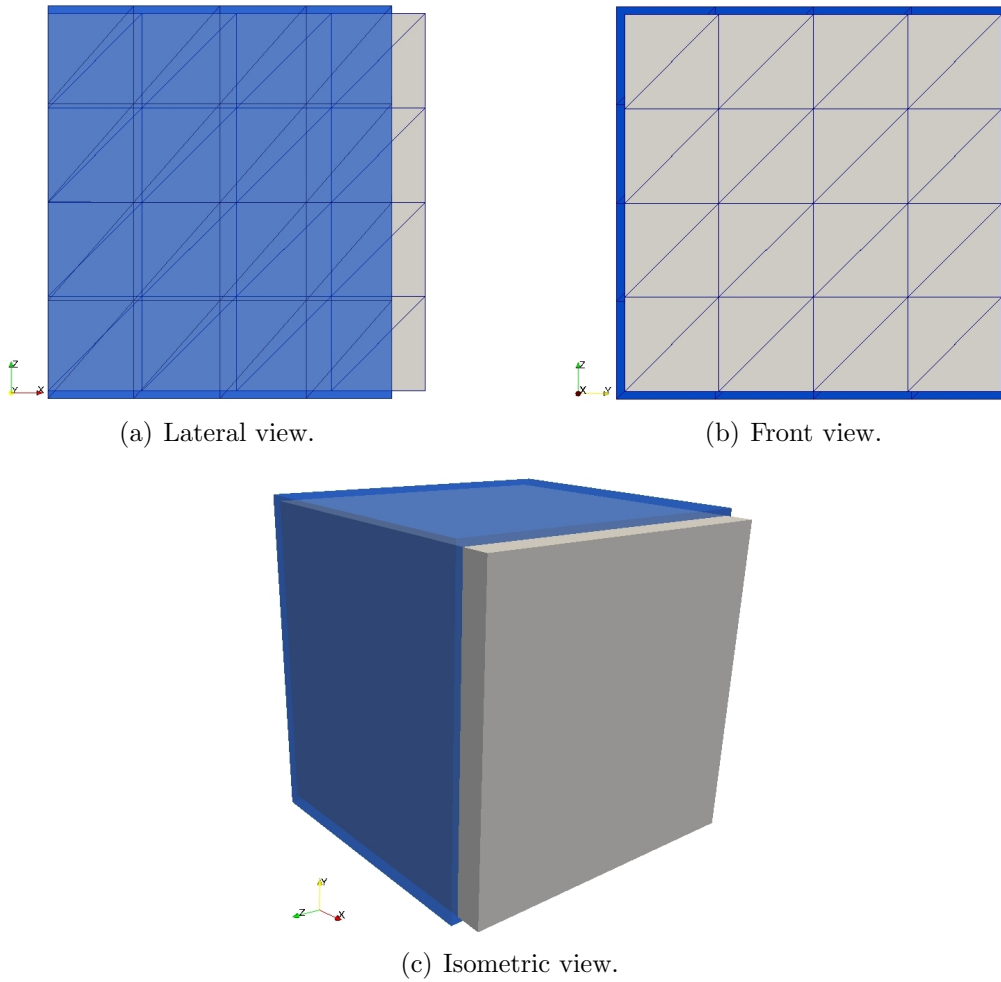


Figure 3.9: St.Venant-Kirchhoff material cube, comparison between the reference geometry $\widehat{\Omega}$ (in grey) and the deflated geometry Ω_0 (in blue), for the load case $\bar{p} = 0.625 \cdot 10^6 \text{ dyne/cm}^2$. The deflated cube shows a shortening of 0.0887 cm in the x direction and an elongation of 0.0212 cm in the y and z directions.

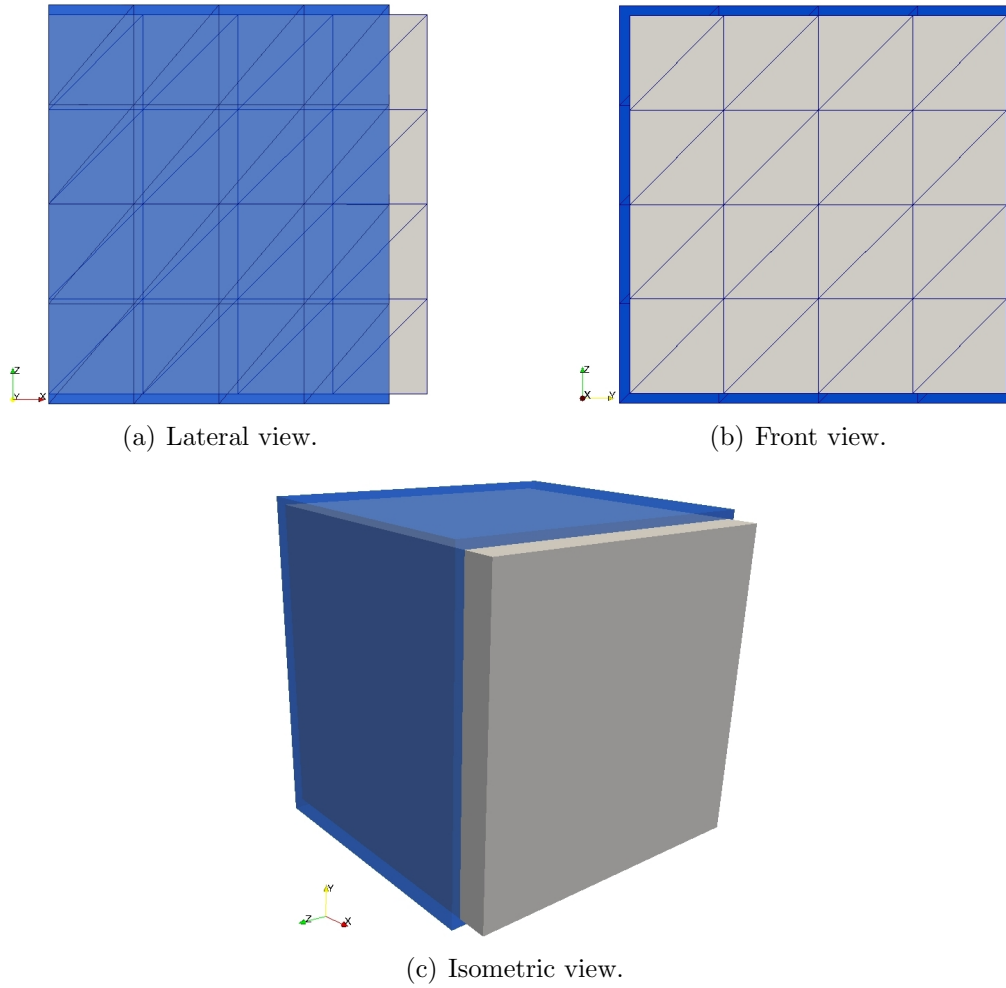


Figure 3.10: Exponential material cube, comparison between the reference geometry $\widehat{\Omega}$ (in grey) and the deflated geometry Ω_0 (in blue), for the load case $\bar{p} = 0.625 \cdot 10^6 \text{ dyne/cm}^2$. The deflated cube shows a shortening of 0.1012 cm in the x direction and an elongation of 0.0266 cm in the y and z directions.

Consistency test. As a consistency test, we can apply the load P_d , used in the algorithm at steps 1 and 3, on the final deflated geometry Ω_0 to obtain the reference geometry $\widehat{\Omega}$. In figures 3.11 and 3.12 we observe a very good overlapping between this two geometries for both St.Venant-Kirchhoff and Exponential material cases.

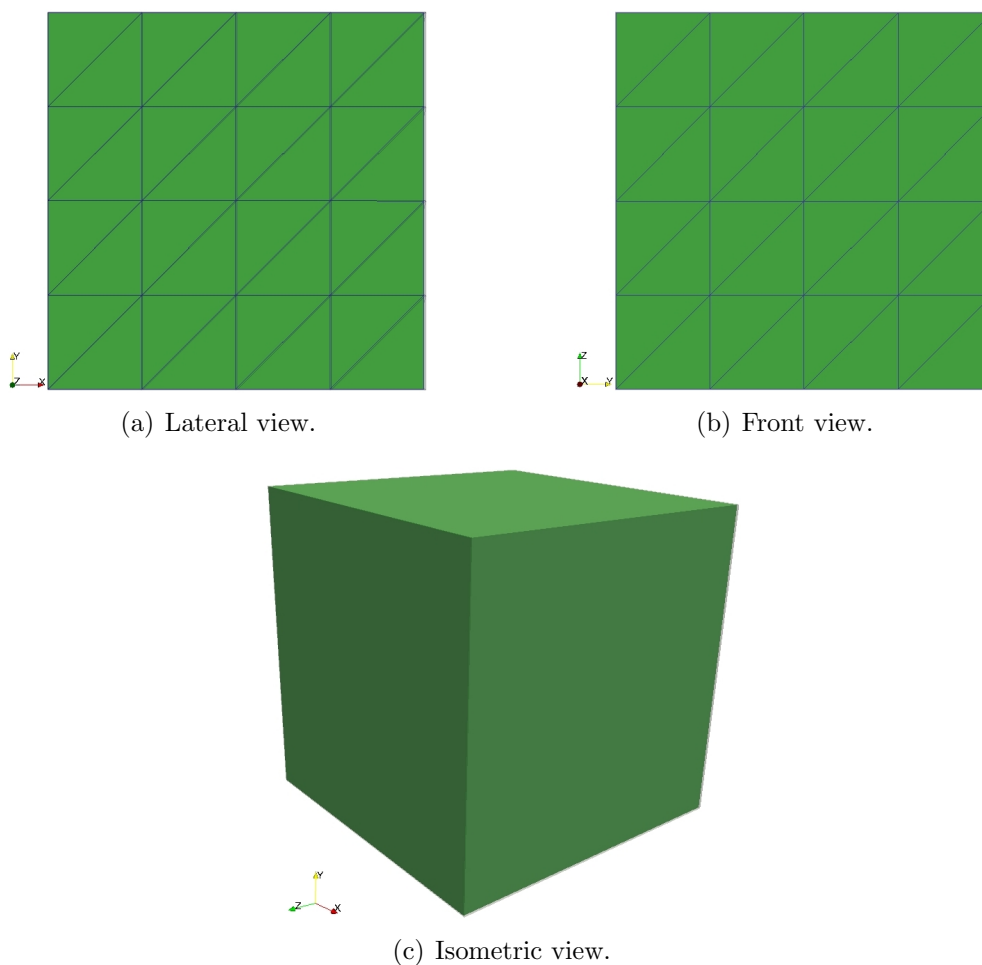


Figure 3.11: St.Venant-Kirchhoff material cube, comparison between the reference geometry $\widehat{\Omega}$ (in grey) and the deflated geometry Ω_0 (in green) re-inflated with the load $\bar{p} = 0.625 \cdot 10^6 \text{ dyne/cm}^2$. After re-inflation, the deflated cube length is 0.0055 cm shorter than the reference geometry one.

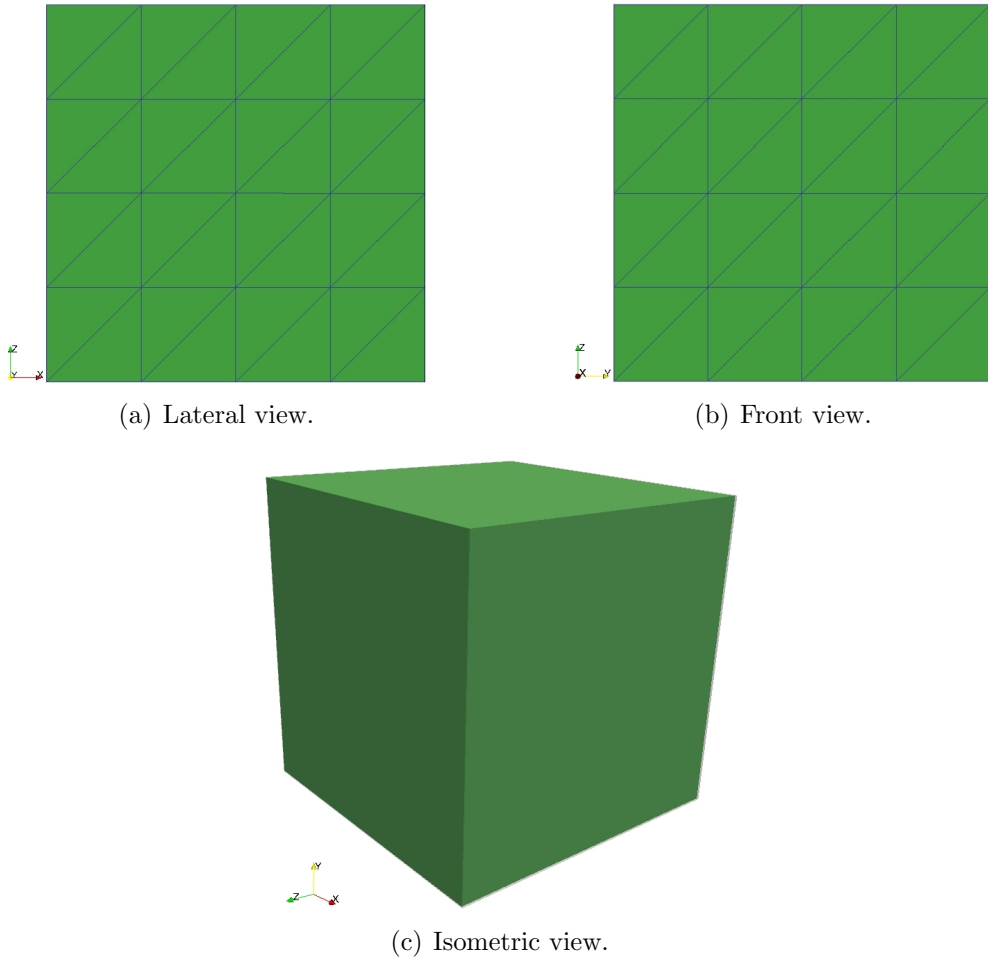


Figure 3.12: Exponential material cube, comparison between the reference geometry $\hat{\Omega}$ (in grey) and the deflated geometry Ω_0 (in green) reinflated with the load $\bar{p} = 0.625 \cdot 10^6 \text{ dyne/cm}^2$. After reflation, the deflated cube length is 0.00046 cm longer than the reference geometry one.

3.4.2 Cylinder

We consider here the inflation of a hollow cylinder, the simplest model to simulate a vessel. The test consists in the application of the average intramural pressure $P_d = 80 \text{ mmHg} = 106640 \text{ dyne/cm}^2$ coming from radiological images, with Dirichlet boundary conditions on the basis, in the direction of the cylinder axis, and Robin boundary conditions on the external surface in the radial direction, see fig.3.13. In particular, Robin boundary condition coefficient β simulates the elastic behaviour of the tissues which surround the vessel in the human body [67]. The problem reads:

$$\left\{ \begin{array}{l} \widehat{\nabla} \cdot \mathbf{P} = 0, \\ \mathbf{P}(R_{in}) \mathbf{e}_R = P_d \mathbf{e}_R, \\ \mathbf{P}(R_{out}) \mathbf{e}_R + \beta \boldsymbol{\eta}(R_{out}) \cdot \mathbf{e}_R = P_{ext} \mathbf{e}_R, \\ \boldsymbol{\eta}(z = -L/2) \cdot \mathbf{e}_z = 0, \\ \boldsymbol{\eta}(z = L/2) \cdot \mathbf{e}_z = 0, \end{array} \right. \quad (3.10)$$

where \mathbf{e}_R and \mathbf{e}_z are the unit vectors associated to the radial and axial directions, R_{in} and R_{out} are the inner and outer radii of the cylinder.

To correctly reproduce the steady state elastostatic response in (3.10), we have performed unsteady simulations and we have waited the end of the transitory of the elastodynamic system. For this purpose, we used as time discretization parameter $\Delta t = 0.001 \text{ s}$, with a final time $T = 0.005 \text{ s}$.

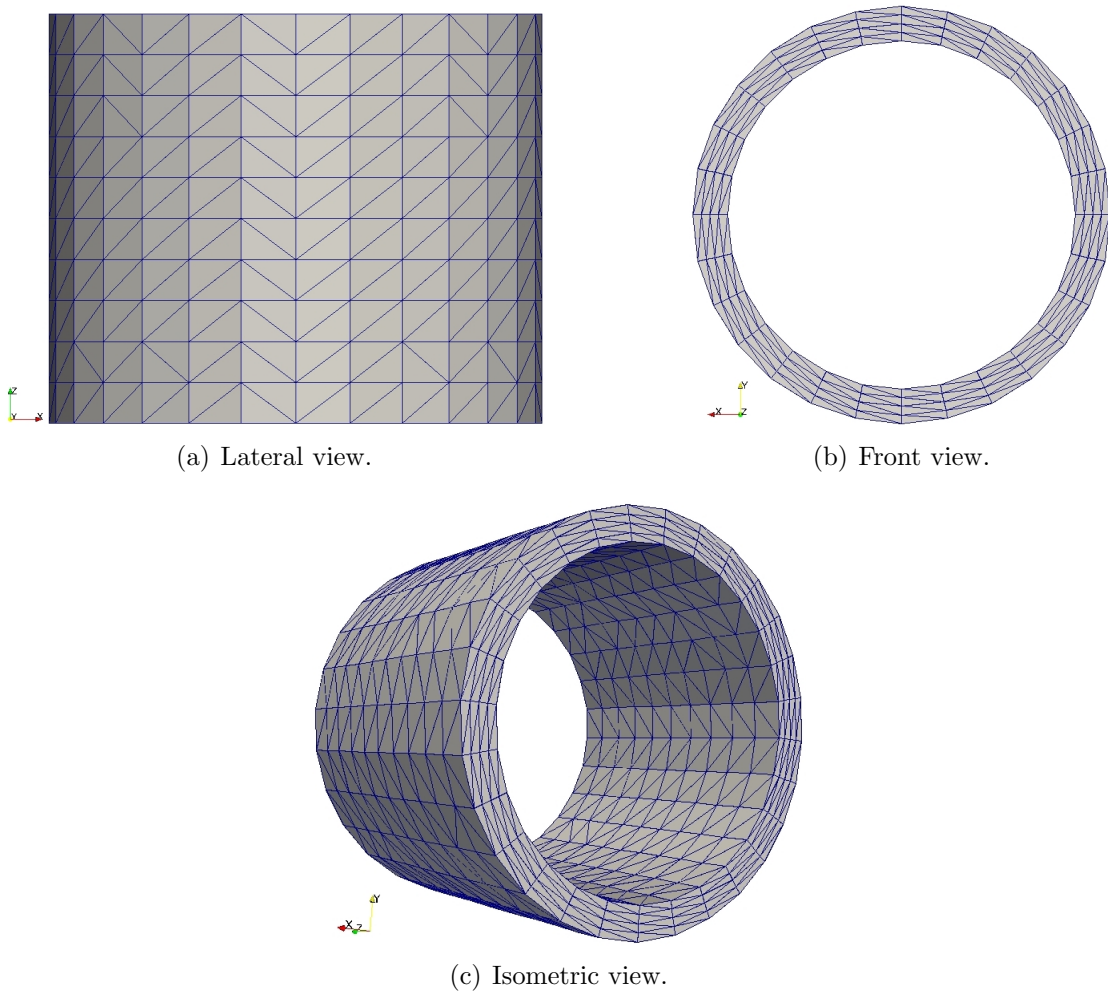


Figure 3.13: The cylinder.

Table 3.3: Cylinder mesh properties.

Nodes	Triangles	Tetrahedra	Length	Inner radius	Outer radius
1540	1568	6720	1 cm	0.5 cm	0.6 cm

Harmonic extension problem Given $\widehat{\Omega}_f$ and $\mathbf{h}(t)$, find $\widehat{\boldsymbol{\eta}}_m(t) : \widehat{\Omega}_f \rightarrow \Omega_f$ for any $t \in [t_0, T]$ such that

$$\begin{cases} -\Delta \widehat{\boldsymbol{\eta}}_m(t) = 0 & \text{in } \widehat{\Omega}_f, \\ \widehat{\boldsymbol{\eta}}_m(t) = \mathbf{h}(t) & \text{on } \partial \widehat{\Omega}_f. \end{cases} \quad (3.11)$$

$$\mathbf{u}_m = \frac{\partial \widehat{\boldsymbol{\eta}}_m}{\partial t}.$$

Varying the surrounding tissue coefficient. We performed different simulations varying the value of the Robin boundary condition coefficient β . In fig.3.14 we observe the variation of the final residual $\boldsymbol{\chi}$ respect to the Robin boundary condition coefficient β and in fig.3.15 the number of iterations to reach convergence for each β . The values of β are chosen in the range of experimental results reported in [86]. During simulations we assumed $\varepsilon = 10^{-4}$ and different values of the relaxation parameter *alpha* to verify the stopping criterion (3.7) (see fig.3.16). In particular, from figures 3.15 and 3.16 we observe that the number of iterations and the values of α to reach convergence are the same for both materials. We want to remark that the values of the relaxation parameter α are not optimal. Therefore, the number of iterations to reach convergence can be decreased further.

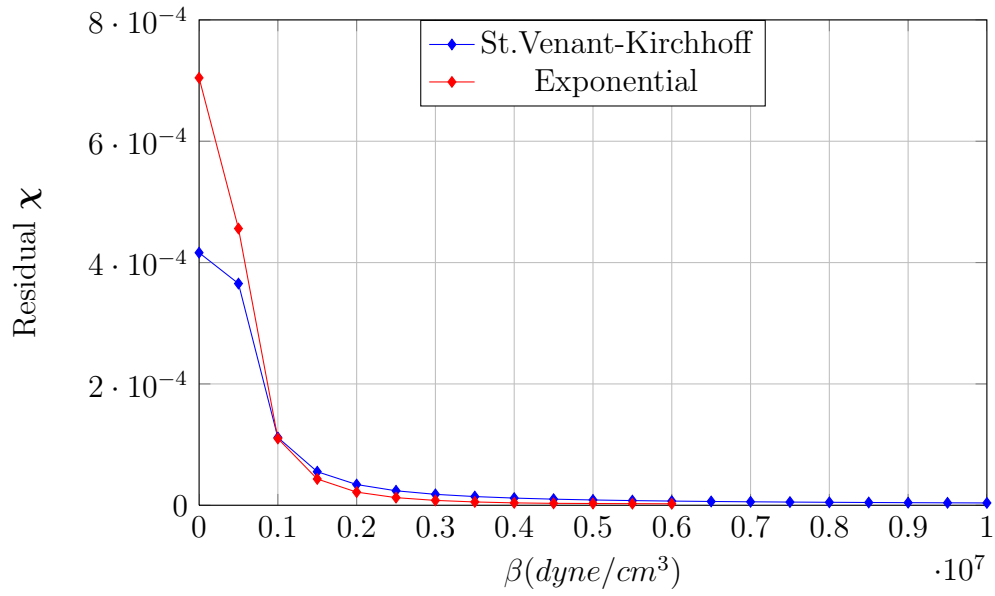


Figure 3.14: Cylinder, residual χ vs. load \bar{p} .

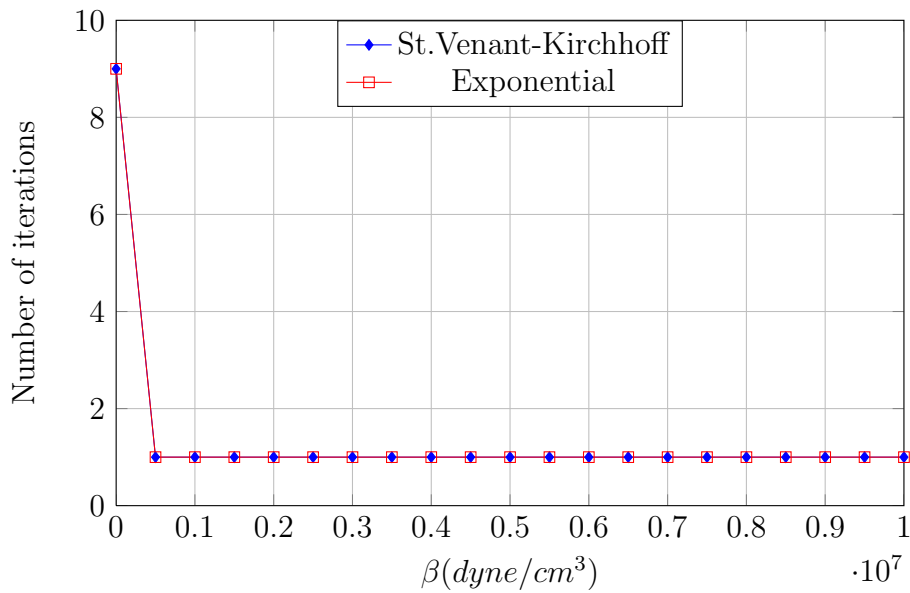


Figure 3.15: Cylinder, number of iterations vs. coefficient β .

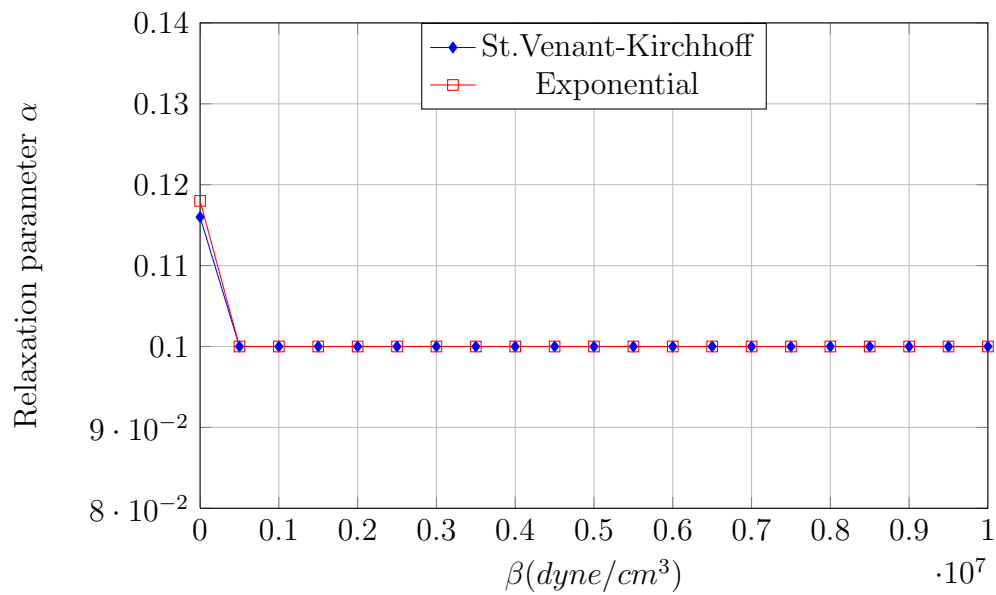


Figure 3.16: Cylinder, values of the relaxation parameter α vs. coefficient β .

3.4. Numerical results

In figures 3.17 and 3.18, for the Robin boundary condition coefficient $\beta = 0$, we observe the comparison between the reference geometry $\widehat{\Omega}$ (in grey) and the deflated geometry Ω_0 (in blue) calculated in (3.5) at the end of the process.

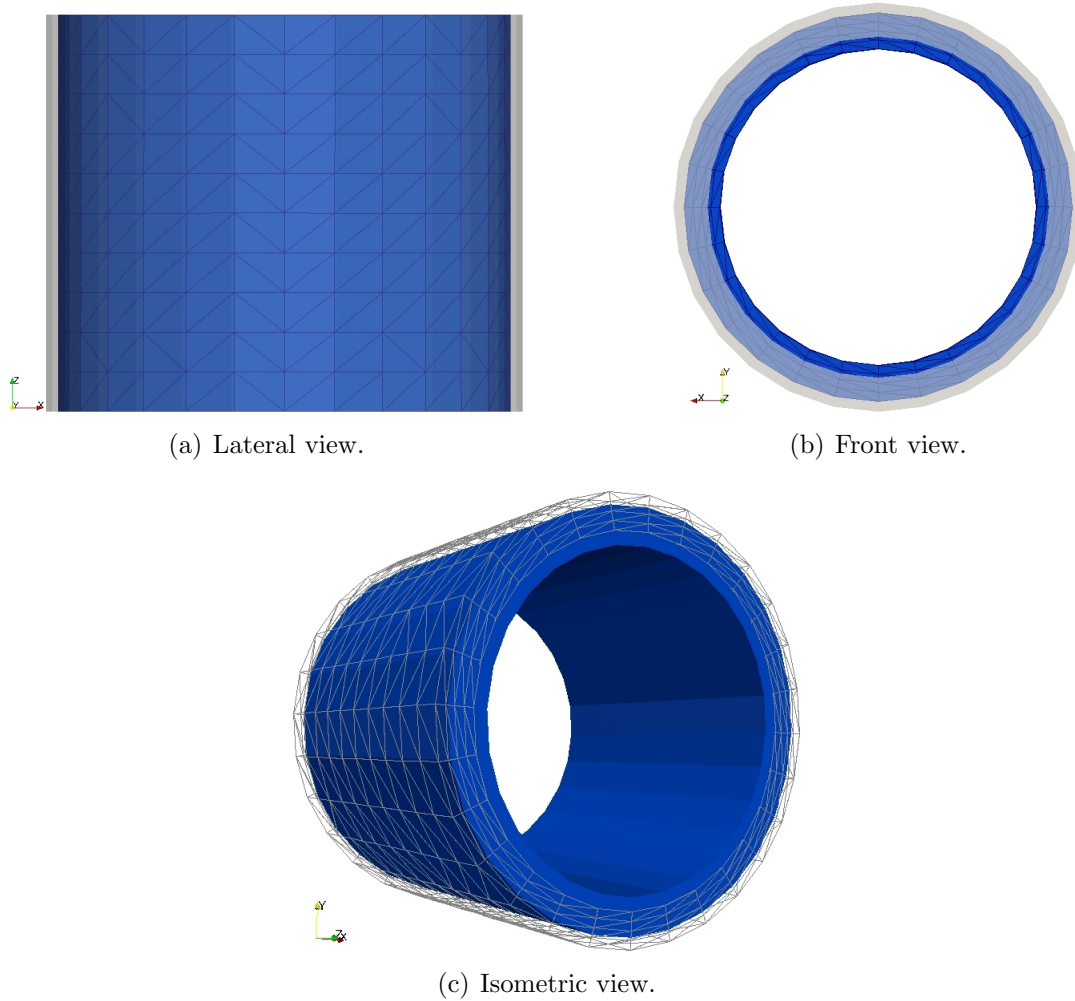


Figure 3.17: St.Venant-Kirchhoff material cylinder: comparison between the reference geometry $\widehat{\Omega}$ (in grey) and the deflated geometry Ω_0 (in blue), for the Robin boundary condition coefficient $\beta = 0 \text{ dyne/cm}^3$. The deflated cylinder shows a reduction of the inner and the outer radii of 0.0358 cm and 0.0304 cm respectively, and its thickness increases of 0.005 cm.

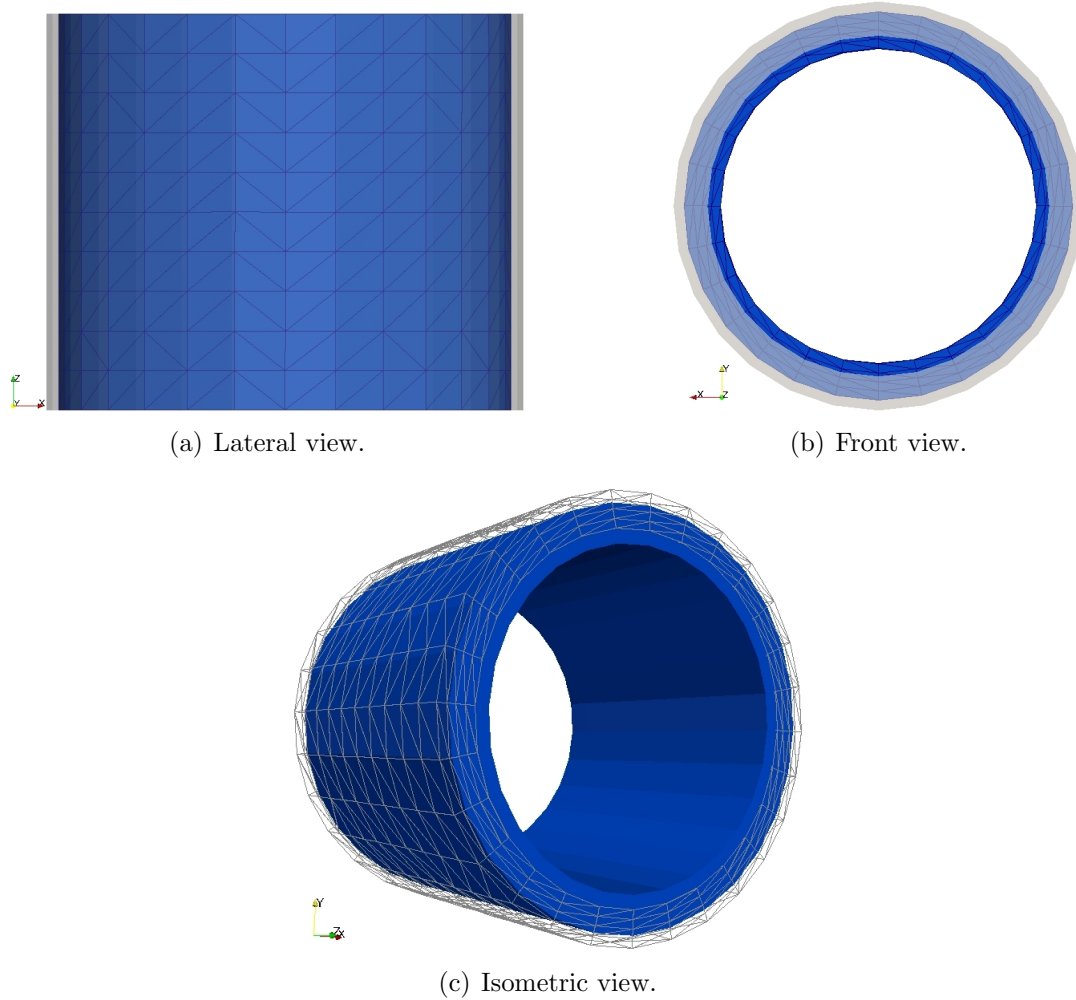


Figure 3.18: Exponential material cylinder: comparison between the reference geometry $\hat{\Omega}$ (in grey) and the deflated geometry Ω_0 (in blue), for the Robin boundary condition coefficient $\beta = 0 \text{ dyne/cm}^3$. The deflated cylinder shows a reduction of the inner and the outer radii of 0.0372 cm and 0.0308 cm respectively, and its thickness increases of 0.006 cm.

Consistency test. As a consistency test, we can apply the load P_d , used in the algorithm at steps 1 and 3, on the final deflated geometry Ω_0 to obtain the reference geometry $\hat{\Omega}$. In figures 3.19 and 3.20 we observe a very good overlapping between this two geometries for both St.Venant-Kirchhoff and Exponential material cases.

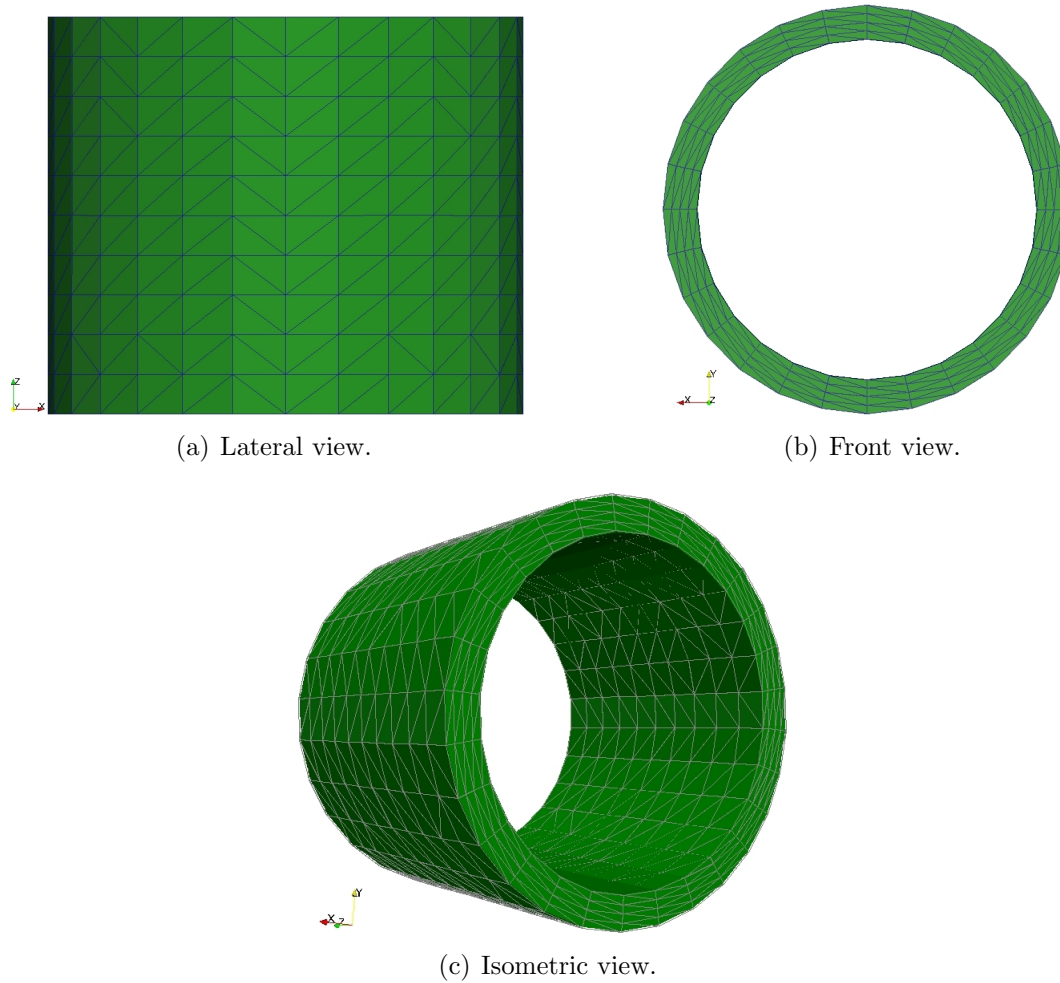


Figure 3.19: St.Venant-Kirchhoff material cylinder: comparison between the reference geometry $\hat{\Omega}$ (in grey) and the deflated geometry Ω_0 (in green) reinflated with the load $P_d = 80 \text{ mmHg} = 106640 \text{ dyne/cm}^2$. After reflation, the deflated geometry inner and outer radii are, respectively, 0.0017 cm and 0.0020 cm shorter than the reference geometry ones.

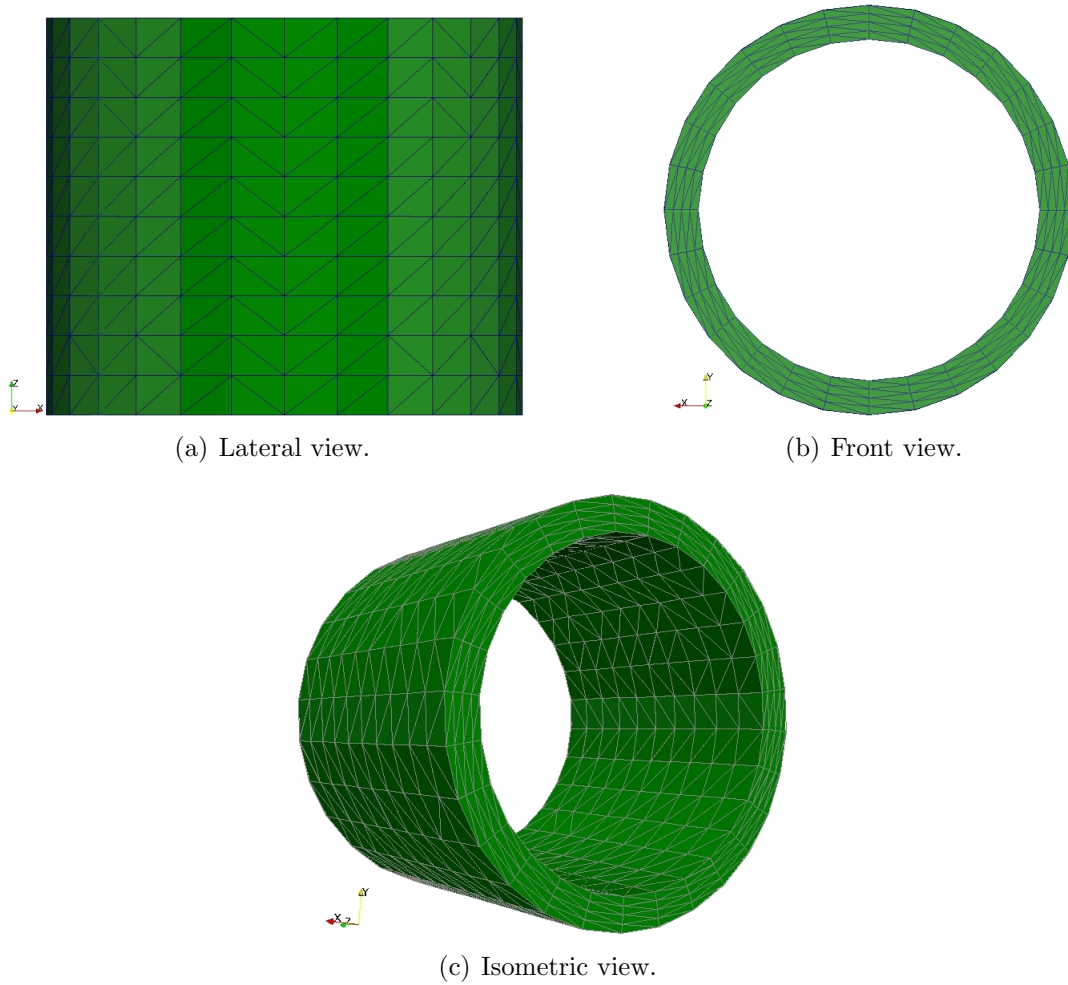


Figure 3.20: Exponential material cylinder: comparison between the reference geometry $\hat{\Omega}$ (in grey) and the deflated geometry Ω_0 (in green) reinflated with the load $P_d = 80 \text{ mmHg} = 106640 \text{ dyne/cm}^2$. After reflation, the deflated geometry inner and outer radii are, respectively, 0.00058 cm and 0.00052 cm longer than the reference geometry ones.

Chapter 4

Incompressible Navier-Stokes equations in moving domain

In the first part of this chapter we introduce the Arbitrary Lagrangian Eulerian (ALE) formulation for moving domains and the fluid and fluid domain problems. In the second part we delineate the weak formulation, finite element and time discretization of such problems.

4.1 The blood modeling

To correctly describe the fluid-structure interaction (FSI) problem, in addition to the structural problem equations described in chapter 2, we must describe the equations governing the fluid problem. The blood is a complex suspension of cells in plasma, with the concentration of cells $\approx 50\%$ by volume and the plasma consisting of $\approx 90\%$ water, 8% proteins, 1% inorganic substances, and 1% emulsified fat. There are three major types of cells in blood: erythrocytes (or red blood cells), leukocytes (or white blood cells), and platelets, as depicted in fig.4.1. Erythrocytes are the most abundant cells in blood; they transport oxygen and carbon dioxide. Mammalian erythrocytes are disk shaped (due to the absence of a nucleus) with a diameter of approximately $8 \mu m$ and a thickness of $2 \mu m$. Leukocytes represent less than 1% of blood cells, but they have a critical role in producing antibodies and identifying and disposing of foreign substances. Monocytes and lymphocytes are two particular types of leukocytes that have been implicated in early stages of atherosclerosis, consistent with the view that chronic inflammation is important [87]. Platelets control the conversion of the plasma-borne protein fibrinogen to fibrin, a key structural element in a blood clot. Activation, aggregation, and accumulation of platelets depends on local hemodynamic loads and are critical in both the normal processes of vessel healing/hemostasis and the abnormal events that cause thrombosis.

Although the plasma consists primarily of water, the large concentration of cells in blood results in a *non-Newtonian* rheological behavior. Specifically, blood exhibits a shear-thinning behavior, with a higher overall viscosity at any shear rate in the presence of increased cell concentration. Non-Newtonian models, are often used in computational modeling of blood

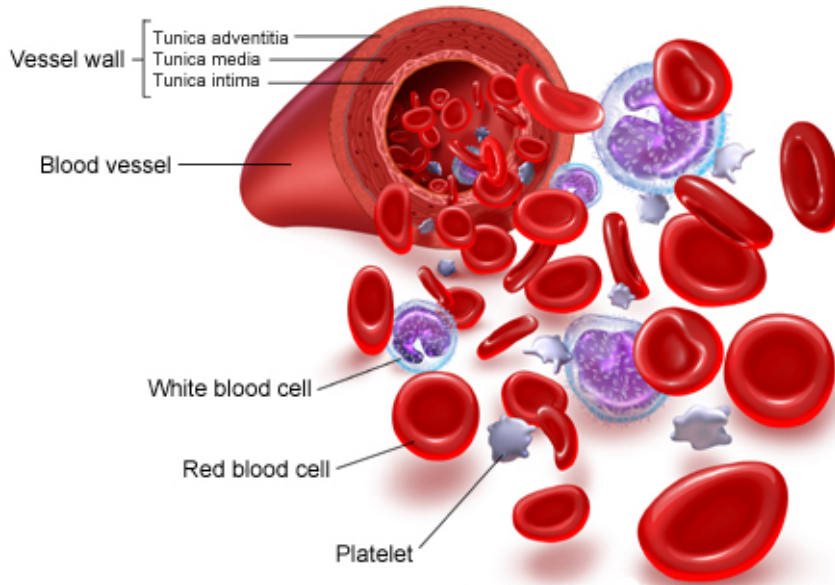


Figure 4.1: The three major types of cells in blood.

flow [88]. Nevertheless, it is generally assumed that blood flow in large arteries, where the shear rate is high, can be modeled reasonably well using a *Newtonian fluid approximation*. This hypothesis is commonly accepted in literature for flow in main blood vessels (e.g. [89, 90, 20, 91, 92, 93]) though it may be inaccurate in the small ones, or when the shear stress in the fluid is below a critical threshold (e.g. in the venous system). However, in this work we focus on the carotid artery, where the assumption of incompressible Newtonian fluid is acceptable.

4.2 The fluid and the fluid domain problem

The first difficulty we have to face is the computation of the unknown moving fluid domain. The idea is to use a moving mesh that follows the deformation of the physical border, i.e. the fluid-structure (FS) interface Σ , and that is kept fixed on the artificial sections $\Sigma_f^{in}, \Sigma_f^{out}$ (see fig.4.2).

We assume that the physical border displacement \mathbf{h} is given. The fluid domain displacement at the physical border must be equal to \mathbf{h} , at the artificial one we decide to keep it fixed. Considering the motion of fluid and fluid domain particles, on the physical border, where the fluid domain particles have the same motion as the fluid, we adopt a Lagrangian Navier-Stokes equations formulation. On the contrary, at the artificial sections, where the fluid domain particles are fixed while the fluid ones follow their own independent motion, we use an Eulerian Navier-Stokes equations formulation. Inside the fluid domain we consider a hybrid behaviour. Indeed, near the physical border, the fluid domain velocity is similar to the fluid one, becoming identical at Σ ; approaching to the artificial border, instead, the fluid

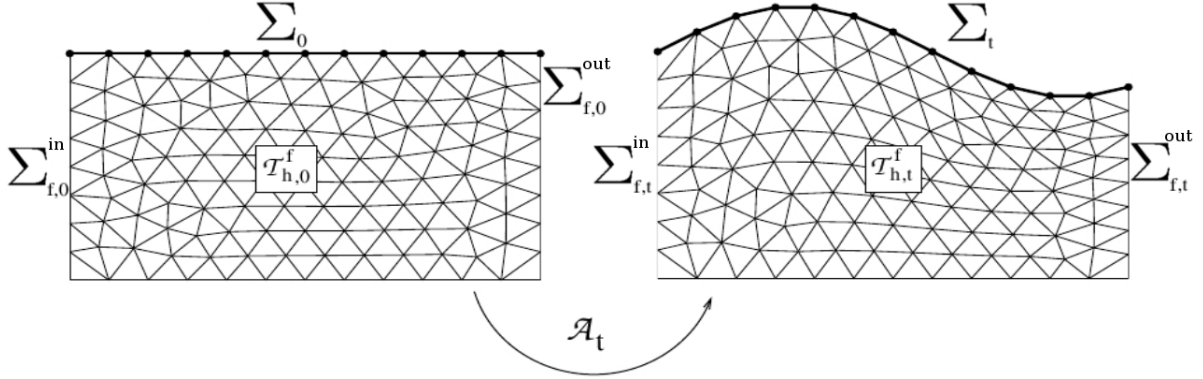


Figure 4.2: Moving mesh.

domain velocity tends to zero. We observe that, whatever it happens inside the domain, on the borders two constraints must be respected, namely

$$\begin{cases} \boldsymbol{\eta}_m = \mathbf{h} & \text{on } \Sigma, \\ \boldsymbol{\eta}_m = \mathbf{0} & \text{on } \Sigma_f. \end{cases} \quad (4.1)$$

The ALE formulation is *Lagrangian-Eulerian* because it satisfy (4.1), following a Lagrangian treatment for Navier-Stokes equations on the physical interface and an Eulerian one on the artificial sections, and it is *Arbitrary* because we choose which problem to solve inside the physical and artificial borders. Between all the possible choices, we will solve an harmonic extension problem.

Let \mathcal{A}_t be a family of mappings (see fig.4.3), which at each $t \in (t_0, T)$ associates a point $\widehat{\mathbf{x}}$ of the fluid reference configuration $\widehat{\Omega}_f$ (for instance the domain configuration at time $t = t_0$) to a point \mathbf{x} in the current fluid configuration Ω_f ,

$$\mathcal{A}_t : \widehat{\Omega}_f \subset \mathbb{R}^3 \rightarrow \Omega_f \subset \mathbb{R}^3, \quad \mathbf{x}(\widehat{\mathbf{x}}, t) = \mathcal{A}_t(\widehat{\mathbf{x}}). \quad (4.2)$$

\mathcal{A}_t is assumed to be an homeomorphism, that is $\mathcal{A}_t \in C^0(\widehat{\Omega}_f)$ is invertible with continuous inverse $\mathcal{A}_t^{-1} \in C^0(\Omega_f)$. In addition, we assume that the application

$$t \rightarrow \mathbf{x}(\widehat{\mathbf{x}}, t), \quad \widehat{\mathbf{x}} \in \widehat{\Omega}_f,$$

is differentiable almost everywhere in $[t_0, T]$.

The coordinates $\widehat{\mathbf{x}} \in \widehat{\Omega}_f$ are the ALE coordinates, while $\mathbf{x} = \mathbf{x}(\widehat{\mathbf{x}}, t) \in \Omega_f$ will be denoted as the spatial coordinates. Let us define a function v defined on the Eulerian frame

$$v : \Omega_f \times [t_0, T] \rightarrow \mathbb{R},$$

and the corresponding function $\widehat{v} := v \circ \mathcal{A}_t$ on the ALE frame

$$\widehat{v} : \widehat{\Omega}_f \times [t_0, T] \rightarrow \mathbb{R}, \quad \widehat{v}(\widehat{\mathbf{x}}, t) := v(\mathcal{A}_t(\widehat{\mathbf{x}}), t).$$

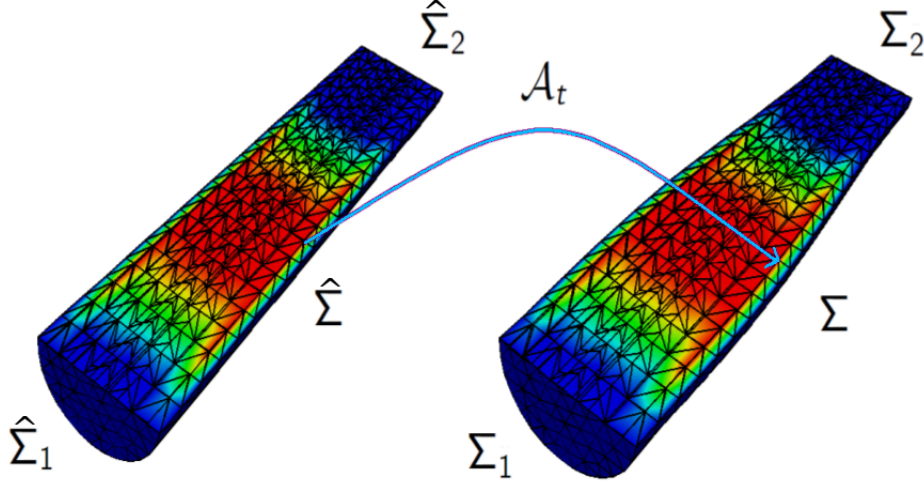


Figure 4.3: The ALE frame described by the map \mathcal{A}_t , which maps a reference (initial) domain into the current one. Σ is the fluid-structure interface, while Σ_1 and Σ_2 are the inlet and the outlet surfaces respectively.

The symbol $\frac{D^A}{Dt}$ will indicate the time derivative on the ALE frame, written in the spatial coordinates:

$$\frac{D^A v}{Dt} : \Omega_f \times [t_0, T] \rightarrow \mathbb{R}, \quad \frac{D^A v}{Dt}(\hat{\mathbf{x}}, t) = \frac{\partial \hat{v}}{\partial t}(\hat{\mathbf{x}}, t), \quad \hat{\mathbf{x}} = \mathcal{A}_t^{-1}(\mathbf{x}).$$

We can now define the fluid domain velocity \mathbf{u}_m as

$$\mathbf{u}_m := \frac{D^A \mathbf{x}}{Dt}.$$

and, using the classical chain rule on the time derivative, for a given function w we have

$$\frac{D^A w}{Dt} = \frac{\partial w}{\partial t} + \frac{D^A \mathbf{x}}{Dt} \cdot \nabla w = \frac{\partial w}{\partial t} + \mathbf{u}_m \cdot \nabla w.$$

Harmonic extension problem. Let us suppose to know the moving boundary displacement $\mathbf{h}(t) : \partial\hat{\Omega}_f \rightarrow \Omega_f$ for any $t \in [t_0, T]$. We consider an harmonic extension of the datum $\mathbf{h}(t)$ in order to calculate the fluid domain displacement $\hat{\boldsymbol{\eta}}_m(t)$ also in the internal points:

Given $\hat{\Omega}_f$ and $\mathbf{h}(t)$, find $\hat{\boldsymbol{\eta}}_m(t) : \hat{\Omega}_f \rightarrow \Omega_f$ for any $t \in [t_0, T]$ such that

$$\begin{cases} -\Delta \hat{\boldsymbol{\eta}}_m(t) = 0 & \text{in } \hat{\Omega}_f, \\ \hat{\boldsymbol{\eta}}_m(t) = \mathbf{h}(t) & \text{on } \partial\hat{\Omega}_f. \end{cases} \quad (4.3)$$

The fluid domain velocity will be easily recovered in the following manner

$$\mathbf{u}_m = \frac{\partial \hat{\boldsymbol{\eta}}_m}{\partial t}. \quad (4.4)$$

Fluid problem. Denoting by $\mathbf{u}_f(\mathbf{x}, t)$ the fluid velocity, p_f the fluid pressure and ρ_f the fluid density, we can introduce the Navier-Stokes equations defined in the Eulerian frame [94, 95]:

$$\begin{cases} \rho_f \frac{\partial \mathbf{u}_f}{\partial t} + \rho_f (\mathbf{u}_f \cdot \nabla) \mathbf{u}_f - \nabla \cdot \mathbf{T}_f(\mathbf{u}_f, p_f) = \mathbf{f}_f, & \text{in } [t_0, T] \times \Omega_f, \\ \nabla \cdot \mathbf{u}_f = 0, & \text{in } [t_0, T] \times \Omega_f, \end{cases} \quad (4.5)$$

where \mathbf{f}_f represents body forces (per unit volume) acting on the fluid and \mathbf{T}_f is the *Cauchy stress tensor*

$$\mathbf{T}_f(\mathbf{u}_f, p_f) = 2\mu \mathbf{D}(\mathbf{u}_f) - p_f \mathbb{I} \quad \text{and} \quad \mathbf{D}(\mathbf{u}_f) = \frac{\nabla \mathbf{u}_f + (\nabla \mathbf{u}_f)^T}{2},$$

where \mathbb{I} is the identity tensor and μ is the dynamic viscosity, which here is taken as a positive constant.

We have seen that map \mathcal{A}_t allows to conveniently express the time variation of relevant quantities (displacement, velocity, pressure) at the nodes of the moving computational mesh. I would not write Navier-Stokes equations in an eulerian frame because the fluid domain is moving, and I would not use their lagrangian formulation too because the fluid domain is fixed at the artificial borders. I want to write Navier-Stokes equation in a suitable system that is joint with map \mathcal{A}_t . From the Reynold's transport formula, we use the total time derivative written in a frame wich follows a particular direction \mathbf{l} :

$$\frac{D\mathbf{v}}{Dt} := \frac{\partial \mathbf{v}}{\partial t} - (\mathbf{u}_f - \mathbf{l}) \cdot \nabla_x \mathbf{v}, \quad (4.6)$$

where $(\mathbf{u}_f - \mathbf{l})$ is the effective convective term seen from the chosen frame. Relation (4.6) states that the variation in time of a quantity \mathbf{v} is made up of a part belonging to the node of the mesh ($\frac{\partial \mathbf{v}}{\partial t}$) and a part due to node movement with velocity \mathbf{u}_f . We observe that \mathbf{l} is the reference frame velocity. If $\mathbf{l} = \mathbf{u}_f$ we obtain the lagrangian formulation, if $\mathbf{l} = 0$ we come back to the eulerian one. When we choose the fluid domain as the reference frame we have $\mathbf{l} = \mathbf{u}_m$ and we obtain the Navier-Stokes equations in the ALE formulation [96, 47]:

$$\begin{cases} \rho_f \frac{D^A \mathbf{u}_f}{Dt} + \rho_f ((\mathbf{u}_f - \mathbf{u}_m) \cdot \nabla) \mathbf{u}_f - \nabla \cdot \mathbf{T}_f(\mathbf{u}_f, p_f) = \mathbf{f}_f, & \text{in } [t_0, T] \times \Omega_f, \\ \nabla \cdot \mathbf{u}_f = 0, & \text{in } [t_0, T] \times \Omega_f, \end{cases} \quad (4.7)$$

We must add to these equations some initial conditions for the velocity field

$$\mathbf{u}_f(\mathbf{x}, 0) = \mathbf{u}_f^0 \quad \text{in } \widehat{\Omega}_f,$$

and suitable boundary conditions. The boundary $\partial\Omega_f$ can be splitted into two non-overlapping parts $\partial\Omega_f = \Sigma_{f,D} \cup \Sigma_{f,N}$, in order to consider the following boundary conditions

$$\begin{cases} \mathbf{u}_f = \boldsymbol{\phi}_f & \text{on } \Sigma_{f,D}, \\ \mathbf{T}_f \cdot \mathbf{n} = \boldsymbol{\psi}_f & \text{on } \Sigma_{f,N}, \end{cases}$$

where \mathbf{n} is the unit outward normal vector to $\partial\Omega_f$ and $\boldsymbol{\phi}_f, \boldsymbol{\psi}_f$ are two given data with enough regularity.

4.3 Finite element formulation

4.3.1 Weak formulation for the fluid and the fluid domain problems

Harmonic extension problem. The weak formulation of the problem (4.3) needs the introduction of the following functional spaces:

$$\begin{aligned}\widehat{\mathbf{V}}_m &= [H^1(\widehat{\Omega}_f)]^3, \\ \widehat{\mathbf{V}}_m^D &= [H_{\Sigma_{f,D}}(\widehat{\Omega}_f)]^3 = \left\{ \widehat{\mathbf{v}} \in \widehat{\mathbf{V}}_f, \widehat{\mathbf{v}} = \mathbf{0} \text{ on } \widehat{\Sigma}_{f,D} \right\}.\end{aligned}\quad (4.8)$$

Then the weak formulation of problem (4.3) reads:

Weak-formulation 4.1. (*Continuous setting*). Find $t \rightarrow \widehat{\boldsymbol{\eta}}_m(t) \in \widehat{\mathbf{V}}_m$, with $\widehat{\boldsymbol{\eta}}_m(t) = \mathbf{h}(t)$ on $\Sigma_{m,D}$, such that

$$\int_{\widehat{\Omega}_f} \widehat{\boldsymbol{\eta}}_m(t) \cdot \widehat{\mathbf{v}} \, d\Omega = 0, \quad \forall \widehat{\mathbf{v}} \in \widehat{\mathbf{V}}_m^D. \quad (4.9)$$

Fluid problem. In order to write the weak formulation of problem (4.7) we need to introduce the following functional spaces:

$$\begin{aligned}\widehat{\mathbf{V}}_f &= [H^1(\widehat{\Omega}_f)]^3, \\ \widehat{\mathbf{V}}_f^D &= [H_{\Sigma_{f,D}}(\widehat{\Omega}_f)]^3 = \left\{ \widehat{\mathbf{v}} \in \widehat{\mathbf{V}}_f, \widehat{\mathbf{v}} = \mathbf{0} \text{ on } \widehat{\Sigma}_{f,D} \right\}, \\ \widehat{Q}_f &= L^2(\widehat{\Omega}_f), \\ \widehat{Q}_{f,0} &= \left\{ \widehat{q} \in \widehat{Q}_f, \int_{\widehat{\Omega}_f} \widehat{q} \, d\Omega = 0 \right\},\end{aligned}\quad (4.10)$$

and

$$\mathbf{V}_f = \left\{ \mathbf{v} : \Omega_f \times I \rightarrow \mathbb{R}^3, \mathbf{v} = \widehat{\mathbf{v}} \circ \mathcal{A}_t^{-1}, \widehat{\mathbf{v}} \in \widehat{\mathbf{V}}_f \right\}, \quad (4.11)$$

$$Q_f = \left\{ q : \Omega_f \times I \rightarrow \mathbb{R}, q = \widehat{q} \circ \mathcal{A}_t^{-1}, \widehat{q} \in \widehat{Q}_f \right\}. \quad (4.12)$$

\mathbf{V}_f^D is defined in a similar manner. We illustrate now two possible weak formulations for the fluid problem in the ALE frame taken from [97].

The weak non-conservative formulation of the problem (4.7) reads:

Weak-formulation 4.2. (*Continuous setting*). For almost every $t \in I$, find $t \rightarrow \mathbf{u}_f(t) \in \mathbf{V}_f$,

4.3. Finite element formulation

with $\mathbf{u}_f(t) = \boldsymbol{\phi}_f(t)$ on $\Sigma_{f,D}$, $\mathbf{u}_f(0) = \mathbf{u}_f^0$ in $\widehat{\Omega}_f$ and find $t \rightarrow p_f(t) \in Q_f$ such that

$$\begin{cases} \rho_f \int_{\Omega_f} \frac{D^A \mathbf{u}_f}{Dt} \cdot \mathbf{v} d\Omega + \rho_f \int_{\Omega_f} ((\mathbf{u}_f - \mathbf{u}_m) \cdot \nabla) \mathbf{u}_f \cdot \mathbf{v} d\Omega \\ + 2\mu \int_{\Omega_f} \mathbf{D}(\mathbf{u}_f) : \nabla \mathbf{v} d\Omega - \int_{\Omega_f} p_f \nabla \cdot \mathbf{v} d\Omega = \int_{\Omega_f} \mathbf{f}_f \cdot \mathbf{v} d\Omega + \int_{\Sigma_{f,N}} \boldsymbol{\psi}_f \cdot \mathbf{v} d\gamma & \forall \mathbf{v} \in \mathbf{V}_f^D, \\ \int_{\Omega_f} \nabla \cdot \mathbf{u}_f q = 0 & \forall q \in Q_f. \end{cases} \quad (4.13)$$

We remark that if $\Sigma_{f,N} = 0$ the space \mathbf{V}_f^D coincides with $[H_0^1(\Omega_f)]^3$. In this case the space Q_f in (4.13) should be replaced by $Q_{f,0}$ (i.e. the pressure is defined up to a constant) and the non-homogeneous Dirichlet boundary datum $\boldsymbol{\psi}_f(t)$ must satisfy the compatibility condition

$$\int_{\partial\Omega_f} \boldsymbol{\phi}_f(t) \cdot \mathbf{n} d\gamma = 0 \quad \forall t \in I.$$

The weak conservative formulation of the problem (4.7) reads:

Weak-formulation 4.3. (*Continuous setting*). For almost every $t \in I$, find $t \rightarrow \mathbf{u}_f(t) \in \mathbf{V}_f$, with $\mathbf{u}_f(t) = \boldsymbol{\phi}_f(t)$ on $\Sigma_{f,D}$, $\mathbf{u}_f(0) = \mathbf{u}_f^0$ in $\widehat{\Omega}_f$ and find $t \rightarrow p_f(t) \in Q_f$ such that

$$\begin{cases} \rho_f \frac{d}{dt} \int_{\Omega_f} \mathbf{u}_f \cdot \mathbf{v} d\Omega + \rho_f \int_{\Omega_f} \nabla \cdot ((\mathbf{u}_f - \mathbf{u}_m) \otimes \mathbf{u}_f) \cdot \mathbf{v} d\Omega \\ + 2\mu \int_{\Omega_f} \mathbf{D}(\mathbf{u}_f) : \nabla \mathbf{v} d\Omega - \int_{\Omega_f} p_f \nabla \cdot \mathbf{v} d\Omega = \int_{\Omega_f} \mathbf{f}_f \cdot \mathbf{v} d\Omega + \int_{\Sigma_{f,N}} \boldsymbol{\psi}_f \cdot \mathbf{v} d\gamma & \forall \mathbf{v} \in \mathbf{V}_f^D, \\ \int_{\Omega_f} \nabla \cdot \mathbf{u}_f q = 0 & \forall q \in Q_f. \end{cases} \quad (4.14)$$

where the symbol \otimes indicates the tensor product and gives us the possibility to write the convective term in conservative form. The conservative form states that, in absence of source terms, the variation of \mathbf{u}_f over the domain Ω_f is due only to boundary terms (for details see [97]).

4.3.2 Finite element discretization

For the finite element approximation of problem (4.13), or equivalently (4.14), we need both the fluid equations discretization and the fluid domain movement one. We consider a triangulation $\widehat{\mathcal{T}}_{f,h}$ of the reference domain $\widehat{\Omega}_f$, which is here supposed made up of elements with straight edges, for simplicity. In addition, let us consider the space of finite elements

$\mathcal{F}_n(\widehat{\mathcal{T}}_{f,h})$ of degree n . In literature there are many finite element spaces $\widehat{\mathbf{V}}_{f,h}$ and $\widehat{Q}_{f,h}$ that approximate $\widehat{\mathbf{V}}_f$ and \widehat{Q}_f respectively, satisfying the *inf-sup* (or *LBB*) condition [98]:

$$\inf_{\widehat{q}_h \in \widehat{Q}_{f,h}} \sup_{\widehat{\mathbf{v}}_h \in \widehat{\mathbf{V}}_{f,h}} \frac{\int_{\widehat{\Omega}_f} \nabla \cdot \widehat{\mathbf{v}}_h q_h \, d\Omega}{\|\widehat{\mathbf{v}}_h\|_{H^1(\widehat{\Omega}_f)} \|\widehat{q}_h\|_{L^2(\widehat{\Omega}_f)}} \geq \beta, \quad (4.15)$$

where the constant $\beta > 0$ is independent from h . We remind that this property is necessary for the well posedness of the discrete problem and the optimal convergence of the method. Among the choices that satisfy (4.15), we mention the Taylor-Hood finite elements $\mathbb{P}_2 - \mathbb{P}_1$ and the choice *P₁ bubble* – *P₁*, where a piecewise linear approximation for the pressure is employed and the velocity is approximated by piecewise linear functions suitably enriched with bubble functions which are element-based polynomials that vanish on the element boundary.

The proper ALE extension of the discrete spaces to a moving domain are

$$\mathbf{V}_{f,h} = \left\{ \mathbf{v}_h : \Omega_{f,h} \times I \rightarrow \mathbb{R}^3, \mathbf{v}_h = \widehat{\mathbf{v}}_h \circ \mathcal{A}_{h,t}^{-1}, \widehat{\mathbf{v}}_h \in \widehat{\mathbf{V}}_{f,h} \right\}, \quad (4.16)$$

$$Q_{f,h} = \left\{ q : \Omega_{f,h} \times I \rightarrow \mathbb{R}, q_h = \widehat{q}_h \circ \mathcal{A}_{h,t}^{-1}, \widehat{q}_h \in \widehat{Q}_{f,h} \right\}. \quad (4.17)$$

where $\Omega_{f,h} = \mathcal{A}_{h,t}(\widehat{\Omega}_h)$, with $\mathcal{A}_{h,t}$ the discrete ALE mapping obtained by a finite element approximation of the harmonic extension problem (4.3).

The discrete version of the non-conservative problem (4.13) reads:

Weak-formulation 4.4. (*Discrete setting*). For almost every $t \in I$, find $t \rightarrow \mathbf{u}_{f,h}(t) \in \mathbf{V}_{f,h}$, with $\mathbf{u}_{f,h}(t) = \phi_{f,h}(t)$ on $\Sigma_{f,D}$, $\mathbf{u}_{f,h}(0) = \mathbf{u}_{f,h}^0$ in $\widehat{\Omega}_f$ and find $t \rightarrow p_{f,h}(t) \in Q_{f,h}$ such that

$$\left\{ \begin{array}{l} \rho_f \int_{\Omega_f} \frac{D^A \mathbf{u}_{f,h}}{Dt} \cdot \mathbf{v}_h \, d\Omega + \rho_f \int_{\Omega_f} ((\mathbf{u}_{f,h} - \mathbf{u}_{m,h}) \cdot \nabla) \mathbf{u}_{f,h} \cdot \mathbf{v}_h \, d\Omega \\ \quad + 2\mu \int_{\Omega_f} \mathbf{D}(\mathbf{u}_{f,h}) : \nabla \mathbf{v}_h \, d\Omega - \int_{\Omega_f} p_{f,h} \nabla \cdot \mathbf{v}_h \, d\Omega \\ = \int_{\Omega_f} \mathbf{f}_f \cdot \mathbf{v}_h \, d\Omega + \int_{\Sigma_{f,N}} \boldsymbol{\psi}_f \cdot \mathbf{v}_h \, d\gamma \\ \int_{\Omega_f} \nabla \cdot \mathbf{u}_{f,h} q_h = 0 \end{array} \right. \quad \begin{array}{l} \forall \mathbf{v}_h \in \mathbf{V}_{f,h} \cap \mathbf{V}_{f,h}^D, \\ \forall q_h \in Q_{f,h}. \end{array} \quad (4.18)$$

where $\phi_{f,h}$ and $\mathbf{u}_{f,h}^0$ are suitable approximations of ϕ_f and \mathbf{u}_f^0 , respectively, and $\mathbf{u}_{m,h}$ is the discrete fluid domain velocity

$$\mathbf{u}_{m,h} = \frac{\partial \widehat{\boldsymbol{\eta}}_{m,h}}{\partial t}. \quad (4.19)$$

In (4.19), $\widehat{\boldsymbol{\eta}}_{m,h}$ is the solution of the following discrete harmonic extension problem:

4.3. Finite element formulation

Weak-formulation 4.5. (*Discrete setting*). Find $t \rightarrow \widehat{\boldsymbol{\eta}}_{m,h}(t) \in \widehat{\mathbf{V}}_{m,h}$, with $\widehat{\boldsymbol{\eta}}_{m,h}(t) = \mathbf{h}(t)$ on $\widehat{\Sigma}_f$, such that

$$\int_{\widehat{\Omega}_f} \widehat{\boldsymbol{\eta}}_{m,h}(t) \cdot \widehat{\mathbf{v}}_h \, d\Omega = 0 \quad \forall \widehat{\mathbf{v}}_h \in \widehat{\mathbf{V}}_{m,h}, \quad (4.20)$$

where $\widehat{\mathbf{V}}_{m,h} \subset \widehat{\mathbf{V}}$.

We remark that if $\Sigma_{f,N} = 0$ and $\boldsymbol{\phi}_f = \mathbf{0}$, the convective term

$$\int_{\Omega_f} (\mathbf{u}_f \cdot \nabla) \mathbf{u}_f \cdot \mathbf{v} \, d\Omega$$

does not contribute to the energy of the system (4.13). Indeed, by taking $\mathbf{v} = \mathbf{u}_f$ we have

$$\int_{\Omega_f} (\mathbf{u}_f \cdot \nabla) \mathbf{u}_f \cdot \mathbf{u}_f \, d\Omega = \frac{1}{2} \int_{\Omega_f} \mathbf{u}_f \cdot |\mathbf{u}_f|^2 \, d\Omega = -\frac{1}{2} \int_{\Omega_f} \nabla \cdot \mathbf{u}_f |\mathbf{u}_f|^2 \, d\Omega,$$

where the last term is equal to zero thanks to (4.13)₂ and to the fact that $|\mathbf{u}_f|^2 \in Q_f$. This property is not true at the discrete level in (4.18). Indeed,

$$\int_{\Omega_f} (\mathbf{u}_{f,h} \cdot \nabla) \mathbf{u}_{f,h} \cdot \mathbf{u}_{f,h} \, d\Omega = -\frac{1}{2} \int_{\Omega_f} \nabla \cdot \mathbf{u}_{f,h} |\mathbf{u}_{f,h}|^2 \, d\Omega \neq 0,$$

since, in general, $|\mathbf{u}_{f,h}|^2 \notin Q_{f,h}$. Then we obtain the correct energy balance (at least in the case of a fully Dirichlet problem) modifying (4.18) in a consistent way, i.e. by adding to (4.18)₁ the term

$$\frac{1}{2} \int_{\Omega_f} \nabla \cdot \mathbf{u}_{f,h} \mathbf{u}_{f,h} \cdot \mathbf{v}_h \, d\Omega,$$

in order to recover the stability property at the discrete level too. This modification is consistent since (4.7)₁ holds. In the sequel, we will always consider this modified problem.

The weak stabilized non-conservative formulation of the problem (4.7) reads:

Weak-formulation 4.6. (*Discrete setting*). For almost every $t \in I$, find $t \rightarrow \mathbf{u}_{f,h}(t) \in \mathbf{V}_{f,h}$, with $\mathbf{u}_{f,h}(t) = \boldsymbol{\phi}_{f,h}(t)$ on $\Sigma_{f,D}$, $\mathbf{u}_{f,h}(0) = \mathbf{u}_{f,h}^0$ in $\widehat{\Omega}_f$ and find $t \rightarrow p_{f,h}(t) \in Q_{f,h}$ such that

$$\left\{ \begin{array}{l} \rho_f \int_{\Omega_f} \frac{D^A \mathbf{u}_{f,h}}{Dt} \cdot \mathbf{v}_h \, d\Omega + \rho_f \int_{\Omega_f} ((\mathbf{u}_{f,h} - \mathbf{u}_{m,h}) \cdot \nabla) \mathbf{u}_{f,h} \cdot \mathbf{v}_h \, d\Omega \\ \quad + \frac{\rho_f}{2} \int_{\Omega_f} \nabla \cdot \mathbf{u}_{f,h} \mathbf{u}_{f,h} \cdot \mathbf{v}_h \, d\Omega + 2\mu \int_{\Omega_f} \mathbf{D}(\mathbf{u}_{f,h}) : \nabla \mathbf{v}_h \, d\Omega \\ \quad - \int_{\Omega_f} p_{f,h} \nabla \cdot \mathbf{v}_h \, d\Omega = \int_{\Omega_f} \mathbf{f}_f \cdot \mathbf{v}_h \, d\Omega + \int_{\Sigma_{f,N}} \boldsymbol{\psi}_f \cdot \mathbf{v}_h \, d\gamma \quad \forall \mathbf{v}_h \in \mathbf{V}_{f,h} \cap \mathbf{V}_{f,h}^D, \\ \int_{\Omega_f} \nabla \cdot \mathbf{u}_{f,h} q_h = 0 \quad \forall q_h \in Q_{f,h}. \end{array} \right. \quad (4.21)$$

Let $\{\psi_i\}_{i=1}^{N_p}$ be the Lagrange basis associated to the space $Q_{f,h}$ and $\{\varphi_j\}_{j=1}^{N_v}$ those associated to $\mathbf{V}_{f,h} \cup \mathbf{V}_{f,h}^D$. In addition, let $\{\varphi_k^b\}_{k=1}^{N_v^b}$ be the set of basis functions corresponding to the nodes on $\Sigma_{f,D}$, such that $\{\varphi_j\} \oplus \{\varphi_k^b\}$ is a basis for $\mathbf{V}_{f,h}$. We set

$$\mathbf{u}_{f,h}(\mathbf{x}, t) = \sum_{j=1}^{N_v} u_j(t) \varphi_j(\mathbf{x}, t) + \sum_{j=1}^{N_v^b} u_j^b(t) \varphi_j^b(\mathbf{x}, t),$$

and

$$p_{f,h}(\mathbf{x}, t) = \sum_{j=1}^{N_p} p_j(t) \psi_j(\mathbf{x}, t).$$

where the nodal values u_j^b are known from the boundary datum ϕ_f , and $\{u_j\}$ and $\{p_j\}$ are the unknowns of the problem.

The weak stabilized conservative formulation of the problem (4.7) reads:

Weak-formulation 4.7. (*Discrete setting*). For almost every $t \in I$, find $t \rightarrow \mathbf{u}_{f,h}(t) \in \mathbf{V}_{f,h}$, with $\mathbf{u}_{f,h}(t) = \phi_{f,h}(t)$ on $\Sigma_{f,D}$, $\mathbf{u}_{f,h}(0) = \mathbf{u}_{f,h}^0$ in $\widehat{\Omega}_f$ and find $t \rightarrow p_{f,h}(t) \in Q_{f,h}$ such that

$$\left\{ \begin{array}{l} \rho_f \frac{d}{dt} \int_{\Omega_f} \mathbf{u}_{f,h} \cdot \mathbf{v}_h \, d\Omega + \rho_f \int_{\Omega_f} \nabla \cdot ((\mathbf{u}_{f,h} - \mathbf{u}_{m,h}) \otimes \mathbf{u}_{f,h}) \cdot \mathbf{v}_h \, d\Omega \\ - \frac{\rho_f}{2} \int_{\Omega_f} \nabla \cdot \mathbf{u}_{f,h} \mathbf{u}_{f,h} \cdot \mathbf{v}_h \, d\Omega + 2\mu \int_{\Omega_f} \mathbf{D}(\mathbf{u}_{f,h}) : \nabla \mathbf{v}_h \, d\Omega \\ - \int_{\Omega_f} p_{f,h} \nabla \cdot \mathbf{v}_h \, d\Omega = \int_{\Omega_f} \mathbf{f}_f \cdot \mathbf{v}_h \, d\Omega + \int_{\Sigma_{f,N}} \boldsymbol{\psi}_f \cdot \mathbf{v}_h \, d\gamma \quad \forall \mathbf{v}_h \in \mathbf{V}_{f,h} \cap \mathbf{V}_{f,h}^D, \\ \int_{\Omega_f} \nabla \cdot \mathbf{u}_{f,h} q_h = 0 \quad \forall q_h \in Q_{f,h}, \end{array} \right. \quad (4.22)$$

4.3.3 Time discretization

Let Δt be the time discretization parameter and $t^n = n\Delta t$, $n \in \mathbb{N}$. Given a generic function z , we denote by z^n the approximation of $z(t^n)$. We consider a *backward Euler scheme* to discretize in time equations (4.21) and (4.22).

4.3. Finite element formulation

We can now discretize the non-conservative formulation (4.21) obtaining

$$\left\{ \begin{array}{l}
 \rho_f \frac{1}{\Delta t} \int_{\Omega_f^{n+1}} \mathbf{u}_{f,h}^{n+1} \cdot \mathbf{v}_h \, d\Omega + \rho_f \int_{\Omega_f^{n+1}} ((\mathbf{u}_{f,h}^* - \mathbf{u}_{m,h}^*) \cdot \nabla) \mathbf{u}_{f,h}^{n+1} \cdot \mathbf{v}_h \, d\Omega \\
 + \frac{\rho_f}{2} \int_{\Omega_f^{n+1}} \nabla \cdot \mathbf{u}_{f,h}^* \mathbf{u}_{f,h}^{n+1} \cdot \mathbf{v}_h \, d\Omega + 2\mu \int_{\Omega_f^{n+1}} \mathbf{D}(\mathbf{u}_{f,h}^{n+1}) : \nabla \mathbf{v}_h \, d\Omega \\
 - \int_{\Omega_f^{n+1}} p_{f,h}^{n+1} \nabla \cdot \mathbf{v}_h \, d\Omega = \int_{\Omega_f^{n+1}} \mathbf{f}_f \cdot \mathbf{v}_h \, d\Omega \\
 + \int_{\Sigma_{f,N}^{n+1}} \boldsymbol{\psi}_f^{n+1} \cdot \mathbf{v}_h \, d\gamma + \rho_f \frac{1}{\Delta t} \int_{\Omega_f^{n+1}} \mathbf{u}_{f,h}^n \cdot \mathbf{v}_h \, d\Omega \\
 \int_{\Omega_f^{n+1}} \nabla \cdot \mathbf{u}_{f,h}^{n+1} q_h = 0
 \end{array} \right. \quad \begin{array}{l}
 \forall \mathbf{v}_h \in \mathbf{V}_{f,h} \cap \mathbf{V}_{f,h}^D, \\
 \forall q_h \in Q_{f,h}.
 \end{array} \quad (4.23)$$

For the conservative formulation (4.22) we have

$$\left\{ \begin{array}{l}
 \rho_f \frac{1}{\Delta t} \int_{\Omega_f^{n+1}} \mathbf{u}_{f,h}^{n+1} \cdot \mathbf{v}_h \, d\Omega + \rho_f \int_{\Omega_f^{n+1}} \nabla \cdot ((\mathbf{u}_{f,h}^* - \mathbf{u}_{m,h}^*) \otimes \mathbf{u}_{f,h}^{n+1}) \cdot \mathbf{v}_h \, d\Omega \\
 - \frac{\rho_f}{2} \int_{\Omega_f^{n+1}} \nabla \cdot \mathbf{u}_{f,h}^* \mathbf{u}_{f,h}^{n+1} \cdot \mathbf{v}_h \, d\Omega + 2\mu \int_{\Omega_f^{n+1}} \mathbf{D}(\mathbf{u}_{f,h}^{n+1}) : \nabla \mathbf{v}_h \, d\Omega \\
 - \int_{\Omega_f^{n+1}} p_{f,h}^{n+1} \nabla \cdot \mathbf{v}_h \, d\Omega = \int_{\Omega_f^{n+1}} \mathbf{f}_f \cdot \mathbf{v}_h \, d\Omega \\
 + \int_{\Sigma_{f,N}^{n+1}} \boldsymbol{\psi}_f^{n+1} \cdot \mathbf{v}_h \, d\gamma + \rho_f \frac{1}{\Delta t} \int_{\Omega_f^{n+1}} \mathbf{u}_{f,h}^{n+1} \cdot \mathbf{v}_h \, d\Omega \\
 \int_{\Omega_f^{n+1}} \nabla \cdot \mathbf{u}_{f,h}^{n+1} q_h = 0
 \end{array} \right. \quad \begin{array}{l}
 \forall \mathbf{v}_h \in \mathbf{V}_{f,h} \cap \mathbf{V}_{f,h}^D, \\
 \forall q_h \in Q_{f,h},
 \end{array} \quad (4.24)$$

Chapter 5

Fluid-Structure Interaction

The purpose of this chapter is to introduce the equations describing the fluid-structure interaction (FSI) problem and to describe the partitioned strategies used for the numerical solution.

5.1 Introduction

FSI is present in many engineering situations like vibrations of aeronautics structures and suspended bridges, flow into pipelines, oscillations of long electrical cables spans, wind turbines and many others. FSI is a major issue in the haemodynamic field too. Indeed, in large arteries, blood flow interacts mechanically with the vessel wall, giving rise to a complex FSI mechanism with a continuous transfer of energy between the blood and the vessel structure (see, e.g., [99, 100, 48, 101, 102, 103, 20]). Typically, this substantial amount of energy, exchanged between fluid and structure in each cardiac cycle, generates a strongly non-linear coupled problem. The FSI problem is usually solved by considering the Arbitrary Lagrangian-Eulerian (ALE) formulation for the fluid problem [47, 96], which leads to the solution of a coupled problem, formed by three subproblems, namely the *fluid*, the *structure* and the *fluid domain* problems. The latter problem, typically an harmonic extension, is necessary to reconstruct the fluid domain. We remark that we do not have any structure domain problem since it coincides with the structure problem itself, due to the Lagrangian framework used for this problem.

5.2 The FSI problem

Starting from the description of the structure problem in chapter 2 and from the description of the fluid in moving domains in chapter 4, we can consider the coupled fluid-structure interaction problem, obtained when a fluid exchanges a significant amount of energy with a deformable solid. In this case, the fluid domain is an unknown of the problem and depends on the solid displacement at the FS interface. In particular, the interface position of the

fluid domain must coincide with the solid position at the interface, which is unknown since it depends on the interaction between the two subproblems. We refer to this source of non-linearity as *geometrical coupling*. In addition, we have to satisfy the continuity of the velocity and the continuity of the normal stresses at the FS interface. The former is the well-known *no-slip condition*, the latter comes from the action-reaction principle.

We consider an open domain $\Omega_f \subset \mathcal{R}^3$, see fig.5.1, to represent the lumen vessel in a certain instant t . The inflow and the outflow sections are denoted by $\Sigma_{f,i}$. The incompressible Navier-Stokes equations in ALE configuration for a Newtonian fluid (4.23) and (4.24) are assumed to hold in Ω_f .

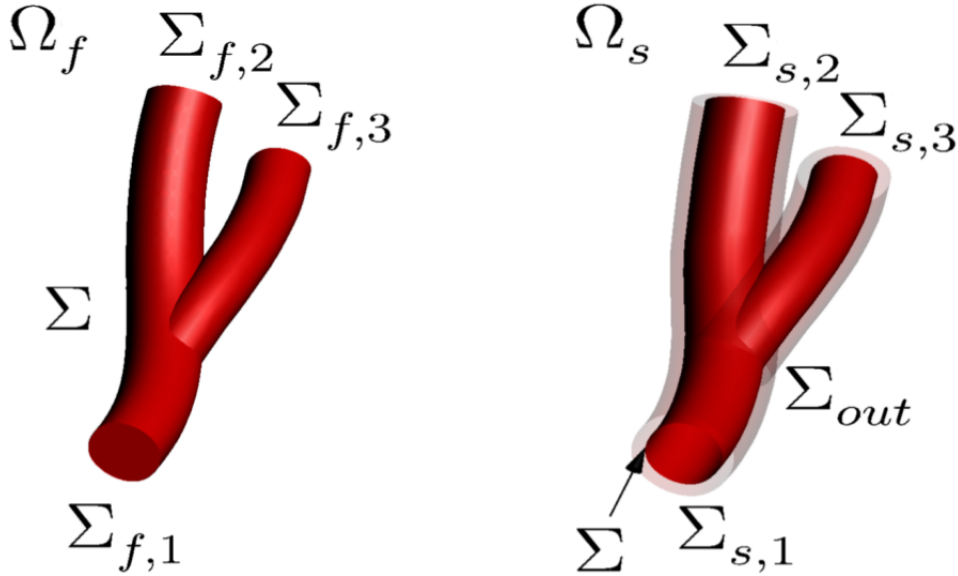


Figure 5.1: Description of the FSI domain: fluid domain Ω_f on the left, structure domain Ω_s on the right.

On the structural side, we consider an open domain $\Omega_s \subset \mathbb{R}^3$, see fig.5.1, to represent the vessel wall. The intersection of Ω_s and Ω_f is empty, and $\Sigma = \Omega_s \cup \Omega_f$ is the FS interface. We define a normal unit vector \mathbf{n} on Σ , pointing outward of the solid domain and inward to the fluid domain. The inflow and the outflow sections are denoted by $\Sigma_{s,i}$, and Σ_{out} represents the external surface of the structure domain.

The FSI problem in the strong formulation and in the ALE frame reads

1. **Fluid-Structure problem.** *Given the (unknown) fluid domain velocity \mathbf{u}_m and the fluid domain Ω_f , find, at each time $t \in (t_0, T]$, the fluid velocity \mathbf{u}_f , the fluid pressure*

p_f , and the structure displacement $\boldsymbol{\eta}_s$ such that

$$\left\{ \begin{array}{ll} \rho_f \frac{D^A \mathbf{u}_f}{Dt} + \rho_f ((\mathbf{u}_f - \mathbf{u}_m) \cdot \nabla) \mathbf{u}_f - \nabla \cdot \mathbf{T}_f(\mathbf{u}_f, p_f) = \mathbf{f}_f, & \text{in } \Omega_f, \\ \nabla \cdot \mathbf{u}_f = 0, & \text{in } \Omega_f, \\ \hat{\rho}_s \frac{\partial^2 \hat{\boldsymbol{\eta}}_s}{\partial t^2} - \hat{\nabla} \cdot \mathbf{P}(\hat{\boldsymbol{\eta}}_s) = \hat{\mathbf{f}}_s, & \text{in } \hat{\Omega}_s, \\ \mathbf{u}_f = \frac{\partial \boldsymbol{\eta}_s}{\partial t}, & \text{on } \hat{\Sigma}, \\ \mathbf{T}_s(\boldsymbol{\eta}_s) \mathbf{n} - \mathbf{T}_f(\mathbf{u}_f, p_f) \mathbf{n} = \mathbf{0}, & \text{on } \hat{\Sigma}. \end{array} \right. \quad (5.1)$$

where the two matching conditions enforced at the FS interface are the *continuity of velocities* (5.1)₄ and the *continuity of normal stresses* (5.1)₅.

2. **Geometry problem.** Given the (unknown) interface structure displacement $\hat{\boldsymbol{\eta}}_s|_{\hat{\Sigma}}$, find the displacement of the points of the fluid domain $\boldsymbol{\eta}_m$ such that

$$\left\{ \begin{array}{ll} -\Delta \hat{\boldsymbol{\eta}}_m = \mathbf{0} & \text{in } \hat{\Omega}_f, \\ \hat{\boldsymbol{\eta}}_m = \hat{\boldsymbol{\eta}}_s & \text{on } \hat{\Sigma}, \end{array} \right. \quad (5.2)$$

and then find accordingly the fluid domain velocity

$$\hat{\mathbf{u}}_m = \frac{\partial \hat{\boldsymbol{\eta}}_m}{\partial t},$$

and the new points \mathbf{x}_f of the fluid domain by moving the points $\hat{\mathbf{x}}_f$ of the reference domain $\hat{\Omega}_f$ as

$$\mathbf{x}_f = \hat{\mathbf{x}}_f + \hat{\boldsymbol{\eta}}_m. \quad (5.3)$$

Note that now the physical border displacement $\mathbf{h} = \hat{\boldsymbol{\eta}}_s$ is unknown. We observe that (5.2)₂ guarantees the coincidence between the displacement of the fluid and the structure interface (geometrical conformity), whereas (5.3) guarantees that the mesh and structure velocities coincide at FS interface. Note that now the displacement at the physical border $\hat{\Sigma}$ is an unknown.

Problems (5.1) and (5.2) have to be endowed with suitable boundary conditions on $\Omega_f \cup \Sigma$ and $\hat{\Omega}_s \cup \hat{\Sigma}$, and with suitable initial conditions.

5.2.1 Time discretization

Applying a *backward Euler scheme*, time discretization of problems (5.1) and (5.2) reads as follows

1. **Fluid-Structure problem.** Given the (unknown) fluid domain velocity \mathbf{u}_m^{n+1} and the fluid domain Ω_f^{n+1} , the solution at previous time steps, and functions \mathbf{f}_f^{n+1} and \mathbf{f}_s^{n+1} , find fluid velocity \mathbf{u}_f^{n+1} , fluid pressure p_f^{n+1} , and structure displacement $\boldsymbol{\eta}_s^{n+1}$ such that

$$\left\{ \begin{array}{ll} \rho_f \frac{1}{\Delta t} \mathbf{u}_f^{n+1} + \rho_f ((\mathbf{u}_f^{n+1} - \mathbf{u}_m^{n+1}) \cdot \nabla) \mathbf{u}_f^{n+1} - \nabla \cdot \mathbf{T}_f(\mathbf{u}_f^{n+1}, p_f^{n+1}) = \mathbf{f}_f^{n+1} + \rho_f \frac{1}{\Delta t} \mathbf{u}_f^n, & \text{in } \Omega_f^{n+1}, \\ \nabla \cdot \mathbf{u}_f^{n+1} = 0, & \text{in } \Omega_f^{n+1}, \\ \hat{\rho}_s \frac{1}{\Delta t^2} (\hat{\boldsymbol{\eta}}_s^{n+1} - 2\hat{\boldsymbol{\eta}}_s^n + \hat{\boldsymbol{\eta}}_s^{n-1}) - \hat{\nabla} \cdot \mathbf{P}(\hat{\boldsymbol{\eta}}_s^{n+1}) = \hat{\mathbf{f}}_s^{n+1}, & \text{in } \hat{\Omega}_s, \\ \mathbf{u}_f^{n+1} = \mathbf{u}_s^{n+1}, & \text{on } \hat{\Sigma}^{n+1}, \\ \mathbf{T}_s(\boldsymbol{\eta}_s^{n+1})\mathbf{n} - \mathbf{T}_f(\mathbf{u}_f^{n+1}, p_f^{n+1})\mathbf{n} = \mathbf{0}, & \text{on } \hat{\Sigma}_{n+1}. \end{array} \right. \quad (5.4)$$

2. **Geometry problem.** Given the (unknown) interface structure displacement $\hat{\boldsymbol{\eta}}_s^{n+1}|_{\hat{\Sigma}}$, solve an harmonic extension problem

$$\left\{ \begin{array}{ll} -\Delta \hat{\boldsymbol{\eta}}_m^{n+1} = \mathbf{0} & \text{in } \hat{\Omega}_f, \\ \hat{\boldsymbol{\eta}}_m^{n+1} = \hat{\boldsymbol{\eta}}_s^{n+1} & \text{on } \hat{\Sigma}, \end{array} \right. \quad (5.5)$$

and then find accordingly the discrete fluid domain velocity by

$$\hat{\mathbf{u}}_m^{n+1} = \frac{1}{\Delta t} (\hat{\boldsymbol{\eta}}_m^{n+1} - \hat{\boldsymbol{\eta}}_m^n),$$

and the points \mathbf{x}_f^{n+1} of the new fluid domain by

$$\mathbf{x}_f^{n+1} = \hat{\mathbf{x}}_f^0 + \hat{\boldsymbol{\eta}}_m^{n+1}.$$

5.2.2 Boundary conditions

In this section we detail the inflow and outflow boundary conditions for the FSI problem considered in this work, as well as the condition we have imposed on the external surface Σ_{out} . In particular, some portions of the computational domain boundary do not correspond to any physical boundary and are just introduced to limit the domain of interest. In fig.5.1 the artificial boundaries are the sections $\Sigma_{f,j}$ and $\Sigma_{s,j}$, while Σ_{out} is a physical wall. For the fluid problem, we consider *flow rate conditions* necessary to impose the physiological data at the inlet section. Moreover, we define *absorbing conditions* useful to reduce non physiological reflection generated by artificial outlets. Instead, for the solid problem we consider a Robin condition to model the *surrounding tissue* on the external wall.

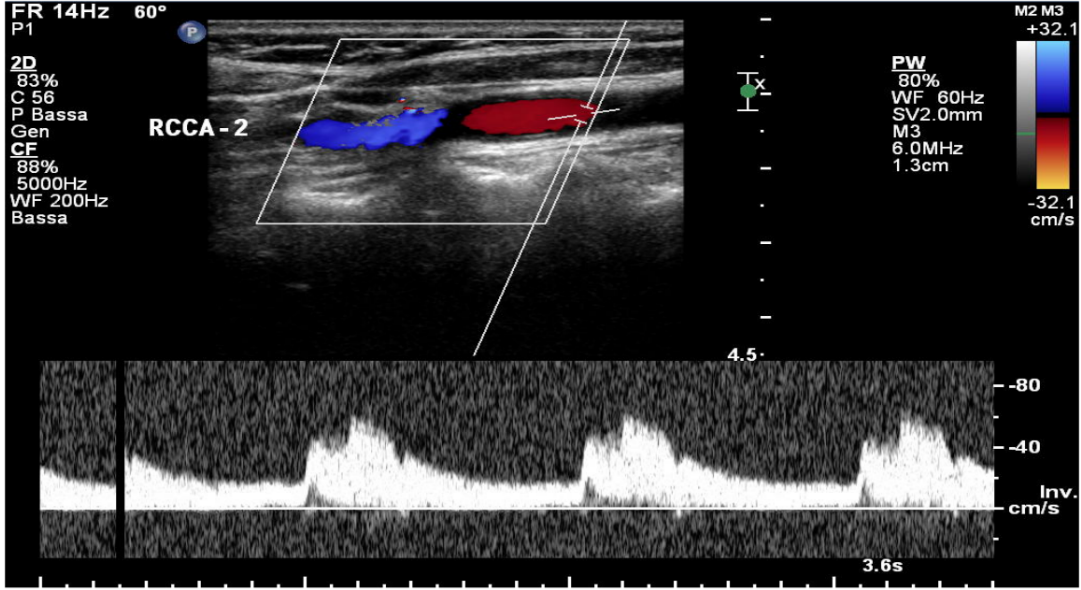


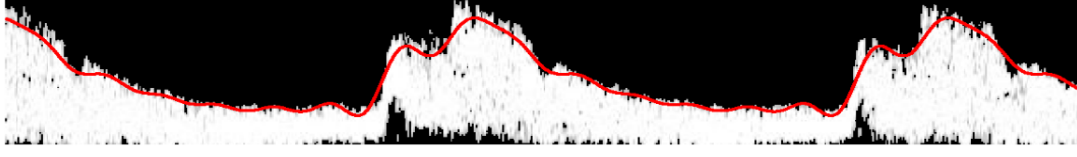
Figure 5.2: An image from an eco-color-doppler ultrasound machine.

Flow rate conditions. The prescription of boundary data on the artificial sections can be based on clinical measurements. Nevertheless, point-wise data are often not available. Indeed, the most common measurement techniques used in the clinical practice, as the *eco-color-doppler (ECD)*, gives *average data* for example of the velocity, over small volumes of blood of the lumen, as showed in fig.5.2. In particular, the eco-color-doppler signal can be regarded as an histogram, evolving in time, of the blood red cells velocity in the location of interest. Following [104, 105], the signal extracted from the eco-color-doppler image is obtained, after image noise removal with a threshold filter, computing the quantile of order 0.95 from all the histograms in time, as indicated with the red line in fig.5.3(a). This signal is then smoothed by projecting the signal on a Fourier basis with a Fourier transform estimated period. Then, from the velocity, we obtain the patient-specific *flow rate* (see fig.6.17). At the fluid inlet we prescribe this patient-specific flow rate

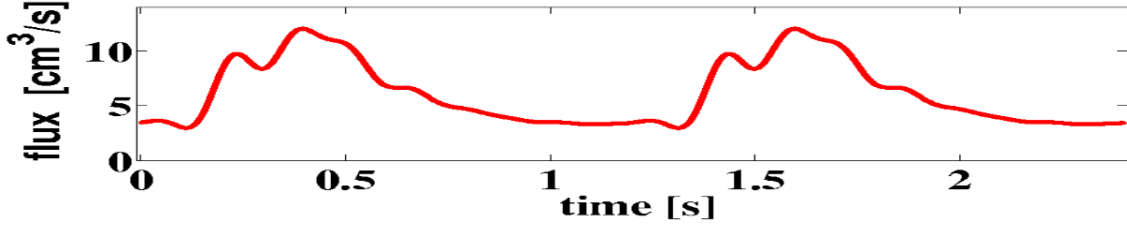
$$Q = \int_{\Omega_f} \mathbf{u}_f \cdot \mathbf{n} d\Omega, \quad (5.6)$$

and we impose a flat velocity profile. This imposition consists in a Dirichlet condition $\mathbf{u}_f = \mathbf{g}$ in (5.6), with $\mathbf{g}(t) = Q(t)/A(t) \cdot \mathbf{n}$ and $|g| = V_{maxECD}/2$, where V_{maxECD} is the fluid peak velocity measured from ECD.

Absorbing boundary conditions. In hemodynamic problems pressure waves travel along the arterial system (see [106, 107, 108, 109]). The imposition of a suitable outflow boundary condition, which does not induce spurious reflections (these effects happen when free stress or non physiological stress are applied), is a major issue in this kind of applications. In order to avoid the phenomenon of spurious reflections, it is possible to follow



(a) The red line represents the eco-color-doppler estimated velocity.



(b) The eco-color-doppler estimated flow rate.

Figure 5.3: From the eco-color-doppler image to the patient-specific flow rate.

the geometrical multiscale approach [107], where we prescribe a suitable absorbing boundary condition by coupling the 3D compliant model with a 1D reduced model. Indeed, in [107], the authors considered a cylinder of radius R , length L and with S the section normal to the axis z of the cylinder and wrote an hyperbolic system that allows to capture propagative phenomena along the axis of the cylinder. Then, they assumed that one of the characteristic variables of the system was zero at an outflow Σ (for details see [110]) and, considering the *resistance absorbing boundary conditions*, they calculated the following *defective resistance boundary condition* in the normal direction [111]

$$\frac{1}{|\Sigma|} \int_{\Sigma} (\mathbf{T}_f \mathbf{n}) \cdot \mathbf{n} d\sigma - R_e \int_{\Sigma} \mathbf{u} \cdot \mathbf{n} d\sigma = P_e, \quad \text{on } \Sigma, \quad (5.7)$$

where the *resistance* R_e is a constant and is given by

$$R_e = \sqrt{\frac{\rho_f \tau^0}{2\sqrt{\pi}}} \frac{1}{A_0^{3/4}}, \quad (5.8)$$

and P_e is the external pressure. In the expression of R_e , A_0 is the area of the surface S at $t = 0$ and τ^0 comes from the following

$$\tau = \frac{EH_s \sqrt{\pi}}{(1 - \nu^2)R^2}, \quad (5.9)$$

when (5.9) is calculated with A_0 , and H_s is the vessel thickness, E is the Young modulus, ν the Poisson modulus.

Let us remark that the proposed resistance boundary condition in the normal direction has to be completed with a condition in the tangential direction $\boldsymbol{\tau}$, e.g.

$$(\mathbf{T}_f \mathbf{n}) \cdot \boldsymbol{\tau} = 0, \quad \text{on } \Sigma.$$

Robin condition for the surrounding tissue. Vessels are constrained radially by the surrounding tissue. A common hypothesis about the surrounding tissue is that it takes up a considerable portion of the intravascular pressure and significantly reduces the wall strain and stress. From the analysis reported in [86], the radial constraint of the surrounding tissue was quantified as an effective perivascular pressure on the outer surface of the vessel, which was estimated as 50% or more of the intravascular pressure. For carotid arteries at pressure of 100 mmHg, the circumferential wall stretch ratio in the intact state was $\approx 20\%$ lower than in the untethered state, and the average circumferential stress was reduced by $\approx 70\%$. We use a 0D model to describe the presence of a surrounding tissue around the vessel as shown in fig.5.4. In particular, we prescribe the following Robin boundary condition on Σ_{out} (see

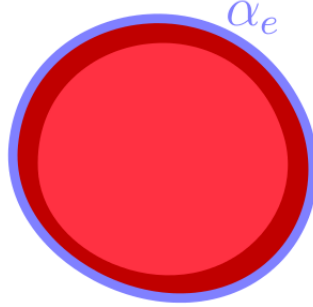


Figure 5.4: Section of the FSI domain. The blue line represents the surrounding tissue, the dark red line describes the vessel wall and the red area indicates the vessel lumen.

[112, 67, 113])

$$\alpha_e \hat{\boldsymbol{\eta}}_s + \mathbf{P}(\hat{\boldsymbol{\eta}}_s) \hat{\mathbf{n}} = P_{ext} \hat{\mathbf{n}}. \quad (5.10)$$

where α_e (in [$dyne/cm^3$]) is the elastic coefficient used to describe an elastic behaviour of the surrounding tissue [67, 86].

5.3 Partitioned algorithms for the numerical solution of the FSI problem

We are here interested in *partitioned algorithms* for the numerical solution of the FSI problem (5.4), which consist in the successive solution of the three subproblems (the fluid, the structure and the fluid domain problems) in an iterative framework [114, 115, 116, 103, 117, 118]. The main difficulties related to the numerical solution of a FSI problem are the following:

1. the fluid computational domain is an unknown of the problem and we have to enforce the continuity of displacements at the fluid-structure (FS) interface (*geometrical interface condition*);
2. the fluid and the structure subproblems are both non-linear (*constitutive non-linearities*);
3. we have to guarantee the continuity of velocities and normal stresses at the fluid-structure interface (*physical interface condition*).

The geometrical interface condition can be managed following two different strategies. The first strategy consists in an *exact treatment* of the interface position, in which the geometrical interface condition is satisfied exactly (*geometrical exact schemes*), through, for example, fixed point or Newton iterations (see, e.g., [119, 120]). The second strategy consists in an *inexact treatment* of the interface position, in which this condition is not satisfied, due to an explicit treatment of the interface position by extrapolation from previous time steps (the so-called *semi-implicit schemes*, e.g., [102, 121, 110]), or, in general, to an a priori fixing of the number of iterations over the interface position [113] (*geometrical inexact schemes*). However, in the haemodynamic context, when dealing with three-dimensional real geometries and physiological data, it is still not clear which treatment of the fluid-structure interface is appropriate for practical purposes. Recently, in [113] it has been shown that general geometrical inexact schemes, obtained by performing just few iterations over the interface position, are effective in haemodynamics in the case of the linear infinitesimal elasticity, providing the expected time convergence rate when high order temporal schemes are considered and accurate solutions when dealing with three-dimensional real geometries and physiological data, and being very efficient from the computational point of view.

The second difficulty is represented by the fluid and the structure constitutive non-linearities. In haemodynamics, for the case of the linear infinitesimal elasticity, the first one (due to the convective term in the Navier-Stokes equations) have been typically treated together with the geometrical interface condition, so that we can identify also for this non-linearity an *exact* and an *inexact treatment*. In [112], another treatment has been discussed, where the convective term has been treated differently from the geometrical interface condition. When also the structure constitutive non-linearity is present, different treatments have been considered, as those derived from the application of the Newton method to the interface problem [120, 122] and those obtained by the application of suitable linearization of the monolithic system. Regarding the last strategy, some authors stressed the modularity of the related algorithms, leading to *partitioned schemes*. A first approach of this type (holding for a geometrical exact or inexact scheme) consists in solving the non-linear fluid and structure subproblems in an iterative framework until convergence of the physical interface conditions (see for example the classical Dirichlet-Neumann scheme). At each iteration two non-linear subproblems have to be solved [123, 124, 125, 126]. In this case, the constitutive non-linearities are treated in an inner loop with respect to both the physical and the geometrical interface conditions. A second strategy considered so far consists in applying the quasi-Newton method to the monolithic non-linear system. In [119], the author proposed a block-diagonal approximation of the Jacobian, relying to a partitioned algorithm

where all the interface conditions and non-linearities are treated in the same loop (see also [127, 126, 128, 129, 130]). In [113], the authors considered new different approximations of the Jacobian, leading to different, most efficient partitioned algorithms. Such schemes are *Double-loop* schemes, where there is an external loop to manage the geometrical interface condition and the constitutive non-linearities and an internal one to prescribe the physical interface conditions.

Concerning the physical interface condition, after a suitable linearization of the constitutive and geometrical non-linearities - whichever of the two strategies is adopted for the treatment of the interface position (implicit or explicit) - one has to deal with a linearized FSI problem. However, this problem is still coupled through the interface continuity conditions. Up to now, two strategies have been proposed namely the *monolithic* and the *partitioned approaches*. In the first case, the problem is solved by building the whole FSI matrix, and then by solving the related linear system with a suitable preconditioned Krylov [119, 100], domain-decomposition [112] or multigrid [131, 132] method. Obviously, in this way the interface continuity conditions are automatically satisfied. Alternatively, in partitioned schemes one solves the fluid and structure subproblems in an iterative framework, until fulfillment of the interface continuity conditions. It has been clearly highlighted in several works that the physical conditions have to be treated implicitly in haemodynamics, due to the high added-mass effect characterizing this case (see, e.g., [133, 116, 115, 103, 114]).

Robin-Robin partitioned procedures. We are focusing on partitioned algorithms that involve the solution of separate fluid and structure problems through the exchange of suitable transmission conditions at the FS interface Σ . At convergence, they guarantee the continuity of the velocity and the normal stress at Σ .

To solve system (5.4) we have to take into account the *added-mass effect*, that is present when the fluid and the structure densities are of the same order or when the domain is very slender. Indeed, if we use the classical *Dirichlet-Neumann (DN)* scheme, which consists in solving iteratively the fluid problem with the structure velocity as Dirichlet condition at the FS interface, and the structure problem with the fluid interface normal stress as Neumann condition at the same interface, the convergence properties of this scheme deteriorate due to the added-mass effect. It has been shown in [115, 133, 134] that in presence of a large added-mass effect, DN algorithm needs a strong relaxation and features a very slow convergence. Two straightforward alternatives proposed for haemodynamic problems are the *Neumann-Dirichlet (ND)* and the *Neumann-Neumann (NN)* schemes. However, the former has even worse numerical properties than DN and the latter do not improve substantially the results obtained with DN scheme [116].

We consider now a linear combination of the interface continuity of velocities and normal stresses, i.e. (5.4)₄₋₅, that leads to a set of Robin-type transmission conditions [103]. Introducing two suitable coefficients, α_f and α_s , with $\alpha_f \neq \alpha_s$, we can write

$$\begin{cases} \alpha_f \mathbf{u}_f^{n+1} + \mathbf{T}_f(\mathbf{u}_f^{n+1}, p_f^{n+1})\mathbf{n} = \alpha_f \mathbf{u}_s^{n+1} + \mathbf{T}_s(\boldsymbol{\eta}_s^{n+1})\mathbf{n}, & \text{on } \widehat{\Sigma}^{n+1}, \\ \alpha_s \mathbf{u}_s^{n+1} - \mathbf{T}_s(\boldsymbol{\eta}_s^{n+1})\mathbf{n} = \alpha_s \mathbf{u}_f^{n+1} - \mathbf{T}_f(\mathbf{u}_f^{n+1}, p_f^{n+1})\mathbf{n}, & \text{on } \widehat{\Sigma}^{n+1}. \end{cases} \quad (5.11)$$

Using this conditions we introduce a family of partitioned schemes with better convergence properties. The *Robin-Robin (RR)* scheme consists in solving iteratively the fluid subproblem with Robin condition (5.11)₁ at the FS interface, and the structure problem with Robin condition (5.11)₂ at the FS interface. This algorithm generates a family of partitioned procedures. Indeed, the classical DN and ND algorithms can be recovered with $\alpha_f \rightarrow \infty, \alpha_s = 0$ and $\alpha_f = 0, \alpha_s \rightarrow \infty$, respectively. The particular cases of $\alpha_s = 0$ or $\alpha_f = 0$ lead to the *Neumann-Robin* and the *Robin-Neumann* schemes, respectively. Moreover, when $\alpha_f \rightarrow \infty$ or $\alpha_s \rightarrow \infty$ we obtain the *Dirichlet-Robin* and *Robin-Dirichlet* schemes, respectively. RR algorithm has good convergence properties and it is independent of the added-mass effect when the parameters α_f and α_s are suitably chosen, as shown in [103, 135].

Double-loop algorithm To solve the non-linear FSI problem (5.4) we will consider a Double-loop algorithm. The idea is to consider an external loop to manage the geometrical interface condition and the constitutive non-linearities, and an internal loop to treat the physical interface condition with a Robin-Robin scheme.

Let us introduce

- the fluid solver operator \mathcal{F} ;
- the structure solver operator \mathcal{S} ;
- the fluid domain operator \mathcal{H} .

Using the above operators the Double-loop scheme reads as follows

External loop. *Given the solution at iteration k , solve at the current iteration $k+1$ until convergence*

1. The harmonic extension

$$\begin{cases} \mathcal{H}(\widehat{\boldsymbol{\eta}}_m^{k+1}) = \mathbf{0} & \text{in } \widehat{\Omega}_f, \\ \widehat{\boldsymbol{\eta}}_m^{k+1} = \widehat{\boldsymbol{\eta}}_s^{k+1} & \text{on } \widehat{\Sigma}, \end{cases}$$

obtaining the fluid domain velocity $\widehat{\mathbf{u}}_m$ and the new fluid domain Ω_f .

2. The linearized FSI problem in a known domain. For its solution, we consider the following RR partitioned algorithm

Internal loop n iterations. *Given the solution at subiteration $l - 1$, solve at the current subiteration l until convergence or until $l \leq n$*

- (a) The fluid subproblem with a Robin condition at the FS interface

$$\begin{cases} \mathcal{F}(\mathbf{u}_{f,l}^{k+1}, p_{f,l}^{k+1}, \mathbf{u}_m^{k+1}) = \mathbf{f}_f^{k+1}, & \text{in } \Omega_f^{k+1}, \\ \alpha_f \mathbf{u}_{f,l}^{k+1} + \mathbf{T}_f(\mathbf{u}_{f,l}^{k+1}, p_{f,l}^{k+1})\mathbf{n} = \alpha_f \mathbf{u}_{s,l-1}^{k+1} + \mathbf{T}_s(\boldsymbol{\eta}_{s,l-1}^{k+1})\mathbf{n}, & \text{on } \widehat{\Sigma}^{k+1}, \end{cases}$$

(b) The structure subproblem with a Robin condition at the FS interface

$$\begin{cases} \mathcal{S}(\widehat{\boldsymbol{\eta}}_{s,l}^{k+1}) = \widehat{\mathbf{f}}_s & \text{in } \widehat{\Omega}_s, \\ \alpha_s \mathbf{u}_{s,l}^{k+1} - \mathbf{T}_s(\boldsymbol{\eta}_{s,l}^{k+1})\mathbf{n} = \alpha_s \mathbf{u}_{f,l}^{k+1} - \mathbf{T}_f(\mathbf{u}_{f,l}^{k+1}, p_{f,l}^{k+1})\mathbf{n}, & \text{on } \widehat{\Sigma}^{k+1}. \end{cases}$$

Chapter 6

Haemodynamic results

In this chapter we first introduce the carotid artery stenosis pathology. Then we describe the numerical simulations performed on a patient-specific carotid by using the C++ parallel finite element library LifeV [22]. Our aim is to compare FSI results on inflated and deflated patient-specific carotid, showing differences in the displacement, velocity, pressure field, and in the wall shear stress (WSS) haemodynamic factor.

6.1 Carotid artery stenosis

Several factors play a role in the development of the carotid artery stenosis. Non modifiable risk factors include age, race, sex, genetic, and family history and modifiable ones include smoking, hyperlipidemia, sedentary lifestyle, increased body mass index, alcohol and substance abuse, diabetes mellitus, hypertension, prior transient ischemic attack or stroke, elevated anticardiolipin antibodies, presence of a carotid bruit, cardiac disease and increased fibrinogen. The geometry of the carotid bifurcation itself can be considered a risk factor. Indeed, the unique geometry of the carotid bifurcation governs the local haemodynamics, which is implicated in carotid artery wall heterogeneity. Most people with carotid stenosis have no symptoms until the artery becomes severely narrowed or a clot forms. Symptoms are most likely to first appear with a mini-stroke, also known as a transient ischemic attack. Carotid stenosis is a progressive narrowing of the carotid arteries in a process called *atherosclerosis*. Normal healthy arteries are flexible and have smooth inner walls. With age, hypertension and small injuries to the blood vessel wall can allow *plaque formation*. Plaque is a sticky substance made of fat, cholesterol, calcium and other fibrous material. Over time, plaque deposits inside the inner wall of the artery can form a large mass that narrows the lumen, the inside diameter of the artery (see fig.6.1).

Several study have shown that carotid arterial stenosis occur where the common carotid artery (CCA) bifurcates into the internal carotid artery (ICA) and external carotid artery (ECA) (see fig.6.2).

The carotid bulb, or sinus, appears to host a unique blood flow environment and is thought to play a role in local blood flow disturbances that lead to endothelial cell damage



Figure 6.1: A carotid plaque.

and subsequent plaque formation. After impinging on the carina of the bifurcation, blood flow is redirected downstream into the carotid branches. Due to tight turn, the inertial force on the flowing blood precludes it from following the outer curvature of the carotid sinus and flow separates, creating local flow disturbances. The proximal segment of ICA, where flow is *separated*, is the most common site for the development of the plaque. There are different types of carotid plaques. In particular the surgeons distinguish in *homogeneous* and *heterogeneous plaques*. In general, homogeneous plaques are stable, with deposition of fatty streaks and fibrous tissues. Artherosclerotic changes include diffuse intimal thickening that results from the migration of medial smooth muscles cells into the subendothelial space through the fenestration into the intimal elastic lamina. Intimal growth includes increasing amounts of the elastic fibres, collagen, and glycosaminoglycans. These plaques rarely have evidence of hemorrhage or ulcerations. As the atherosclerotic plaque develops, the elicited biologic response is an attempt to cover the plaque with a fibrous cap, as depicted in fig.6.3. Unfortunately, over time the fibrous cap may rupture and release the underlying debris into the circulation. Restabilization of the ruptured plaque includes a normal cascade of wound healing responses leading to heterogeneous structure. Heterogeneous plaques are unstable, with histological characteristics of lipid-laden macrophages, monocytes, leukocytes, necrotic debris, cholesterol crystals, and calcifications. These plaques are soft and friable but may harden with calcium, lipid, and cholesterol accumulation within the vessel wall. Surface irregularities or plaque ulceration have also been shown to be risk factors for thromboembolic events. *Ulcerated plaques* consist of soft, gelatinous clots that contain platelets, fibrin, white blood cells, and red blood cells. The complicated plaque may undergo rupture, intraplaque hemorrhage, extensive necrosis, calcification, and subsequent *thrombosis*. Infiltration of the



Figure 6.2: Eco-color-doppler scan of plaque formation at internal carotid artery (ICA).

fibrous cap by foam cells may also contribute to the *rupture*. Extensive studies of plaque characteristics have revealed a correlation between the histologic features of a plaque and its susceptibility to cause thromboembolic events. In general, symptomatic carotid disease is not a result of inadequate perfusion due to a high degree of stenosis, rather, patients with symptomatic carotid disease usually have heterogeneous plaques that are the source of shed emboli. The degree of carotid artery stenosis alone may not enable an adequate prediction of which patients will suffer strokes.

Plaque characteristics have been studied not only to elucidate the cause of the disease but also in an effort to correlate them with either intravascular or perivascular findings at ultrasonography (US). However, effort is directed also toward the development of less-invasive characterization techniques, such as magnetic resonance (MR) imaging. Soft heterogeneous plaques that are more likely to be related to stroke usually have low echogenicity at US. This corresponds to the weak reflection of ultrasound and the echolucency of the lipid and hemorrhage content of the plaque [136, 137].

The hypothesis that blood flow patterns at the carotid bifurcation have a substantial bearing on the predilection of this region to atherosclerosis has led to a comprehensive investigation into the associated hemodynamics [138, 139]. Many factors, such as *blood flow velocity*, *mural tensile stress*, *turbulence*, and *arterial wall shear stress (WSS)* have been proposed as causative factors in the initiation of atheroma. WSS in particular has been explored and consequently implicated as an atherogenic factor by many investigators [140, 141, 142]. Initial hypotheses involving WSS contended that atheroma formation at sites with low wall shear is due to a decreased efflux of cholesterol [12]. Other studies [142] have suggested that

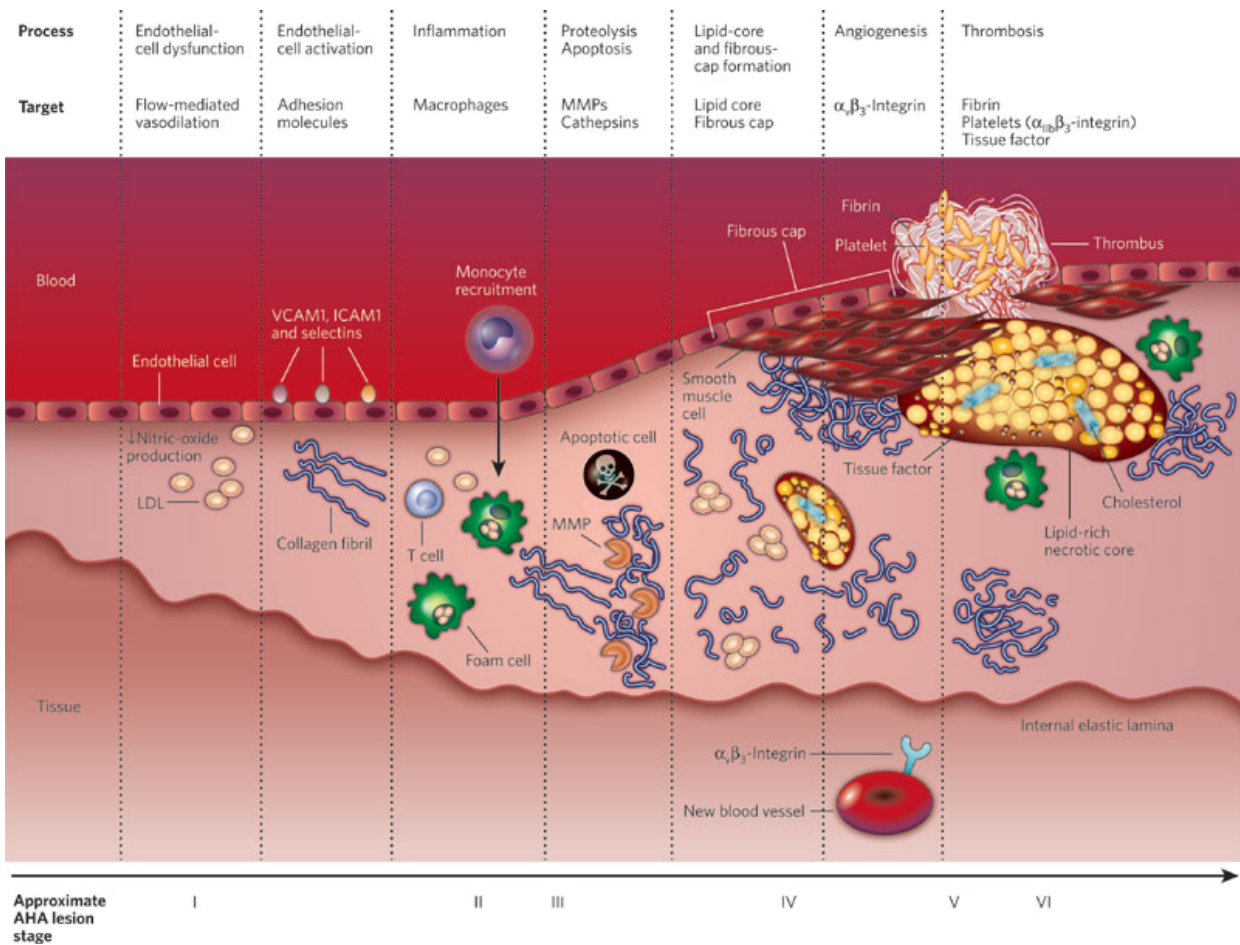


Figure 6.3: Plaque formation process.

atheroma formation occurs at sites with high WSS due to damage caused to the endothelium. Vascular zones susceptible to plaque formation have been found to experience a combination of low and oscillating shear stresses, whereas zones with high wall shear are relatively free of disease [138, 141, 143]. A comparison of WSS distribution in vitro in carotid bifurcation models and the distribution of intimal plaque thickness obtained at autopsy showed minimal plaque formation at the flow divider wall of the sinus (region of high shear), greater intimal thickening at sinus side walls (region with circumferential velocity components, intermediate oscillatory shear), and maximal thickening at the outer walls (region of flow separation, flow reversal, low and oscillating shear) [140, 144]. Strong correlations were found between intimal thickening and the reciprocals of maximum wall shear and mean wall shear and between intimal thickening and oscillating shear index [140].

WSS parameter With regard to vessel bifurcations, such as the carotid arteries shown in this chapter, we know that atherosclerosis affects in particular regions of the external wall immediately after the bifurcation [145, 146]. In these areas, WSS acting on the endothelial

cell surface [147], is weaker than other regions of the vessel. Two areas of WSS values have been identified, that appear to induce opposite effects on the arterial wall:

- $WSS > 15 \text{ dyne/cm}^2$ induces endothelial quiescence and an atheroprotective gene expression profile;
- $WSS < 4 \text{ dyne/cm}^2$ is prevalent at atherosclerosis-prone sites, stimulates an atherogenic phenotype.

It is also possible to demonstrate the correlation between arteriovenous malformations in cerebral arteries and WSS [148]. Hence, a proper evaluation of this hemodynamic parameter can then provide relevant clinical data for a correct treatment of arteriosclerosis and correlated pathologies in arteries.

The WSS index represents the surface stress on the wall induced by fluid dynamic field:

$$\begin{aligned} \widetilde{WSS} &= -\mu[(\nabla u_x \cdot \mathbf{n}_\Sigma)\mathbf{e}_x + (\nabla u_y \cdot \mathbf{n}_\Sigma)\mathbf{e}_y + (\nabla u_z \cdot \mathbf{n}_\Sigma)\mathbf{e}_z], \\ WSS &= \widetilde{WSS} - (\widetilde{WSS} \cdot \mathbf{n}_\Sigma)\mathbf{n}_\Sigma, \end{aligned} \tag{6.1}$$

where u_x, u_y, u_z are the velocity components in cartesian coordinates, \mathbf{n}_Σ is the normal vector with respect to the interface and $\mathbf{e}_x, \mathbf{e}_y, \mathbf{e}_z$ are the cartesian versors.

In the fig.6.4, it is possible to see typical values on WSS for carotids, and in the table 6.1, it is shown the WSS range for healthy and pathological arteries.

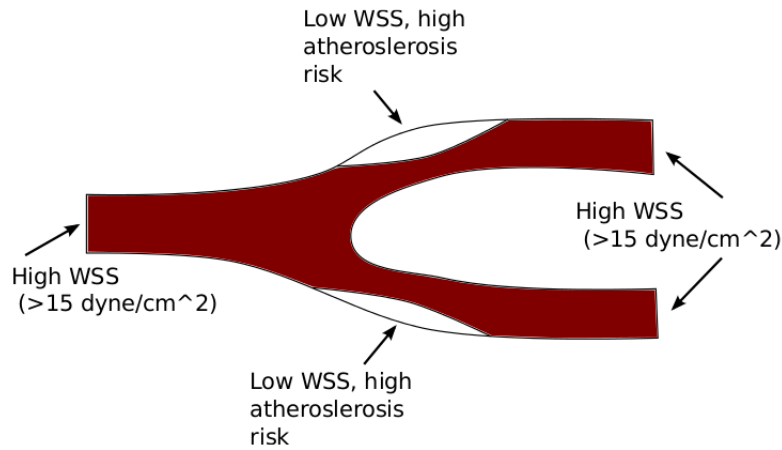


Figure 6.4: Typical values of WSS for carotids. Taken from [147]

Table 6.1: WSS range for healthy and pathological arteries.

	Healthy artery	Atherosclerosis	Thrombosis
WSS range [dyne/cm^2]	$10 \div 17$	$-4 \div 4$	$70 \div \geq 100$

6.2 Numerical results

In this section, we apply the numerical methods described in chapter 5 to solve the FSI problem in a patient-specific human carotid artery geometry. In particular, we build the 3D geometry starting by magnetic resonance angiography (MRA) image and using the Vascular Modeling Toolkit (VMTK) open source program [85]. In fig.6.5, we show an MRA image of healthy left and right carotids.

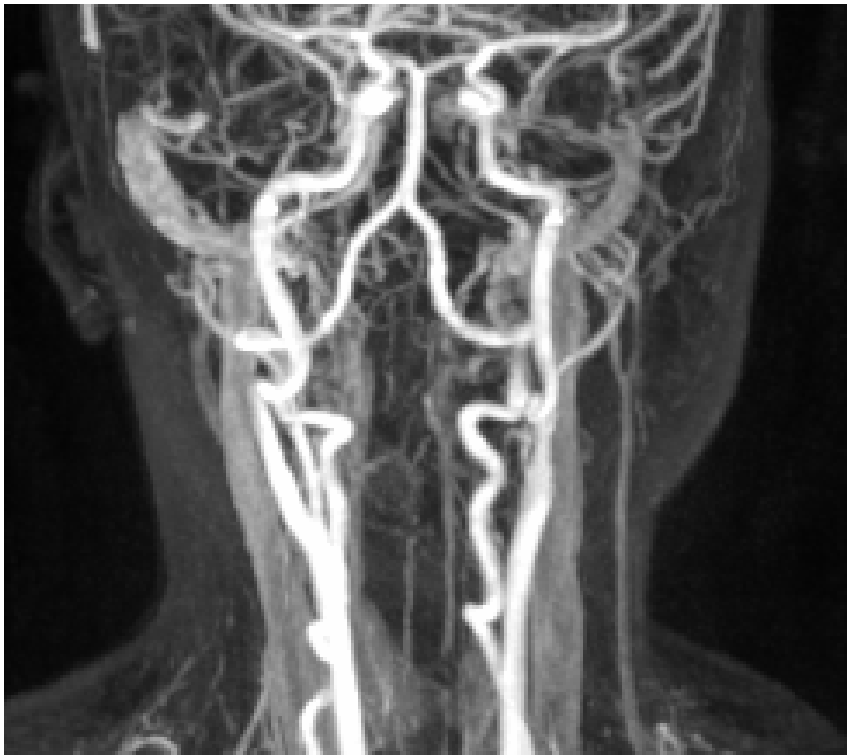


Figure 6.5: A MRA image of left and right carotids.

However, these images could provide just information concerning the interface between the lumen and the vessel. Therefore, just the fluid computational domain could be generated and no information about the vessel are provided. To overcome this limitation and obtain the vessel computational domain, in this work we decided to extrude the lateral surface of the fluid domain in the normal direction. The extrusion is proportional to 24% of the lumen radius.

We performed two FSI simulations, the first with the inflated carotid geometry reconstructed from radiological images and the second with the calculated deflated carotid geometry (see chapter 3). In both numerical simulations, we consider the compressible *St. Venant-Kirchhoff*

6.2. Numerical results

material, whose first Piola-Kirchhoff tensor is defined in (2.42), here reported:

$$\mathbf{P} = \frac{\lambda}{2}(I_1(\mathbf{C}) - 3)\mathbf{F} - \mu\mathbf{F} + \mu\mathbf{F}\mathbf{C}$$

The finite element discretization is performed by *P1bubble* – *P1* elements. The set of structural and fluid parameters used in the simulations are listed in table 6.2 and are typical values for biological tissues [13, 28, 38, 39].

Table 6.2: Set of structural and fluid parameters for the inflated and deflated geometries.

$\rho_s[g/cm^3]$	$E[dyne/cm^2]$	ν	$\kappa[dyne/cm^2]$	$\alpha[dyne/cm^2]$	γ	$\rho_f[g/cm^3]$	$\mu_f[poise]$
1.1	3.0e6	0.49	1.0e7	1.034e6	1	1.0	0.03

The inflated geometry. The inflated geometry is directly reconstructed from MRI or CT scans. The mesh properties are showed in table 6.3 and in fig.6.6 we show the inflated solid mesh.

Table 6.3: Inflated geometry mesh properties.

	Nodes	Tetrahedra	Triangles
Inflated solid mesh	9732	43362	9936
Inflated fluid mesh	6913	34581	5238

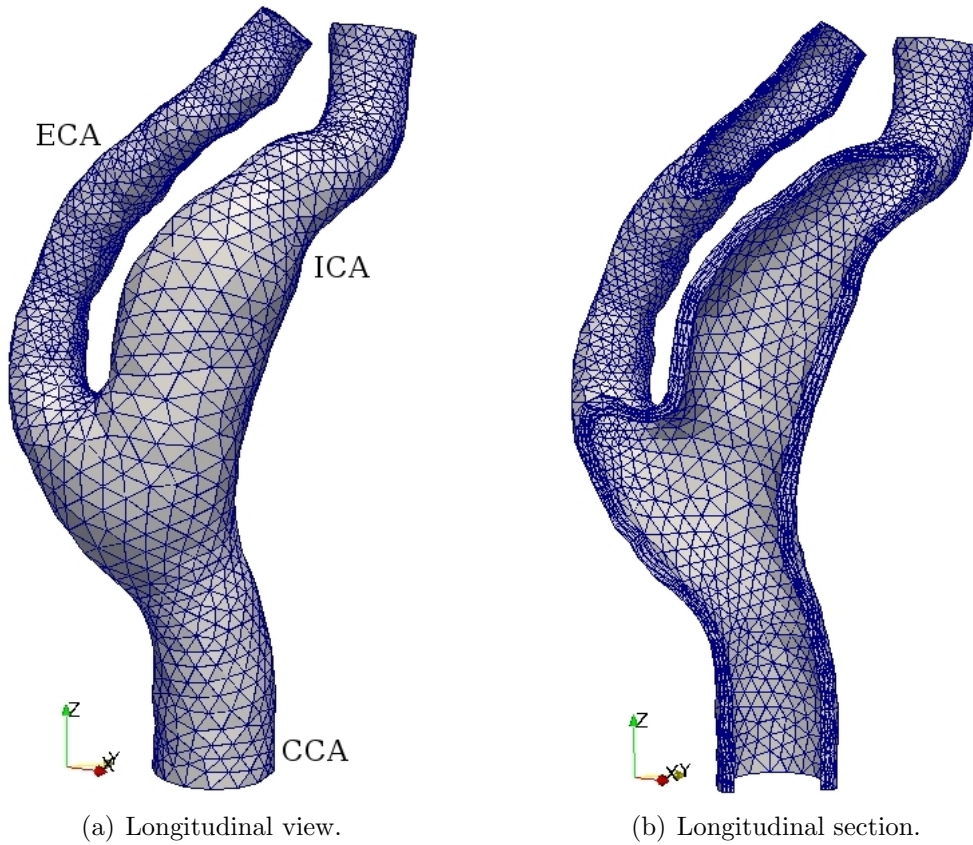


Figure 6.6: The inflated solid mesh. CCA stands for Common Carotid Artery, ECA for External Carotid Artery, and ICA for Internal Carotid Artery.

The deflated geometry. The deflated geometry is calculated applying the algorithm showed in chapter 3 to the inflated geometry. The mesh properties are showed in table 6.4 and in fig.6.7 we show the deflated solid mesh.

Table 6.4: Deflated geometry mesh properties.

	Nodes	Tetrahedra	Triangles
Deflated solid mesh	9732	43362	9936
Deflated fluid mesh	6683	33159	5212

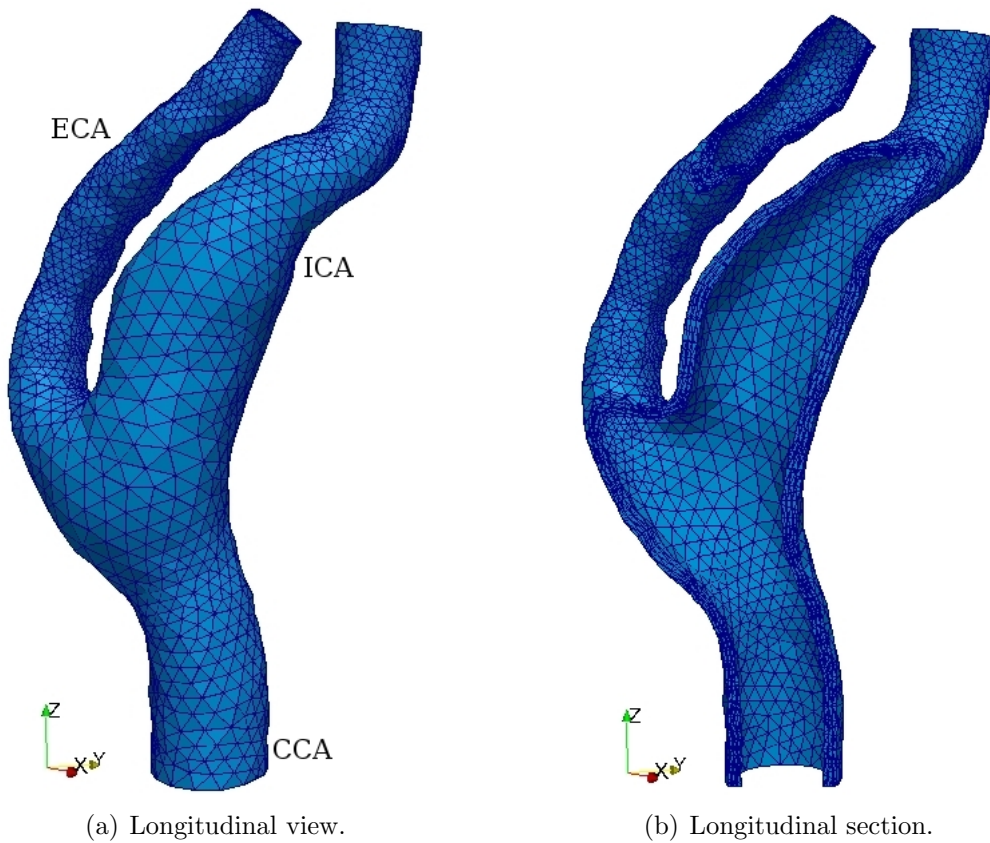


Figure 6.7: The deflated solid mesh. CCA stands for Common Carotid Artery, ECA for External Carotid Artery, and ICA for Internal Carotid Artery.

In fig.6.8 we compare the inflated geometry (in grey) reconstructed from radiological images, and the deflated geometry (in blue) calculated from the inflated one.

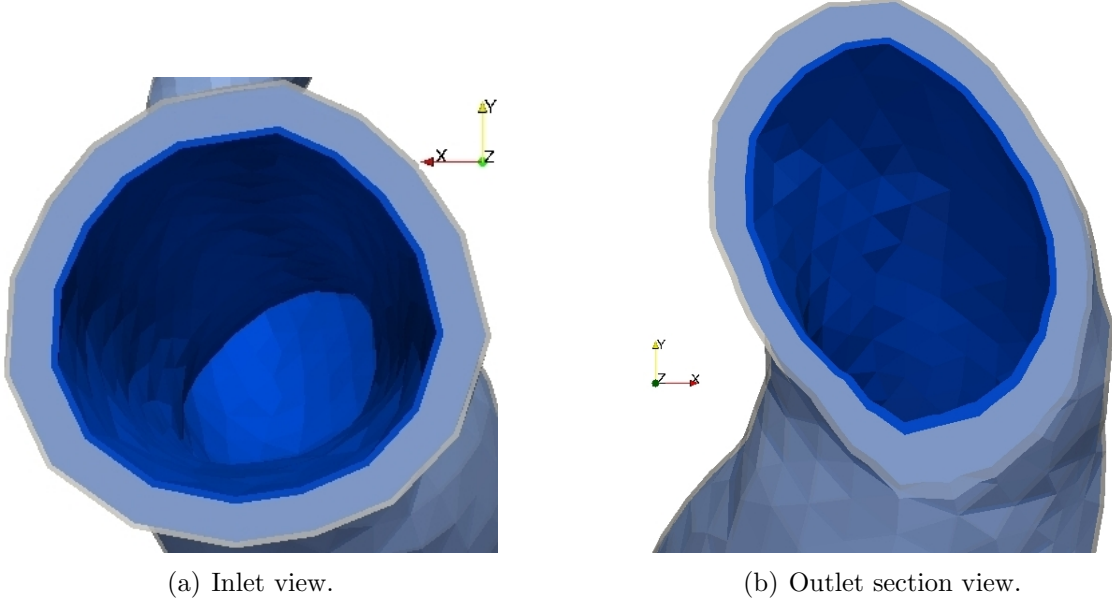


Figure 6.8: Comparison between inflated (in grey) and deflated (in blue) carotid geometries. The deflated geometry shows an inlet radii 9% shorter than the inflated one.

FSI simulation boundary conditions. The boundary conditions we used for the numerical simulations are the following:

- at the inlet we prescribed the flow rate obtained by the eco-color-doppler using the procedure described in section 5.2.2 (see also [104, 105]). In particular, we measured the fluid peak velocity from eco-color-doppler, $V_{max_{ECD}}$, at a distance of 2 cm from the bifurcation;
- at the outlets we imposed a constant resistance condition (see (5.7) and (5.8)) for the fluid;
- the initial conditions $(p_f^0, \hat{\boldsymbol{\eta}}_s^0, \hat{\boldsymbol{\eta}}_m^0, \mathbf{u}_f^0)$ were homogeneous;
- for the solid, at the outlets we imposed homogeneous Dirichlet condition, while at the inlet we imposed homogeneous Dirichlet condition for the normal direction and homogeneous Neumann condition for the tangential direction;
- at the external solid wall we imposed the Robin condition for the surrounding tissue (see (5.10)) with $\alpha_e = 1e6 \text{ dyne/cm}^3$;

- we used Backward Euler/Backward Euler as temporal scheme, with a time step $\Delta t = 0.002 s$ and a final time $T = 0.8$ (a cardiac cycle);
- we ran the simulations on 8 processors for the solution of the fluid and on 1 processor for the solution of the structure.

In fig.6.9,6.10 and 6.11 we report the solid displacement, the velocity and the wall shear stress at systole for both inflated and deflated geometries, while in fig.6.12,6.13 and 6.14 we show the same quantities of interest at diastole. We observe small differences for all the quantities at hand. Indeed, the deflated geometry has only slight lower displacements respect to the inflated one. The recirculation regions next to the bifurcation, at the entrance of the external carotid artery and inside the internal carotid artery, shows small differences between the two geometries. Regarding the WSS values, we observe a more remarkable difference in the area of fluid impingement inside the ICA, see fig.6.15.

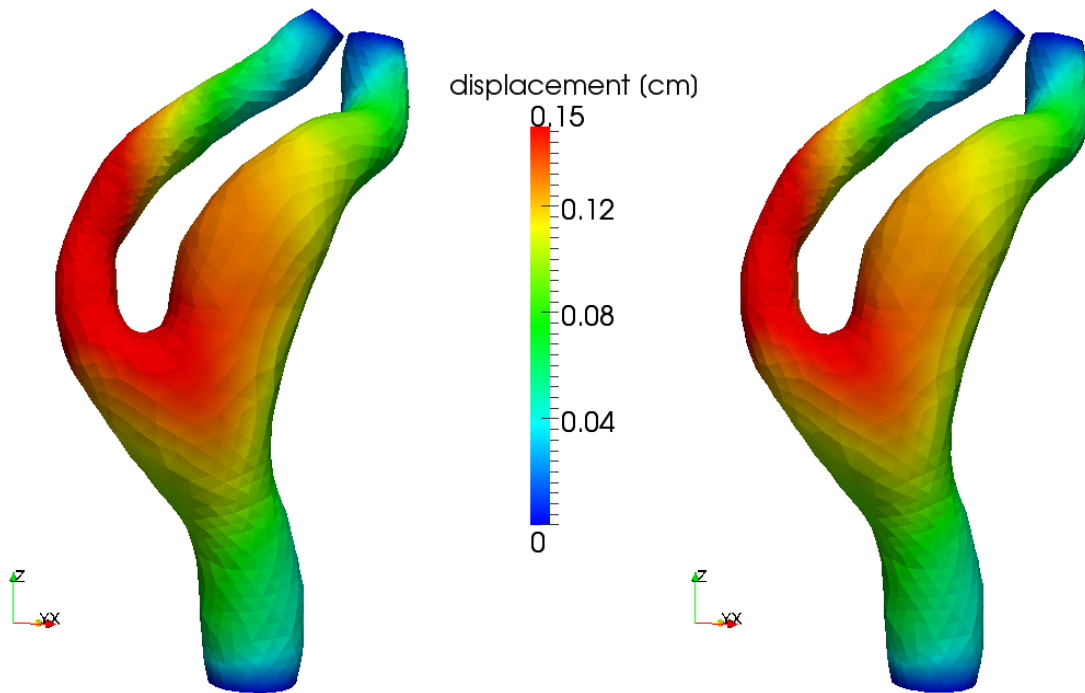


Figure 6.9: Solid displacement [cm] for the inflated (left) and the deflated (right) geometries at systole.

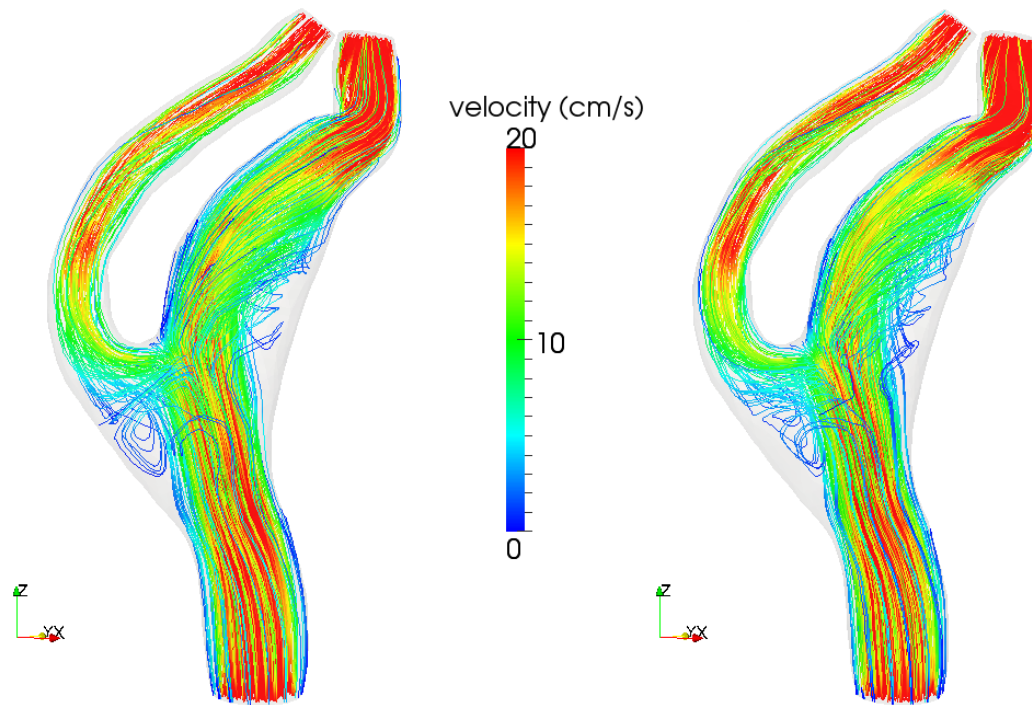


Figure 6.10: Velocity [cm] for the inflated (left) and the deflated (right) geometries at systole.

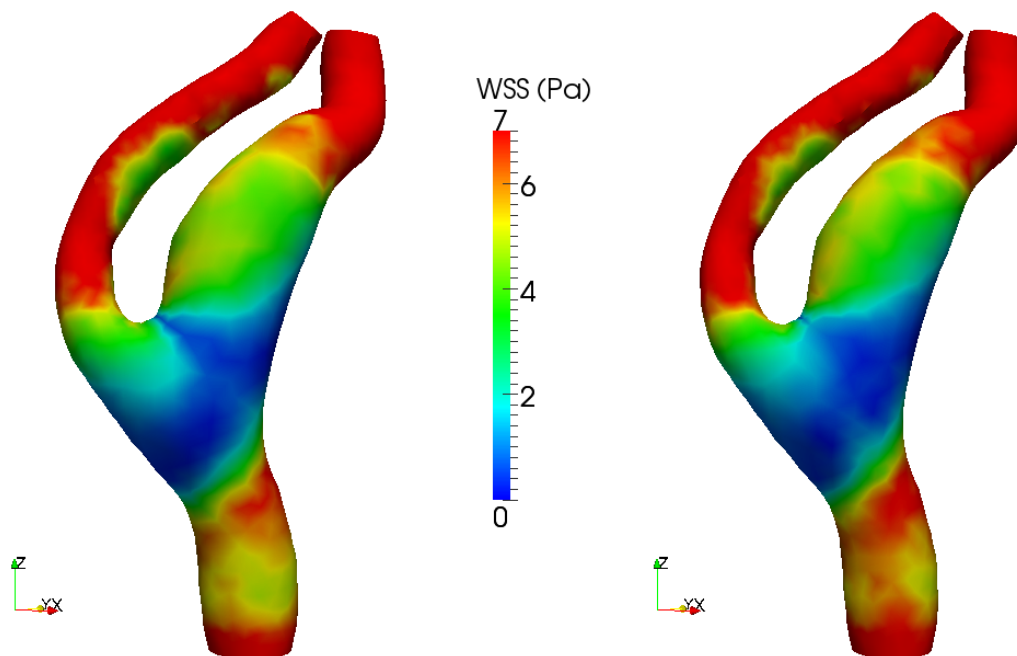


Figure 6.11: Wall shear stress [cm] for the inflated (left) and the deflated (right) geometries at systole.

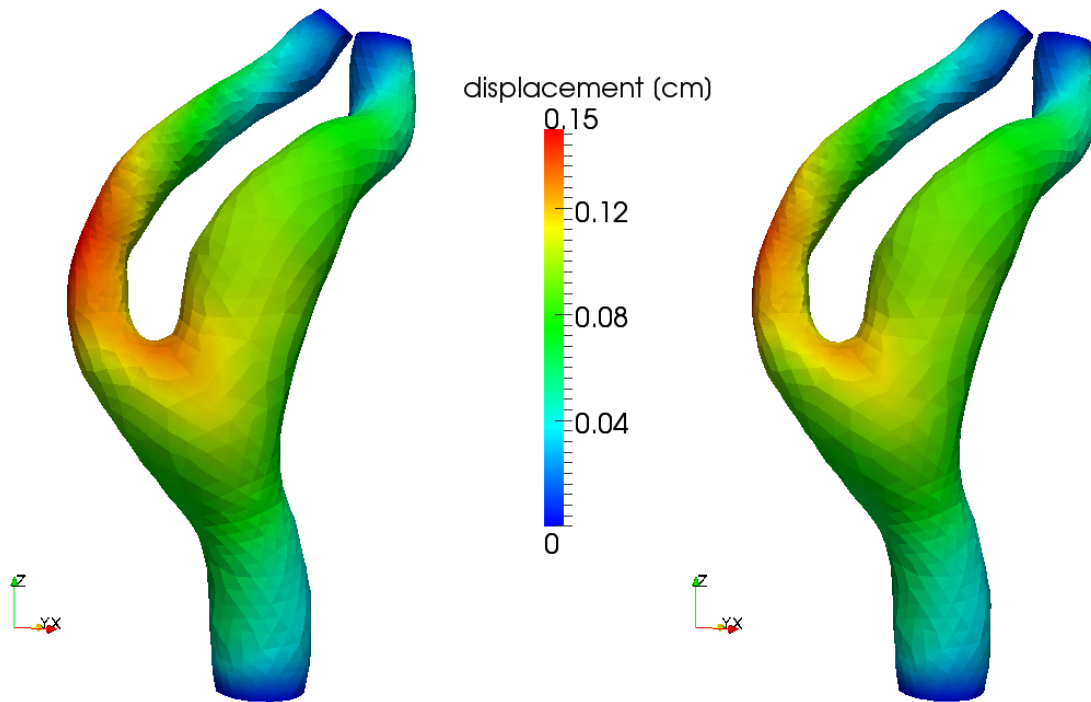


Figure 6.12: Solid displacement [cm] for the inflated (left) and the deflated (right) geometries at diastole.

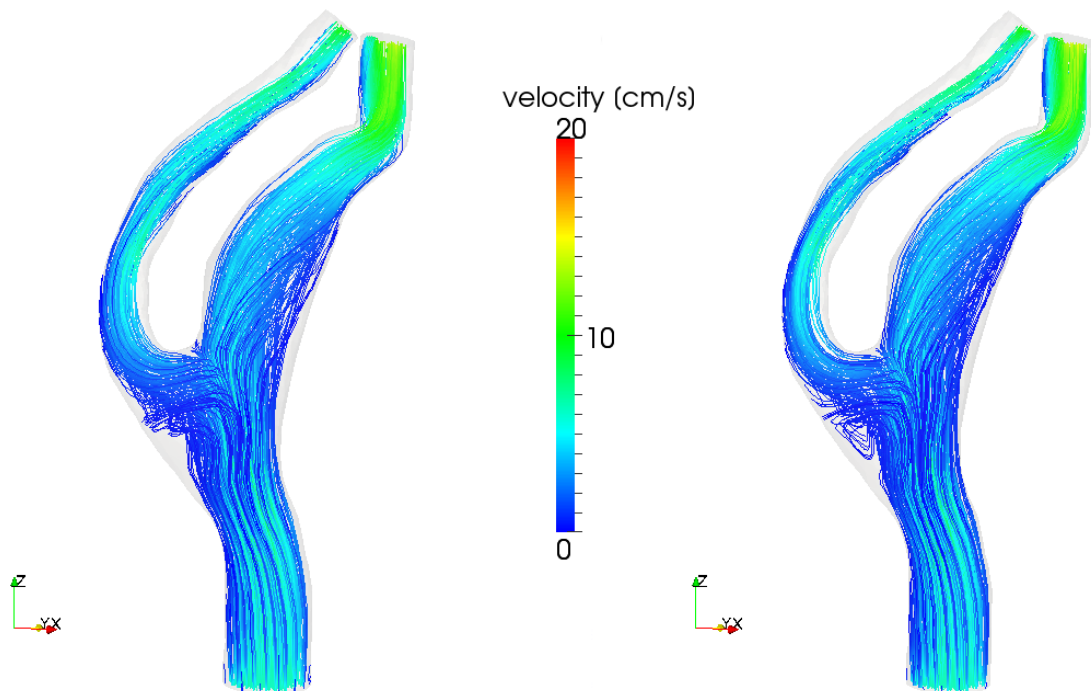


Figure 6.13: Velocity [cm] for the inflated (left) and the deflated (right) geometries at diastole.

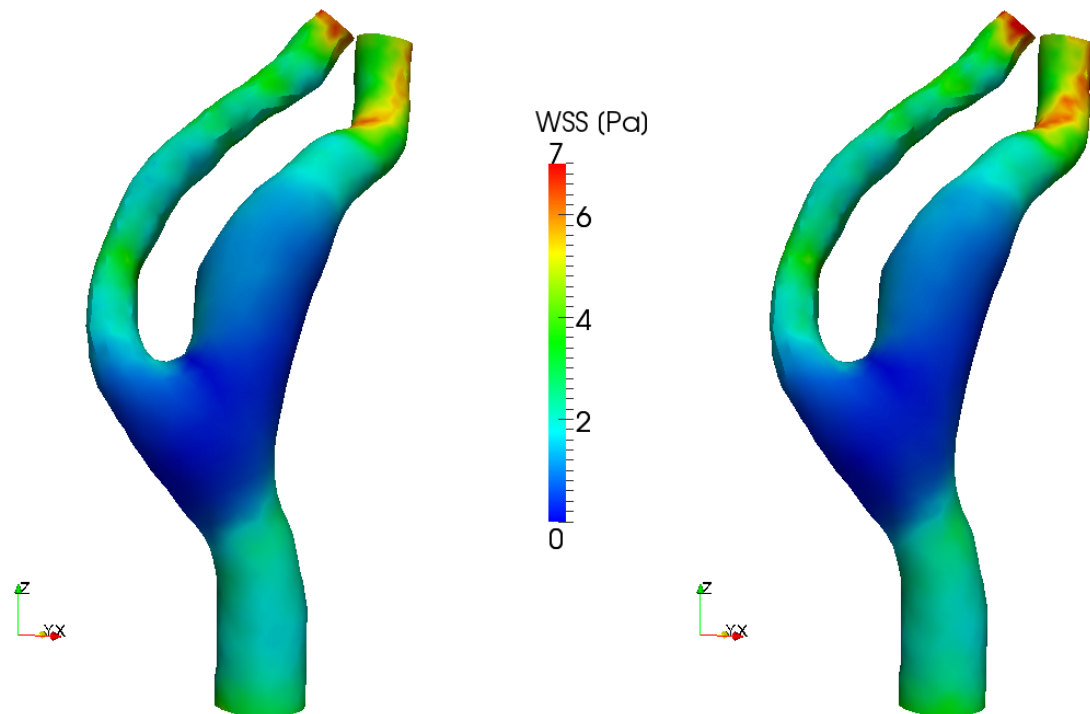


Figure 6.14: Wall shear stress [cm] for the inflated (left) and the deflated (right) geometries at diastole.

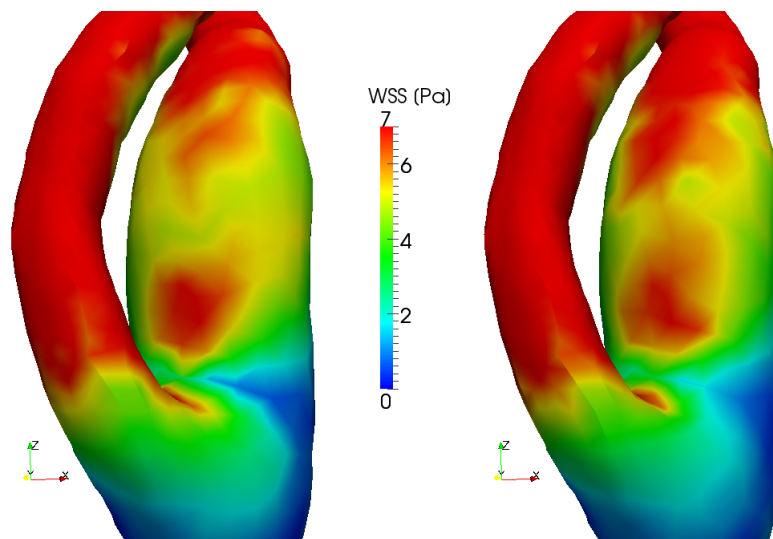


Figure 6.15: Particular of the wall shear stress distribution inside the internal carotid artery, for the inflated (left) and the deflated (right) geometries at systole.

In figures 6.17 and 6.18 we show the variation of flow rate and pressure during the whole cardiac cycle for the inflated and deflated geometries at two different sections (see fig.6.16). We find a smaller flow rate in the case of the deflated geometry (-6%) and a pressure field that is slightly higher (+3%) at systole respect to the inflated geometry one.

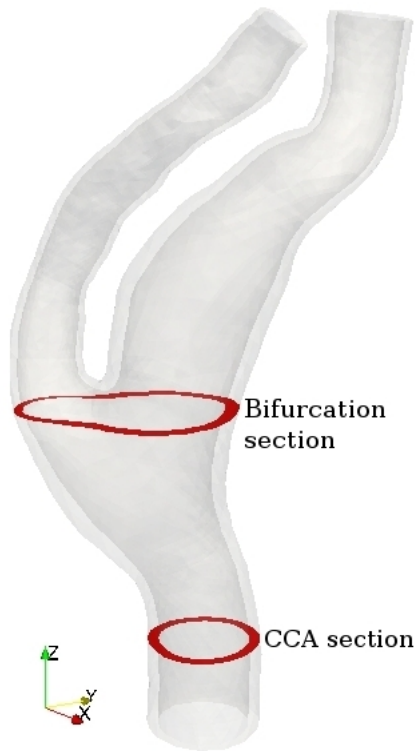
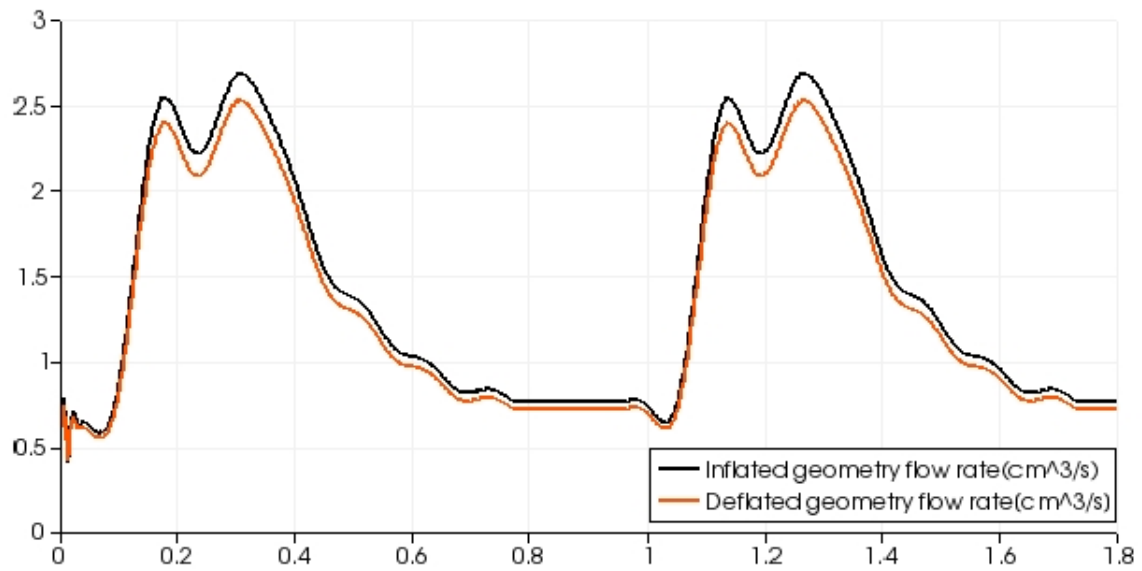
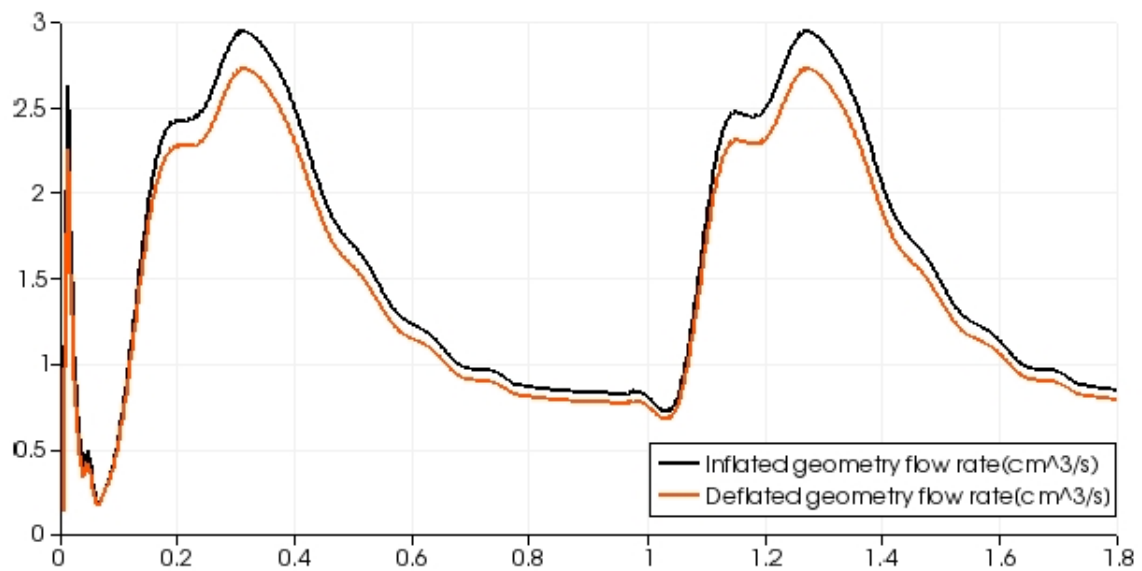


Figure 6.16: The two sections considered to evaluate flow rate and pressure fields in figures 6.17 and 6.18.

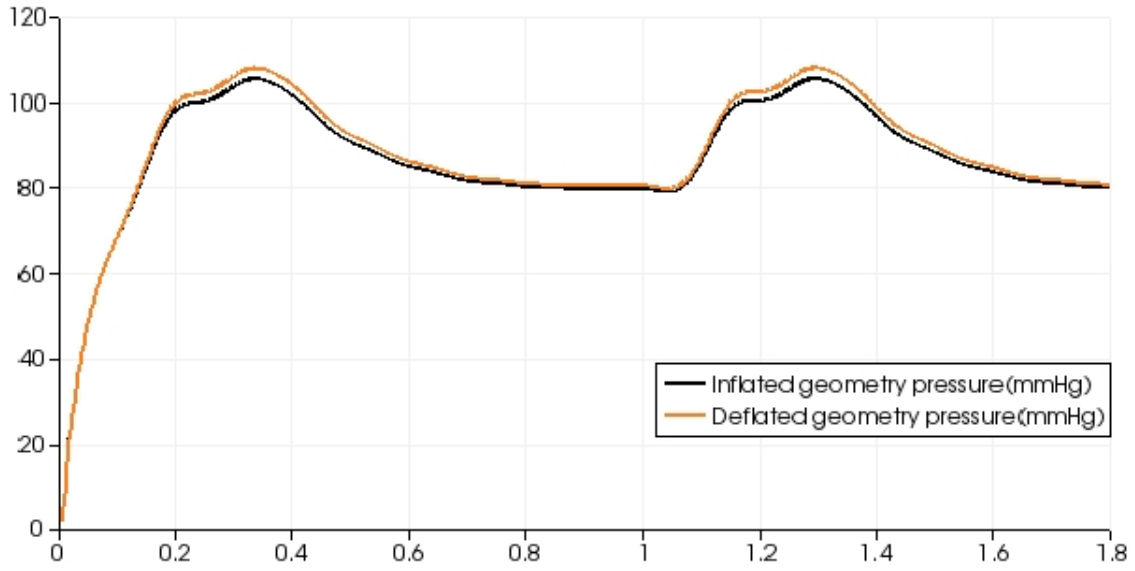


(a) CCA section.

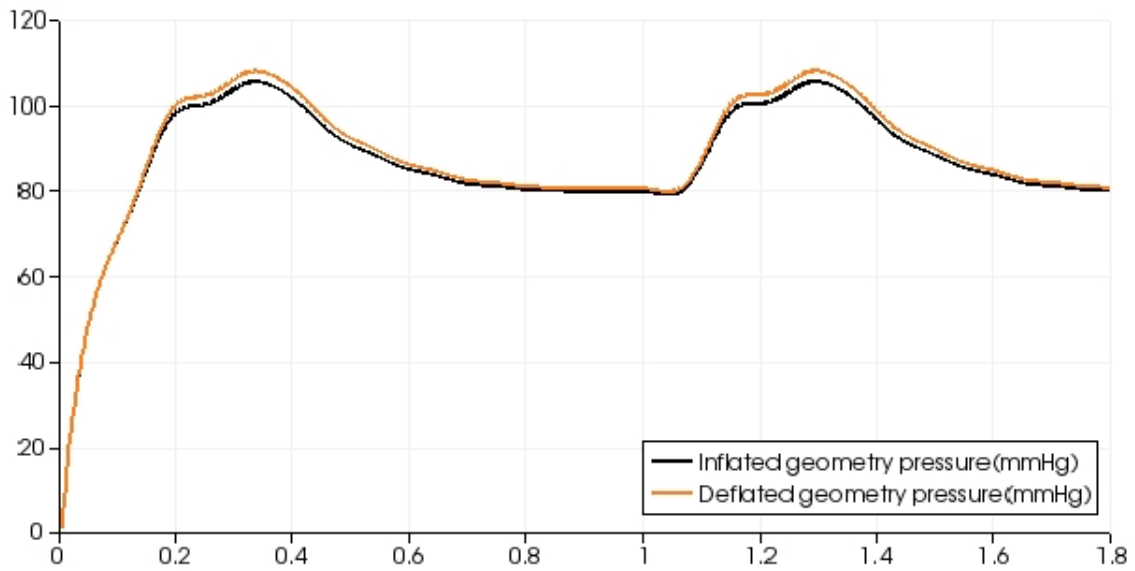


(b) Bifurcation section.

Figure 6.17: Flow rate [cm^3/s] comparison between inflated and deflated geometries at two different sections.



(a) CCA section.



(b) Bifurcation section.

Figure 6.18: Pressure [mmHg] comparison between inflated and deflated geometries at two different sections.

Conclusions

The prestressed state of human arteries is a well-known problem in literature, as we showed in Chapter 3. We chose to simulate this prestress using a deflated geometry, i.e. a 3D reconstructed geometry coming from radiological images (MRI or CT scans) that has been deflated to a 0 mmHg pressure. Then we performed physiological fluid-structure simulations starting from this deflated geometry. Haemodynamic results suggest that the use of correct deflated geometries as initial reference configuration for fluid-structure interaction simulations are required to achieve accurate FSI simulations in haemodynamics because highlighted discrepancies in flux rate and pressure are not neglectable.

Appendix: Functional spaces

In this appendix we recall the main functional spaces used in this work. In particular, to derive the weak formulation of the structural and FSI problems we have used the space L^p and H^q . They belong to the family of Banach spaces where the latter is defined as follows:

Definition .1. A *Banach space* is a normed linear space that is a complete metric space with respect to the metric derived from its norm.

For example, the space \mathbb{R}^n or \mathbb{C}^n equipped with the p -norm defined as:

$$\|(\mathbf{x}_1, \mathbf{x}_2, \dots, \mathbf{x}_n)\|_p = (|\mathbf{x}_1|^p + |\mathbf{x}_2|^p + \dots + |\mathbf{x}_n|^p)^{1/p},$$

for $p < \infty$, and

$$\|(\mathbf{x}_1, \mathbf{x}_2, \dots, \mathbf{x}_n)\|_\infty = \max\{|\mathbf{x}_1|, |\mathbf{x}_2|, \dots, |\mathbf{x}_n|\}, \quad \text{for } p = \infty,$$

is a finite-dimensional Banach space.

Definition .2. The space $L^p(\Omega)$, $1 \leq p < \infty$ is the set of measurable functions $v(\mathbf{x})$ in $\Omega \subset \mathbb{R}^n$ defined as:

$$L^p(\Omega) = \{v : \Omega \mapsto \mathbb{R} \text{ such that } \int_{\Omega} |v(\mathbf{x})|^p d\Omega < \infty, \}$$

with the following norm:

$$\|v\|_{L^p(\Omega)} = \left(\int_{\Omega} |v(\mathbf{x})|^p d\Omega \right)^{1/p}$$

More precisely L^p is the space of *equivalence classes* of measurable functions where the equivalence relation is defined in the following manner: v is equivalent to w if and only if v and w are equal almost everywhere in Ω [69].

A special case of the spaces $L^p(\Omega)$ is that of square integrable functions $L^2(\Omega)$, with $p = 2$:

$$L^2(\Omega) = \{f : \Omega \mapsto \mathbb{R} \text{ such that } \int_{\Omega} |f(\mathbf{x})|^2 d\Omega < +\infty, \}$$

The $L^2(\Omega)$ norm is associated to the scalar product[69]:

$$\|f\|_{L^2(\Omega)} = \sqrt{(f, g)_{L^2(\Omega)}},$$

where

$$(f, g)_{L^2(\Omega)} = \int_{\Omega} f(\mathbf{x})g(\mathbf{x})d\Omega, \quad (.2)$$

is the scalar product in $L^2(\Omega)$. It can be shown that the functions belonging to $L^2(\Omega)$ are special distributions. However, it is not granted that their distributional derivatives are still functions of $L^2(\Omega)$. Therefore it is appropriate to introduce the following spaces:

Definition .3. Given $\Omega \subset \mathbb{R}^n$, the Sobolev space of order k in Ω , is the space formed by all functions of $L^2(\Omega)$ having all distributional derivatives up to order k , belonging to $L^2(\Omega)$:

$$H^k(\Omega) = \{f \in L^2(\Omega) : D^\alpha f \in L^2(\Omega), \forall \alpha : |\alpha| \leq k\}.$$

For the Sobolev spaces it is possible to demonstrate the following result:

Property .1. *If Ω is an open subset of \mathbb{R}^n with sufficiently smooth edge, then:*

$$H^k(\Omega) \subset C^m(\bar{\Omega}) \quad \text{if } k > m + \frac{n}{2}.$$

A particular case of $H^k(\Omega)$ is the space $H_0^1(\Omega)$; this space is very useful and it is defined as:

$$H_0^1(\Omega) = \{f \in L^2(\Omega) : D^1 f \in L^2(\Omega) \text{ and } f(\partial\Omega) = 0\}.$$

Bibliography

- [1] American Heart Association's (AHA) annual meeting. Cardiovascular health crisis. *The Lancet*, 376, 2010.
- [2] American Heart Association's (AHA) annual meeting. Aha statistical update heart disease and stroke statistics — 2012 update: A report from the american heart association. <http://circ.ahajournals.org/>, 2012.
- [3] Heidenreich P.A., Trogon J.G., Khavjou O.A., Butler J., Dracup K., and Ezekowitz M.D. et al. Forecasting the future of cardiovascular disease in the united states: a policy statement from the american heart association. *Circulation: Journal of the American Heart Association's (AHA)*, 2011.
- [4] European Commission. Your gateway to trustworthy information on public health. *Health-EU Portal* <http://ec.europa.eu/health-eu/>, 2012.
- [5] Taylor C.A., Draney M.T., Ku J.P., Parker D., and Steele B.N. et al. Predictive medicine: computational techniques in therapeutic decision-making. *Computer Aided Surgery*, 4(5):231–247, 1999.
- [6] European Commission. Virtual physiological human network of excellence. <http://www.vph-noe.eu/>, 2012.
- [7] CMCS (École Polytechnique Fédérale de Lausanne) and MOX (Politecnico di Milano). Mathematical modelling and simulation of the cardiovascular system (mathcard) project. <http://www.mathcard.eu/>, 2009-2013.
- [8] Pozzoli M. *Efficient partitioned algorithms for the solution of fluid-structure interaction problems in haemodynamics*. PhD thesis, Politecnico di Milano, 2012.
- [9] Campeau L., Enjalbert M., Lesperance J., Vaislic C., Grondin, C. M., and Bourassa M. G. Atherosclerosis an dlate closure of aortocpronary saphenous vein grafts; sequential angiographic studies at 2 weeks, 1 year, 5-7 year and 10-12 years after surgery. *Circulation*, 68:1–7, 1983.
- [10] Fitzgibbon G.M., Kafka H.P., and Keon W.J. Coronary bypass fate: long-term angiographic study. *J.Am. Coll. Cardiol.*, 17(5):1557–1565, 1991.

- [11] Varty K., Allen K.E., Bell P.R.F., and London N.J.M. Infra-inguinal vein graft stenosis. *Br.J. Surg.*, 80:825–833, 1993.
- [12] Caro C.G., Fitz-Gerald J.M., and Schroter R.C. Atheroma and arterial wall shear stress. observations, correlation and proposal of a shear dependent mass transfer mechanism for atherogenesis. *Proc. Roy. Soc. B*, 177:109–159, 1971.
- [13] de Luca M. *Mathematical and Numerical Models for Cerebral Aneurysm Wall Mechanics*. PhD thesis, Politecnico di Milano, January 2009.
- [14] Lu J., Zhou X., and Raghavan M. Inverse method of stress analysis for cerebral aneurysms. *Journal of Biomechanics and Modeling in Mechanobiology*, 7:477–486, 2008.
- [15] Humphrey J.D. and Canham P.B. Structure, mechanical properties, and mechanics of intracranial saccular aneurysms. *Journal of Elasticity*, 61:49–81, 2000.
- [16] C. Vergara and P. Zunino. Multiscale modeling and simulation of drug release from cardiovascular stents. *SIAM Multiscale Modeling and Simulation*, 2007.
- [17] P. Zunino. Multidimensional pharmacokinetic models applied to the design of drug eluting stents. *Cardiov. Eng.*, 4(2):181–191, 2004.
- [18] Quarteroni A. and Rozza G. Optimal control and shape optimization in aorto-coronary bypass anastomoses. *Mathematical Models and Methods in Applied Sciences*, 13(12):1801–1823, 2003.
- [19] Rozza G. *Shape Design by Optimal Flow Control and Reduced Basis Techniques: Applications to Bypass Configurations in Haemodynamics*. PhD thesis, École Polytechnique Fédérale de Lausanne, 2005.
- [20] L. Formaggia, A. Quarteroni, and A. Veneziani (Eds.). *Cardiovascular Mathematics - Modeling and simulation of the circulatory system*. Springer, 2009.
- [21] L. Formaggia, A. Quarteroni, and A. Veneziani (Eds.). The circulatory system: from case studies to mathematical modeling. *Complex systems in biomedicine*, pages 243–287, 2006.
- [22] L. Formaggia, M. Fernández, A. Gauthier, J.F. Gerbeau, C. Prud’homme, and Alessandro Veneziani. The LifeV Project. Web, 2002-2004.
- [23] M.-C. Hsu and Y. Bazilevs. Blood vessel tissue prestress modeling for vascular fluid–structure interaction simulation. *Finite Elements in Analysis and Design*, 47:593–599, 2011.
- [24] M.W. Gee, C. Reeps, H.H. Eckstein, and W.A.Wall. Prestressing in finite deformation abdominal aortic aneurysm simulation. *Journal of Biomechanics*, 42:1732–1739, 2009.

- [25] M.W. Gee, C. Forster, and W.A. Wall. A computational strategy for prestressing patient-specific biomechanical problems under finite deformation. *Communications in Numerical Methods in Engineering*, 26:52–72, 2010.
- [26] de Putter S., Wolters B.J.B.M., Rutten M.C.M., Breeuwer M., Gerritsen F.A., and van de Vosse F.N. Patient-specific initial wall stress in abdominal aortic aneurysms with a backward incremental method. *Journal of Biomechanics*, 40:1081–1090, 2007.
- [27] Ciarlet P.G. *Mathematical Elasticity*, volume I. Elsevier, 1988.
- [28] G.A. Holzapfel. *Nonlinear Solid Mechanics: A continuum Approach for Engineering*. Wiley, Chichester, 2000.
- [29] LeTallec P. *Numerical Methods for Nonlinear Three Dimensional Elasticity*. Elsevier, 1994.
- [30] Ogden R.W. *Nonlinear elastic deformations*. Dover, 1997.
- [31] Holzapfel G.A., Gasser T.C., and Stadler M. A structural model for the viscoelastic behavior of arterial walls: Continuum formulation and finite element analysis. *European Journal of Mechanics - A/Solids*, 21:441–463, 2002.
- [32] Holzapfel G.A., Gasser T.C., and Ogden R.W. A new constitutive framework for arterial wall mechanics and a comparative study of material models. *Journal of Elasticity*, 61:1–48, 2000.
- [33] Kalita P. and Schaefer R. Mechanical models of artery walls. *Archives of Computational Methods in Engineering*, 15:1–36, 2008.
- [34] Holzapfel G.A. and Ogden R.W. Constitutive modelling of arteries. *Proc. R. Soc. A*, 466:1551–1597, 2010.
- [35] J.A.G. Rhodin. Architecture of the vessel wall. *Handbook of Physiology*, 2:1–31, 1980.
- [36] Holzapfel G.A. and Ogden R.W. In planar biaxial tests for anisotropic nonlinearly elastic solids. a continuum mechanical framework. *Mathematics and Mechanics of Solids*, 14:474–489, 2009.
- [37] Wulandana R. and Robertson A.M. An inelastic multi-mechanism constitutive equation for cerebral arterial tissue. *Biomechanics and Modeling in Mechanobiology*, 4:235–248, 2005.
- [38] Li D. and Robertson A.M. A structural multi-mechanism constitutive equation for cerebral arterial tissue. *International Journal of Solids and Structures*, 46:2920–2928, 2009.

- [39] Li D. *Structural multi-mechanism model with anisotropic damage for cerebral arterial tissues and its finite element modelling*. PhD thesis, University of Pittsburgh, November 2009.
- [40] Sommer G., Regitnig P., Költringer L., and Holzapfel G.A. Biaxial mechanical properties of intact and layer-dissected human carotid arteries at physiological and supra-physiological loadings. *Am. J. Physiol. Heart Circ. Physiol.*, 298:H898–H912, 2010.
- [41] Schulze-Bauer C.A.J. and Holzapfel G.A. Determination of constitutive equations for human arteries from clinical data. *Journal of Biomechanics*, 36:165–169, 2003.
- [42] J.D. Humphrey. *Cardiovascular Solid Mechanics, Cells, Tissues, and Organs*. Springer, New York, 2002.
- [43] Y.C. Fung. *Biomechanics: Motion, Flow, Stress, and Growth*. Springer, New York, 1990.
- [44] A. Valentin, L. Cardamone, S. Baek, and J.D. Humphrey. Complementary vasoactivity and matrix remodelling in arterial adaptations to altered flow and pressure. *J. R. Soc. Interface*, 6:293–306, 2009.
- [45] J. Stalhand, A. Klarbring, and M. Karlsson. Towards in vivo aorta material identification and stress estimation. *Biomechanics and Modeling in Mechanobiology*, 2:169–186, 2004.
- [46] I. Masson, P. Boutouyrie, S. Laurent, J.D. Humphrey, and M. Zidi. Characterization of arterial wall mechanical behavior and stresses from human clinical data. *Journal of Biomechanics*, 41:2618–2627, 2008.
- [47] T.J.R. Hughes, W.K. Liu, and T.K. Zimmermann. Lagrangian–eulerian finite element formulation for incompressible viscous flows. *Computer Methods in Applied Mechanics and Engineering*, 29(3):329–349, 1981.
- [48] C.A. Figueroa, I.E. Vignon-Clementel, K.C. Jansen, T.J.R. Hughes, and C.A. Taylor. A coupled momentum method for modeling blood flow in three-dimensional deformable arteries. *Computer Methods in Applied Mechanics and Engineering*, 195:5685–5706, 2006.
- [49] T.E. Tezduyar, S. Sathe, M. Schwaab, and B.S. Conklin. Arterial fluid mechanics modeling with the stabilized space-time fluid–structure interaction technique. *International Journal for Numerical Methods in Fluids*, 57:601–629, 2008.
- [50] T.E. Tezduyar. Stabilized finite element formulations for incompressible flow computations. *Advances in Applied Mechanics*, 28:1–44, 1992.

- [51] T.E. Tezduyar, Behr M., and Liou J. A new strategy for finite element computations involving moving boundaries and interfaces—the deforming-spatial-domain/space-time procedure: I. the concept and the preliminary numerical tests. *Computer Methods in Applied Mechanics and Engineering*, 94:339–351, 1992.
- [52] T.E. Tezduyar, Behr M., Mittal S., and Liou J. A new strategy for finite element computations involving moving boundaries and interfaces—the deforming-spatial-domain/space-time procedure: II. computation of free-surface flows, two-liquid flows, and flows with drifting cylinders. *Computer Methods in Applied Mechanics and Engineering*, 94:353–371, 1992.
- [53] T.E. Tezduyar. Computation of moving boundaries and interfaces and stabilization parameters. *International Journal for Numerical Methods in Fluids*, 43:555–575, 2003.
- [54] Hughes T.J.R. and Brooks A.N. A multi-dimensional upwind scheme with no crosswind diffusion. in finite element methods for convection dominated flows. *ASME: New York*, 34:19–35, 1979.
- [55] Brooks A.N. and Hughes T.J.R. Streamline upwind/petrov-galerkin formulations for convection dominated flows with particular emphasis on the incompressible navier-stokes equations. *Computer Methods in Applied Mechanics and Engineering*, 32:199–259, 1982.
- [56] Tezduyar T.E., Mittal S., Ray S.E., and Shih R. Incompressible flow computations with stabilized bilinear and linear equal-order-interpolation velocity-pressure elements. *Computer Methods in Applied Mechanics and Engineering*, 95:221–242, 1992.
- [57] C.S. Peskin. The immersed boundary method. *Acta Numerica*, 11:1–39, 2002.
- [58] P.F. Davies. Flow-mediated endothelial mechanotransduction. *Physiol. Rev.*, 75:519–560, 1995.
- [59] B.I. Levy and A. Tedgui. *Biology of the Arterial Wall*. Kluwer Academic Publishers, Dordrecht, 1999.
- [60] A. Rachev. A model of arterial adaptation to alterations in blood flow. *Journal of Elasticity*, 61:83–111, 2000.
- [61] L.A. Taber. A model for aortic growth based on fluid shear and fiber stresses. *Journal of Biomechanical Engineering*, 120:348–354, 1998.
- [62] J.D. Humphrey and K.R. Rajagopal. A constrained mixture model for growth and remodeling of soft tissues. *Math. Model Method Appl. Sci.*, 12:407–430, 2002.
- [63] P.N. Watton, N.A. Hill, and M. Heil. A mathematical model for the growth of the abdominal aortic aneurysm. *Biomech. Model Mechanobiol.*, 3:98–113, 2004.

- [64] J.D. Humphrey and C.A. Taylor. Intracranial and abdominal aortic aneurysms: similarities, differences, and need for a new class of computational models. *Annu. Rev. Biomed. Engrg.*, 10:221–246, 2008.
- [65] S. Baek, R.L. Gleason, K.R. Rajagopal, and J.D. Humphrey. Theory of small on large: potential utility in computations of fluid–solid interactions in arteries. *Comput. Methods Appl. Mech. Engrg.*, 196:3070–3078, 2007.
- [66] C.A. Figueroa, S. Baek, C.A. Taylor, and J.D. Humphrey. A computational framework for fluid–solid-growth modeling in cardiovascular simulations. *Computer Methods in Applied Mechanics and Engineering*, 198:3583–3602, 2009.
- [67] P. Moireau, N. Xiao, M. Astorino, C.A. Figueroa, D. Chapelle, C.A. Taylor, and J.-F. Gerbeau. External tissue support and fluid–structure simulation in blood flows. *Biomechanics and Modeling in Mechanobiology*, 11:1–18, 2011.
- [68] Bonet J. and Wood R.D. *Nonlinear Continuum Mechanics for Finite Element Analysis*. Cambridge University Press, 1997.
- [69] Quarteroni A. *Modellistica numerica per problemi differenziali*. Springer, 2008.
- [70] Hughes T.J.R. *The finite element method. Linear static and dynamic finite element analysis*. Prentice-Hall, 1987.
- [71] Quarteroni A., Sacco R., and Saleri F. *Matematica numerica*. Springer, 2008.
- [72] de Luca M., Ambrosi D., Robertson A.M., Veneziani A., and Quarteroni A. Finite element analysis for a multi-mechanism damage model of cerebral arterial tissue. *MOX-Report*, 25, 2011.
- [73] L. Antiga, M. Piccinelli, L. Botti, B. Ene-Iordache, A. Remuzzi, and DA. Steinman. An image-based modeling framework for patient-specific computational hemodynamics. *Medical and Biological Engineering and Computing*, 46:1097–1112, 2008.
- [74] L. Antiga and DA. Steinman. Robust and objective decomposition and mapping of bifurcating vessels. *IEEE Transactions on Medical Imaging*, 23:704–713, 2004.
- [75] L. Speelman, E.M.H. Bosboom, G.W.H. Schurink, J. Buth, M. Breeuwer, M.J. Jacobs, and F.N. van de Vosse. Initial stress and nonlinear material behaviour in patient-specific aaa wall stress analysis. *Journal of Biomechanics*, 42:1713–1719, 2009.
- [76] J.C. Simo and T.J.R. Hughes. *Computational Inelasticity*. Springer-Verlag, New York, 1998.
- [77] Lu J., Zhou X., and Raghavan M. Inverse elastostatic stress analysis in pre-deformed biological structures: demonstration using abdominal aortic aneurysms. *Journal of Biomechanics*, 40:693–696, 2007.

- [78] V. Fachinotti, A. Cardona, and P. Jetteur. Finite element modelling of inverse design problems in large deformation anisotropic hyperelasticity. *International Journal for Numerical Methods in Engineering*, 74:894–910, 2008.
- [79] P. Chadwick. Application of an energy-momentum tensor in elastostatics. *Journal of Elasticity*, 5:249–258, 1975.
- [80] R. Shield. Inverse deformation results in finite elasticity. *Zeitschrift fur Angewandte Mathematik und Physik*, 18:381–389, 1967.
- [81] S. Govindjee and P. Mihalic. Computational methods for inverse finite elastostatics. *Computer Methods in Applied Mechanics and Engineering*, 136:47–57, 1996.
- [82] S. Govindjee and P. Mihalic. Computational methods for inverse deformations in quasi-incompressible finite elasticity. *International Journal for Numerical Methods in Engineering*, 43:821–838, 1998.
- [83] Lu J., Zhou X., and Raghavan M. Computational method of inverse elastostatics for anisotropic hyperelastic solids. *International Journal for Numerical Methods in Engineering*, 69:1239–1261, 2007.
- [84] L. Speelman, A.C. Akyildiz, B. den Adel, J.J. Wentzel, A.F.W. van der Steen, R. Virmani, L. van der Weerd, J.W. Jukema, R.E. Poelmann, E.H. van Brummelen, and F.J.H. Gijssen. Initial stress in biomechanical models of atherosclerotic plaques. *Journal of Biomechanics*, 44:2376–2382, 2011.
- [85] L. Antiga and DA. Steinman. The vascular modeling toolkit. <http://www.vmtk.org>, 2008.
- [86] Y. Liu, C. Charles, M. Gracia, H. Gregersen, and G. S. Kassab. Surrounding tissues affect the passive mechanics of the vessel wall: theory and experiment. *Am. J. Physiol. Heart Circ. Physiol.*, 293:H3290–H3300, 2007.
- [87] R. Ross. Atherosclerosis – an inflammatory disease. *New Engl. J. Med.*, 340(2):115–126, 1999.
- [88] F.J. Gijssen, E. Allanic, F.N. van de Vosse, and J.D. Janssen. The influence of the non-newtonian properties of blood on the flow in large arteries: unsteady flow in a 90 degrees curved tube. *J. Biomech.*, 32(7):705–713, 1999.
- [89] Cebal J.R., Mut F., Weir J., and Putman C.M. Association of hemodynamic characteristics and cerebral aneurysm rupture. *American Journal of Neuroradiology*, 32(2):264–270, 2011.
- [90] Zakaria H., Robertson A.M., and Kerber C.W. A parametric model for studies of flow in arterial bifurcations. *Annals of Biomedical Engineering*, 36(9):1515–1530, 2008.

- [91] Valencia A. and Solis F. Blood flow dynamics and arterial wall interaction in a saccular aneurysm model of the basilar artery. *Computers & Structures*, 84:1326–1337, 2006.
- [92] Bazilevs Y., Hsu M.C., Zhang Y., Wang W., Kvamsdal T., Hentschel S., and Isaksen J.G. Computational vascular fluid-structure interaction: methodology and application to cerebral aneurysms. *Biomechanics and Modeling in Mechanobiology*, 9:481–498, 2010.
- [93] Ottesen J.T., Olufsen M.S., and Larsen J.K. *Applied Mathematical Models in Human Physiology*. Society for Industrial and Applied Mathematics, 2010.
- [94] A. Quarteroni and A. Valli. *Numerical approximation of partial differential equations*. Springer, 1994.
- [95] O. Ladyzhenskaya. *The mathematical theory of viscous incompressible flow*. Gordon and Breach, New York, 1969.
- [96] J. Donea. An arbitrary lagrangian-eulerian finite element method for transient dynamic fluid-structure interaction. *Computer Methods in Applied Mechanics and Engineering*, 33:689–723, 1982.
- [97] Nobile F. *Numerical approximation of fluid-structure interaction problems with application to haemodynamics*. PhD thesis, École Polytechnique Fédérale de Lausanne, 2001.
- [98] F. Brezzi and M. Fortin. *Mixed and hybrid finite element methods*. Springer-Verlag, 1991.
- [99] K. Perktold, E. Thurner, and T. Kenner. Flow and stress characteristics in rigid walled and compliant carotid artery bifurcation models. *Medical and Biological Engineering and Computing*, 32(1):19–26, 1994.
- [100] Y. Bazilevs, V. Calo, Y. Zhang, and T. Hughes. Isogeometric fluid-structure interaction analysis with applications to arterial blood flow. *Computational Mechanics*, 38:310–322, 2006.
- [101] T. Tezduyar, S. Sathe, T. Cragin, B. Nanna, B. Conklin, J. Pausewang, and M. Schwaab. Modelling of fluid-structure interactions with the space-time finite elements: arterial fluid mechanics. *International Journal for Numerical Methods in Fluids*, 54:901–922, 2007.
- [102] M. Fernández, J. Gerbeau, and C. Grandmont. A projection semi-implicit scheme for the coupling of an elastic structure with an incompressible fluid. *International Journal for Numerical Methods in Engineering*, 69(4):794–821, 2007.
- [103] S. Badia, F. Nobile, and C. Vergara. Fluid-structure partitioned procedures based on robin transmission conditions. *Journal of Computational Physics*, 227:7027–7051, 2008.

- [104] L. Azzimonti, P. Buratti, M. Domanin, , and P. Secchi. Classification of doppler signals for the detection of atherosclerotic plaques in the carotid bifurcation. In preparation.
- [105] P. Buratti. *Analysis of Doppler blood flow velocity in carotid arteries for the detection of atherosclerotic plaques*. PhD thesis, Politecnico di Milano, 2011.
- [106] S. A. Berger. Flow in large blood vessels. *Contemporary Mathematics*, 141:479–518, 1993.
- [107] L. Formaggia, J.-F. Gerbeau, F. Nobile, and A. Quarteroni. On the coupling of 3d and 1d navier-stokes equations for flow problems in compliant vessels. *Computer Methods in Applied Mechanics and Engineering*, 191(6-7):561–582, 2001.
- [108] L. Formaggia, F. Nobile, A. Quarteroni, and A. Veneziani. Multiscale modelling of the circulatory system: a preliminary analysis. *Comp. Vis. Sc.*, 2:75–83, 1999.
- [109] T. Pedley. *The fluid mechanics of large blood vessels*. Cambridge University Press, Cambridge, 1980.
- [110] F. Nobile and C. Vergara. An effective fluid-structure interaction formulation for vascular dynamics by generalized robin conditions. *SIAM J. Sc. Comp.*, 30(2):731–763, 2008.
- [111] C. Vergara. Nitsche’s method for defective boundary value problems in incompressible fluid-dynamics. *J. Sci. Comp.*, 46(1):100–123, 2011.
- [112] P. Crosetto, S. Deparis, G. Fourestey, and A. Quarteroni. Parallel algorithms for fluid-structure interaction problems in haemodynamics. *SIAM Journal of Scientific Computing*, 33:1598–1622, 2011.
- [113] F. Nobile, M. Pozzoli, and C. Vergara. Time accurate partitioned algorithms for the solution of fluid-structure interaction problems in haemodynamics. *MOX-Report n.30-2011*, 2011. Submitted.
- [114] S. Piperno and C. Farhat. Design of efficient partitioned procedures for transient solution of aerolastic problems. *Rev. Eur. Elements Finis*, 9(6-7):655–680, 2000.
- [115] P. Causin, J. Gerbeau, and F. Nobile. Added-mass effect in the design of partitioned algorithms for fluid-structure problems. *Computer Methods in Applied Mechanics and Engineering*, 194(42-44):4506–4527, 2005.
- [116] S. Deparis, M. Discacciati, G. Fourestey, and A. Quarteroni. Fluid-structure algorithms based on steklov-poincaré operators. *Computer Methods in Applied Mechanics and Engineering*, 195(41-43):5797–5812, 2006.
- [117] S. Badia, F. Nobile, and C. Vergara. Robin-robin preconditioned krylov methods for fluid-structure interaction problems. *Computer Methods in Applied Mechanics and Engineering*, 198(33-36):2768–2784, 2009.

- [118] M. Astorino, F. Chouly, and M. Fernández. Robin based semi-implicit coupling in fluid-structure interaction: stability analysis and numerics. *SIAM J. Sc. Comp.*, 31(6):4041–4065, 2009.
- [119] M. Heil. An efficient solver for the fully coupled solution of large-displacement fluid-structure interaction problems. *Computer Methods in Applied Mechanics and Engineering*, 193:1–23, 2004.
- [120] M. Fernández and M. Moubachir. A newton method using exact jacobians for solving fluid-structure coupling. *Computers & Structures*, 83(2-3):127–142, 2005.
- [121] S. Badia, A. Quaini, and A. Quarteroni. Splitting methods based on algebraic factorization for fluid-structure interaction. *SIAM J. Sc. Comp.*, 30(4):1778–1805, 2008.
- [122] J. Gerbeau and M. Vidrascu. A quasi-newton algorithm based on a reduced model for fluid-structure interaction problems in blood flows. *Mathematical Modelling and Numerical Analysis*, 37(4):631–648, 2003.
- [123] R. Kirby, Z. Yosibash, and G. Karniadakis. Towards stable coupling methods for high-order discretization of fluid-structure interaction: algorithms and observations. *Journal of Computational Physics*, 223:489–518, 2007.
- [124] U. Kuttler and W. Wall. Fixed-point fluid-structure interaction solvers with dynamic relaxation. *Comput. Mech.*, 43:61–72, 2008.
- [125] C. Kassiotis, A. Ibrahimbegovic, R. Niekamp, and H. Matthies. Nonlinear fluid-structure interaction problem. part i: implicit partitioned algorithm, nonlinear stability proof and validation examples. *Comput. Mech.*, 47:305–323, 2011.
- [126] M. Heil, A. Hazel, and J. Boyle. Solvers for large-displacement fluid-structure interaction problems: segregated versus monolithic approaches. *Comp. Mech.*, 43:91–101, 2008.
- [127] H. Matthies, R. Niekamp, and J. Steindorf. Algorithms for strong coupling procedures. *Computers & Structures*, 195:2028–2049, 2006.
- [128] U. Kuttler, M. Gee, C. Forster, A. Comerford, and W. Wall. Coupling strategies for biomedical fluid-structure interaction problems. *Int. J. Num. Meth. Biomed. Eng.*, 26:305–321, 2010.
- [129] W. Dettmer and D. Perić. On the coupling between fluid flow and mesh motion in the modelling of fluid-structure interaction. *Comp. Mech.*, 43:81–90, 2008.
- [130] T. Tezduyar, S. Sathe, and K. Stein. Solution techniques for the fully discretized equations in computation of fluid-structure interactions with the spacetime formulations. *Computer Methods in Applied Mechanics and Engineering*, 195(41-43):5743–5753, 2006.

- [131] A. Barker and X.-C. Cai. Scalable parallel methods for monolithic coupling in fluid-structure interaction with application to blood flow modeling. *J. Comput. Phys.*, 229:6426–6459, 2010.
- [132] M. Gee, U. Kuttler, and W. Wall. Truly monolithic algebraic multigrid for fluid-structure interaction. *International Journal for Numerical Methods in Engineering*, 85(8):987–1016, 2011.
- [133] C. Forster, W. Wall, and E. Ramm. Artificial added mass instabilities in sequential staggered coupling of nonlinear structures and incompressible viscous flow. *Computer Methods in Applied Mechanics and Engineering*, 196(7):1278–1293, 2007.
- [134] P. L. Tallec and J. Mouro. Fluid structure interaction with large structural displacements. *Computer Methods in Applied Mechanics and Engineering*, 190:3039–3067, 2001.
- [135] L. Gerardo Giorda, F. Nobile, , and C. Vergara. Analysis and optimization of robin-robin partitioned procedures in fluid-structure interaction problems. *SIAM J. Numer. Anal.*, 48(6):2091–2116, 2010.
- [136] A.F. AbuRahma, J.T.J. Wulu, and B. Crotty. Carotid plaque ultrasonic heterogeneity and severity of stenosis. *Stroke*, 33:1772–1775, 2002.
- [137] B.K. Lal, R.W.I. Hobson, and P.J. Pappas. Pixel distribution analysis of b-mode ultrasound scan images predicts histologic features of atherosclerotic carotid plaques. *J. Vasc. Surg.*, 35:1210–1217, 2002.
- [138] D.N.Ku and D.P. Giddens. Pulsatile flow in a model carotid bifurcation. *Arteriosclerosis*, 3(1):31–39, 1983.
- [139] D.A. Steinman. Image-based computational fluid dynamics modeling in realistic arterial geometries. *Ann. Biomed. Eng.*, 30:483–497, 2002.
- [140] D.N. Ku, D.P. Giddens, C.K. Zarins, and S. Glagov. Pulsatile flow and atherosclerosis in the human carotid bifurcation: positive correlation between plaque location and low oscillating shear stress. *Arteriosclerosis*, 5:293–302, 1985.
- [141] S. Glagov, C. Zarins, D.P. Giddens, and D.N. Ku. Hemodynamics and atherosclerosis: insights and perspectives gained from studies of human arteries. *Arch. Pathol. Lab. Med.*, 112:1018–1031, 1988.
- [142] D.L. Fry. Acute vascular endothelial changes associated with increased blood velocity gradients. *Circulation Res.*, 22:165–197, 1968.
- [143] D. Giddens, C. Zarins, and S. Glagov. The role of fluid mechanics in the localization and detection of atherosclerosis. *J. Biomech. Eng.*, 115:588–594, 1993.

- [144] C.K. Zarins, D.P. Giddens, B.K. Bharadvaj, S.V. Sottiurai, R.F. Mabon, and S. Glagov. Carotid bifurcation atherosclerosis: quantitative correlation of plaque localization with flow velocity profiles and wall shear stress. *Circulation Res.*, 53:502–514, 1983.
- [145] Gibson C.M., Diaz L., and Kandarpa K. et al. Relation of vessel wall shear stress to atherosclerosis progression in human coronary arteries. *Arterioscler. Thromb. Vasc. Biol.*, 18:708–718, 1998.
- [146] Gnasso A., Irace C., and Carallo C. et al. Association between intima-media thickness and wall shear stress in common carotid arteries in healthy male subjects. *Circulation*, 94:3257–3262, 1996.
- [147] Malek A.M., Alper S.L., and Izumo S. Hemodynamic shear stress and its role in atherosclerosis. *The Journal of the American Medical Association*, 282:2035–2042, 1999.
- [148] Rossitti S. and Svendsen P. Shear stress in cerebral arteries supplying arteriovenous malformations. *Acta Neurochir.*, 137(3-4):138–145, 1995.
- [149] P.W. Alford, J.D. Humphrey, and L.A. Taber. Growth and remodeling in a thick-walled artery model: effects of spatial variations in wall constituents. *Biomechanics and Modeling in Mechanobiology*, 7:245–262, 2008.
- [150] Agoshkov V., Quarteroni A., and Rozza G. Shape design approach using perturbation theory for bypass anastomoses. *SIAM Journal on Numerical Analysis*, 44(1):367–384, 2006.
- [151] E. Swim and P. Seshaiyer. A nonconforming finite element method for fluid-structure interaction problems. *Computer Methods in Applied Mechanics and Engineering*, 195:2088–2099, 2006.
- [152] C. M. Murea and S. Sy. A fast method for solving fluid-structure interaction problems numerically. *International Journal for Numerical Methods in Fluids*, 60:1149–1172, 2009.
- [153] E. Hairer, S. Norsett, and G. Wanner. *Solving ordinary differential equations: Nonstiff problems*. Springer series in computational mathematics, 1993.
- [154] A. Veneziani and C. Vergara. Flow rate defective boundary conditions in haemodynamics simulations. *International Journal for Numerical Methods in Fluids*, 47:803–816, 2005.
- [155] L. Formaggia, A. Veneziani, and C. Vergara. Flow rate boundary problems for an incompressible fluid in deformable domains: formulations and solution methods. *Computer Methods in Applied Mechanics and Engineering*, 199(9-12):677–688, 2009.